Toroidal Droplets: Instabilities, Stabilizing and Nematic Order

A Thesis
Presented to
The Academic Faculty

by

Ekapop Pairam

In Partial Fulfillment
of the Requirements for the Degree
Doctor of Philosophy

School of Physics
Georgia Institute of Technology
May 2014

Toroidal Droplets: Instabilities, Stabilizing and Nematic Order

Approved by:

Professor Alberto Fernández-Nieves, Adviser
School of Physics
Georgia Institute of Technology

Professor Roman Grigoriev
School of Physics
Georgia Institute of Technology

Professor Paul Goldbart
School of Physics
Georgia Institute of Technology

Professor Michael Schatz
School of Physics
Georgia Institute of Technology

Professor Mohan Srinivasarao
School of Material Science and Engineering
Georgia Institute of Technology

Date Approved: April 7, 2014

ACKNOWLEDGEMENTS

I would like to first thank my Ph.D. adviser Alberto Fernández-Nieves for funding, support, inspiration and the most excellent guidance any graduate student could ever hope for. I am also very grateful for the fact that he accepted me into his lab when I had nowhere to go. Not only this, but time and time again he never gave up in helping and believing even after the countless mistakes that I made.

I would like to express my gratitude especially to Jayalakshmi Vallamkondu, Eric Berger and Hung Le who made major contributions to this research and whose work made their way into my thesis and Kevin Mohan and Josefa Guerrero for spending a huge amount of their time to develop an image analysis program to measure surface tension.

I am also grateful for Vinzenz Koning, Vincenzo Vitelli, Benjamin van Zuiden, Martin Bates and Perry Ellis for providing the theory and simulations which provided major insight in understanding our result in the nematic liquid crystal droplets section.

I would also like to thank Alexandros Fragkopoulos and Zhenwei Yao for useful discussion on hydrodynamic instabilities of toroidal droplet, Phillip Sergrè for useful discussion on the PIV experimental setup, John Hyatt for proof reading my thesis, all my friends and people of the soft condensed matter lab for helping me learn how function in society.

Lastly but not least, I would like to thank my family for all their support, especially my father who is my hero and a role model, my mother who worked without rest to make my dream of continuing my higher education in United States possible and also my aunt Rajaporn Ackarawongwathana who provided unconditional support from the beginning to the end.

TABLE OF CONTENTS

LIST OF TABLES

LIST OF FIGURES

SUMMARY

The goal of this thesis is to study the ground or metastable state structure of nematic liquid crystal systems confined inside handled shapes such as a torus or double torus. We begin our work by introducing a new method to generate a toroidal droplet from a Newtonian liquid inside another, immiscible, Newtonian liquid. In this situation, a toroidal droplet is unstable and follows one of two routes in transforming into a spherical droplet: (i) its tube breaks in a way reminiscent to the breakup of a cylindrical jet, or (ii) its tube grows until it finally coalesces onto itself. However, to be able to probe the nematic structure, we need to address the issue of instabilities. This is done by replacing the outer liquid with a yield stress material, which ultimately leads to the stabilization of the toroidal droplet. Through the experimental investigation, we are able to establish the stabilization conditions. Finally, we generate and stabilize toroidal droplets with a nematic liquid crystal as the inner liquid and a yield stress material as the outer medium. Here we observe that in the ground state, the nematic liquid crystal exhibits an intriguing twisted structure irrespective of the aspect ratio of the torus. While there are no defects observed in a toroidal droplet case, two defects with -1 topological charge each emerge each time we increase the number of handles.

CHAPTER I

INTRODUCTION

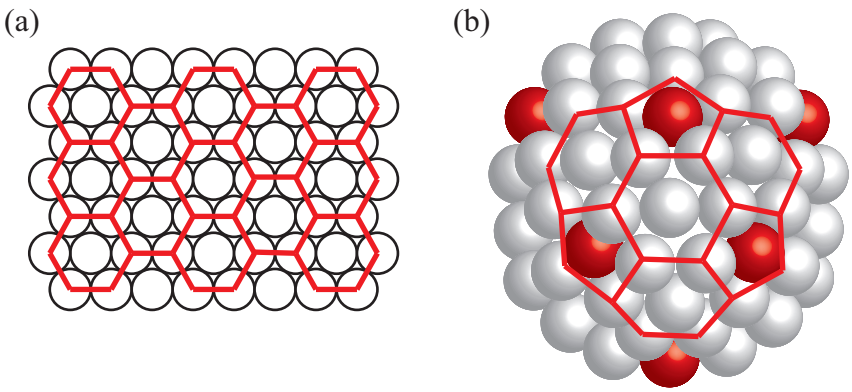

Figure 1.1: Spheres packed into crystalline order on a 2-dimensional (a) flat and (b) spherical surfaces.

Many natural and synthetic systems involve ordered arrangement of units on 2-dimensional surfaces. The structure of these arrangements are profoundly affected by the geometric property of the surface. For instance, on a flat surface, spherical particles in crystalline order pack most efficiently in a simple triangular lattice. Here, the preferred local order of six-fold coordinated triangular lattices can be fulfilled everywhere in space and every sphere has six nearest neighbors, as shown in figure 1.1(a). However, to cover the whole surface of a sphere, such order cannot be maintained globally. Instead, at least 12 five-fold coordinated (sphere with five nearest neighbors) are needed (see figure 1.1(b)). Some familiar examples of this are seen in soccer balls and C_{60} fullerenes [1, 2]. The net number of pentagonal defects on a spherical surface follows from the Euler theorem [3]:

$$\sum_{i}^{V}(6 - c_i) = 6\chi\,, \tag{1.1}$$

where V is the number of vertices (located at the center of each sphere in figure 1.1), c_i is coordination number of the ith sphere, $\chi = \frac{1}{2\pi}\oiint KdS$ is the Euler characteristic or topological invariant (with K as the Gaussian curvature) and is equal to 2 for a sphere. However, the physical system

does not always select the configuration with a minimal number of defects in compliance with Euler theorem. In fact, the strain associated with an isolated pentagon defect grows with the number of particles on the sphere. To relieve the strain, the crystalline order introduces additional pairs of tightly bounded pentagon and heptagon defects [4, 5, 6, 7]. This can also be intuitively understood by creating disclination out of paper by folding a hexagon shape (made out of 6 equilateral triangles) into a pentagon or heptagon by removing or adding a triangle, respectively, as shown in figure 1.2 [8]; note the positive curvature of the pentagon in figure 1.2(c) and the negative curvature of the heptagon in figure 1.2(h). Here each pentagon contributes positive Gaussian curvature while each heptagon contribute negative Gaussian curvature.

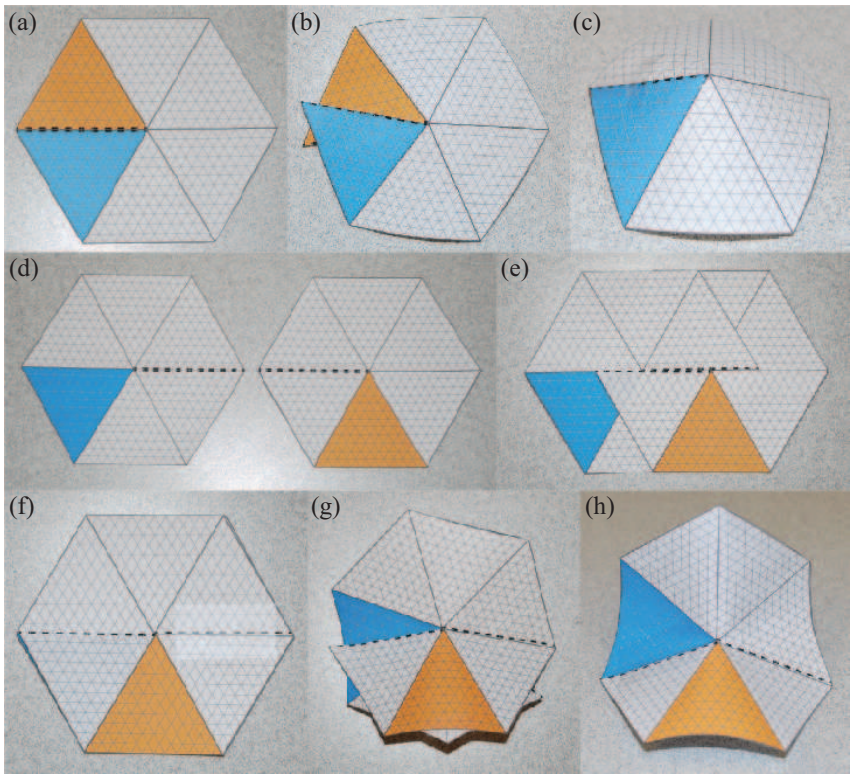

Figure 1.2: Sequences of a paper hexagon folded into (a)-(c) pentagon and (d)-(h) heptagon.

Analogously to packing spherical particles to represent crystalline structure, we can pack rods to represent the nematic order of a liquid crystal. Unlike particles in a crystal lattice, nematic liquid crystal molecules do not have positional order but they tend to align along a preferred direction characterized by a director, **n**. It is easy to see that rods on a flat space can be arranged such that **n** are well-defined everywhere, as shown in figure 1.3(a). However, it is impossible for **n** to be

well-defined everywhere when rods are packed onto a spherical surface. Some familiar examples are the bipolar and concentric configurations, as shown in figure 1.3(b) and (c), respectively. The singularities of **n** are topological defects whose topological charge s measures how much **n** rotates about the defect core in multiples of 2π radians. Thus the director patterns in figure 1.3(b) and (c) have two $s = +1$ defects while the one in figure 1.3(d) has four $s = +1/2$ defects, consistent with the Poincaré-Hopf theorem [9]:

$$\sum_i s_i = \chi \,. \tag{1.2}$$

The structure in figure 1.3(d) is predicted to be the ground state for nematic order on the surface of a sphere [10]. Experimental study of thin spherical nematic liquid crystal shells also shows that, beside this configuration, there exist a bipolar and trigonal geometries of sp^3 carbon bonds structure with three defects (one $s = +1$ and two $s = +1/2$) metastable states [11]. This emphasizes the fact that the minimum energy state in a physical system is not always the simplest solution possible in compliance with the topological constraints.

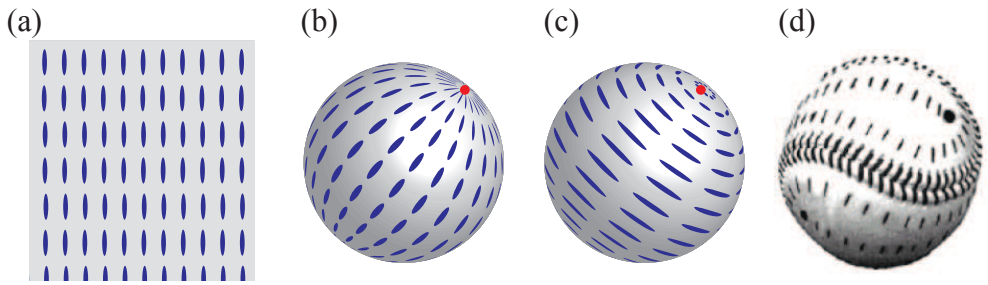

Figure 1.3: Examples of rods arranged in parallel on (a) flat and on (b-d) spherical surface.

There has been a lot of experimental, theoretical and simulation research on the behavior of ordered media confined in spherical volumes [12, 13, 14, 15, 16, 17, 18, 19, 20] and their intriguing technological potential for divalent nano-particle assembly has been already demonstrated [21]. In contrast, there are virtually no controlled experiments with ordered media confined in volumes with handles. A notable exception is the optically induced formation of cholesteric toroidal droplets inside a nematic host [22]. This largely reflects the difficulties in generating stable handled objects with imposed order. While the spherical droplet is relatively easy to create in liquids due to surface tension will always minimize the surface area of the droplet, the generation of stable droplets with

handles posed a challenge because volume for volume they posses a larger surface area than the sphere.

Our goal is to study the metastable and ground state structure of ordered material confined within handled volume, which has topological properties different from those of a sphere. This is made possible by the development of a method to generate and stabilize droplets with a toroidal shape. As a result, our studies are arranged in the following order:

In chapter 2, we introduce a method used to generate toroidal droplets in a viscous medium. These droplets are unstable and evolve into spherical droplets by either breaking up or growing fatter and then coalescing onto itself. Both of these mechanisms are explored and discussed in detail. In addition, we employ the method of particle imaging velocimetry (PIV) to study the flow field inside collapsing toroidal droplets.

In chapter 3, we address the instabilities of the viscous toroidal droplets by replacing the outer simple liquid medium with a yield stress material. From observation and analysis of the behavior of toroidal droplets generated in this manner, we are able to identify the conditions for stabilizing the toroidal shape.

In chapter 4, we probe the nematic order of liquids crystal confined inside a toroidal drop using optical polarizing microscopy. In addition, we identify the defect locations which emerge due to the addition of extra handles in compliance with the Poincaré-Hopf theorem.

CHAPTER II

INSTABILITIES OF VISCOUS TOROIDAL DROPLETS INSIDE ANOTHER IMMISCIBLE CONTINUOUS VISCOUS LIQUID PHASE

2.1 Introduction

Bubbles and droplets are common in everyday life. They make rain and clouds, and are essential constituents of many of the healthcare we often use and food products we eat. Bubbles and droplets are indeed ubiquitous in nature and they have a spherical shape. Surface tension gives them their spherical shape by minimizing the surface area for a given volume [24]. As a result, any means of dispersing a gas or a liquid in a fluid inevitably results in a spherical bubble or a spherical droplet. In contrast, generating fluid objects with non-minimal surface shapes, such as a torus, is far more complicated and still remains a challenge. Despite the difficulty, this can be achieved by using external forces. For example, if rotated at sufficiently high speed, a freely suspended droplet can take on a variety of non-spherical shapes, including the torus; Plateau showed this experimentally [25], although it was not until about a century later that his observations were understood [26] and refined [27]. A bubble can also adopt the shape of a torus if vibrated [28] and dolphins make fascinating vortex rings, which have a toroidal shape [29, 30]. Further examples are provided by the free fall of a droplet in an immiscible fluid [31, 32] or by the impact of a droplet with a superhydrophobic surface [33]. Inevitably, the toroidal droplet or bubble generated by any of these means is unstable and always transforms into a spherical drop once the external force vanishes. However, the details of this collapse are not well known, reflecting in large measure the experimental difficulties in generating toroidal droplets under well-controlled conditions.

In this chapter, we report on a novel procedure to generate toroidal droplets and on how they transform into spherical droplets. Our technique enables precise control of the aspect ratio of the torus, which is in turn the relevant parameter determining its stability. For thin tori, the classical

hydrodynamic instability causing the breakup of a long fluid cylinder, or jet, is also responsible for the breakup of the torus. In this case, however, only modes with a wavelength commensurate with the torus length can grow. By monitoring the breakup as a function of time for different viscosity ratio, we are able to clarify that the growth of capillary disturbance on a torus is the same as that for the cylindrical jet. Interestingly, for sufficiently fat tori, no unstable modes can develop, and the torus shrinks towards its center to finally coalesce onto itself. This shrinkage is always present irrespective of the aspect ratio of the torus, but becomes the dominant mechanism for sufficiently fat tori. This mechanism has sparked an interest in both the theoretical and simulation study. In the theoretical study, Yao and Bowick calculated the analytical results for hydrodynamic properties of a shrinking torus [34]. In the simulation study, breakup model which taking into account the effect of shrinking and curvature of the torus were simulated by Mehrabian and Feng [37]. Inspired by a theoretical work of [34], experiment utilizing Particle Imaging Velocimetry (PIV) were carried out and the results are presented at the end of the chapter.

2.2 Generating Toroidal Droplets

Our method to generate a toroidal droplet is by injecting a liquid through a metallic needle into a rotating bath with rotational speed ω, as shown in figure 2.1(a). As a result of the viscous drag exerted by the outer fluid over the extruded liquid coupling with the rotation a circular jet is generated at the exit of the needle, as shown in figure 2.3(a) and (c) ,provided that the capillary number Ca_o is greater than 1 [38]. However, if the rotational velocity, v_o, is not large enough, the jet breaks before the torus can be formed, as shown in figure 2.3(b). In contrast, if v_o is sufficiently large then the jet will close in on itself and we get the torus, as shown in figure 2.3(d). This suggests there are two relevant time scales for the formation of a torus with our technique: the break-up time of the jet [39], $t_b \approx \eta_o a_{tip}/\Gamma$, with a_{tip} the inner diameter of the needle, η_o the viscosity of the outer liquid and Γ the interfacial tension, and the time required to perform a full rotation, $T = 2\pi/\omega = 2\pi R_{tip}/v_o$, with R_{tip} the distance from the needle to the rotation axis and $\omega = v_o/R_{tip}$ the angular speed. By balancing these two time scales, we obtain the velocity needed to form a torus, $v_o = 2\pi(R_{tip}/a_{tip})(\Gamma/\eta_o)$, which we can recast in terms of a capillary number: $Ca_o \equiv \eta_o v_o/\Gamma \approx 2\pi R_{tip}/a_{tip}$. This expression provides a means to predict when a torus will form using our experimental method. To test its validity, we

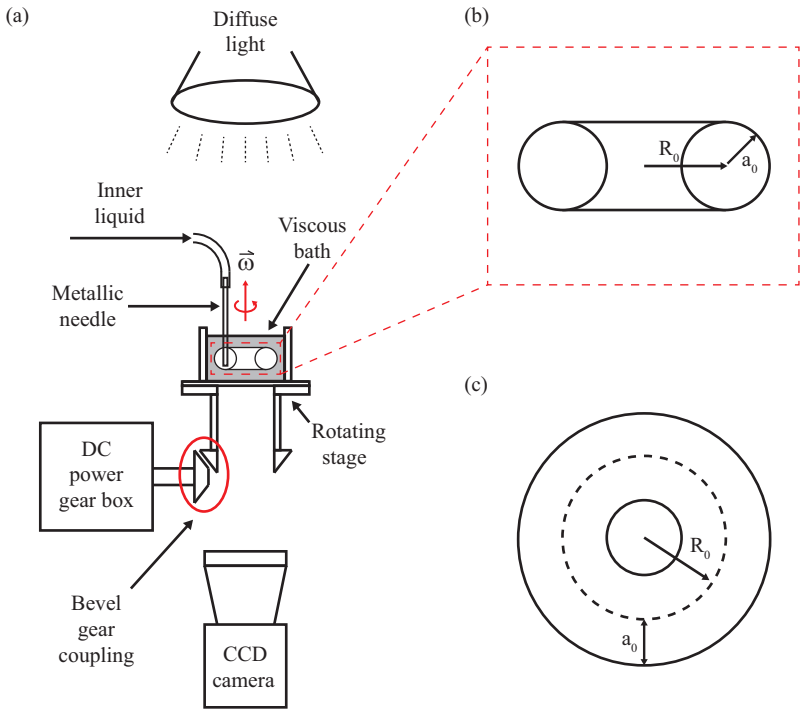

Figure 2.1: The schematic of: (a) experimental setup to generate the toroidal droplet by injecting a liquid through a metallic needle into a bath containing another imisible liquid rotating at angular velocity ω, (b) side view and (c) top view of the torus, with unperturbed tube radius a_0 and overall radius R_0.

varied R_{tip} and v_o for different values of η_o and visually identified when a torus is formed. We summarize our observations in terms of Ca_o and R_{tip}/a_{tip} in figure 2.3(e). The line in this plot separates regions where a torus forms from regions where a torus does not form; it passes through the origin and has a slope of 2.2, which is an acceptable value in comparison with the prefactor value of 2π.

Our method provides great flexibility in tuning the aspect ratio of the torus. On the one hand, its initial overall size, which we quantify by its initial overall radius, R_0, with $R_0 = R_{tip}$, is determined by the position of the injection needle with respect to the rotation axis. On the other hand, the injection flow rate and injection time determine the volume of the torus and thus the initial radius of its tube, a_0. To show this, we made a series of tori all with $R_0 = 8$ mm, for different injection times, t_i, while keeping the injection flow rate equal to $q_i = 50$ ml/hr; in this way, we change the infused volume, $V = q_i t_i$. We find that a_o increases with V/R_0, as shown in figure 2.4; this dependence quantitatively agrees with what would be expected for a torus, whose volume is equal to $V = 2\pi^2 a_0^2 R_o$, as shown by the line in the same figure. Thus our method also provides a simple

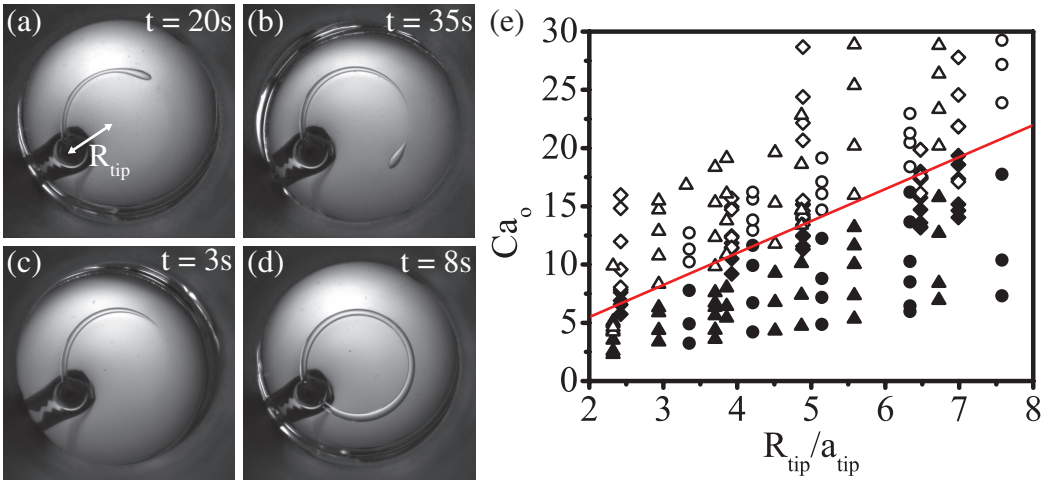

Figure 2.2: (a,b) Formation and breakup of a curved jet. In this experiment, the rotation speed is insufficient and the torus does not form. Instead, the jet breaksup before the torus is generated. (c,d) If the rotation is sufficient, the jet can travel the whole circle and form a toroidal droplet once it closes in on itself. (e) Diagram for the formation of toroidal droplets in terms of the capillary number of the outer liquid, Ca_o, and R_{tip}/a_{tip}, where R_{tip} is the distance between the needle and the rotation axis. The line corresponds to $Ca_o = 2.2R_{tip}/a_{tip}$. The different symbols correspond to different values of η_o: ($\diamond$, $\blacklozenge$) 30000 cP, ($\circ$, $\bullet$) 10000 cP, ($\triangle$ $\blacktriangle$) 5000 cP. We use water for the inner liquid and silicone oil for the outer liquid and always add the surfactant sodium dodecyl sulphate above its critical micelle concentration to decrease the interfacial tension to $\Gamma \approx 10$ mN/m (see Appendix A).

means to precisely vary the aspect ratio of the torus, $\xi = R_0/a_0$, by independently changing R_0 and a_0. Figure 2.5 illustrates toroidal droplets of different sizes and aspect ratios. We can generate a set of toroidal droplets with similar R_0 and varying a_0 by keeping R_{tip} approximately constant while varying the injected volume, as shown in figure 2.5(a)-(c), or a set of toroidal droplets with similar a_0 and varying R_0 by varying both R_{tip} and volume accordingly, as shown in figure 2.5(d)-(f).

2.3 Rayleigh-Plateau Instability of Toroidal Droplets

After the toroidal droplet is formed, we remove the tip and allow the system to evolve in time while recording the evolution with a CCD camera. For a viscosity ratio of the inner to the outer liquid of $\kappa = \eta_i/\eta_o \approx 1/20$, we observe that the torus breaks into a precise number of droplets; this number depends on its initial aspect ratio, as shown by the series of images in figure 2.6, where we show snapshots for a wide range of ξ. The first row of images corresponds to the initial state, right after the needle is removed, the second row of images corresponds to a time slightly before break-up and

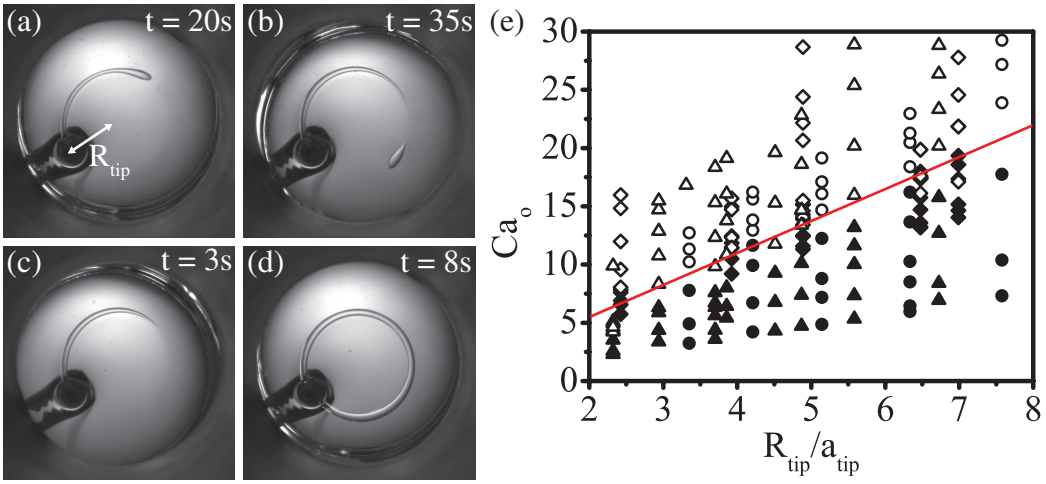

Figure 2.3: (a,b) Formation and breakup of a curved jet. In this experiment, the rotation speed is insufficient and the torus does not form. Instead, the jet breaksup before the torus is generated. (c,d) If the rotation is sufficient, the jet can travel the whole circle and form a toroidal droplet once it closes in on itself. (e) Diagram for the formation of toroidal droplets in terms of the capillary number of the outer liquid, Ca_o, and R_{tip}/a_{tip}, where R_{tip} is the distance between the needle and the rotation axis. The line corresponds to $Ca_o = 2.2R_{tip}/a_{tip}$. The different symbols correspond to different values of η_o: ($\diamond$, $\blacklozenge$) 30000 cP, ($\circ$, $\bullet$) 10000 cP, ($\triangle$ $\blacktriangle$) 5000 cP. We use water for the inner liquid and silicone oil for the outer liquid and always add the surfactant sodium dodecyl sulphate above its critical micelle concentration to decrease the interfacial tension to $\Gamma \approx 10$ mN/m (see Appendix A).

the third row of images corresponds to the end of the process, right after breakup had occurred. We obtain the same number of droplets for a well defined range of aspect ratios, implying that the number of break-up points in the torus, n, as a function of ξ is a step function, as shown in figure 2.7; each step is associated with a certain range of aspect ratios, all for the same n.

The observed break-up into a specific and discrete set of droplets implies that only wavelengths which are integer fractions of the overall length of the torus can induce its break-up. Consequently:

$$2\pi R_0 = n\lambda \tag{2.1}$$

with λ the wavelength associated to the mode inducing the break-up. ξ controls the number of wavelengths that fit inside the torus and consequently the number of droplets that result from its break-up.

Interestingly, we observe that the torus often shrinks before it breaks-up into drops. For a given initial aspect ratio, the overall radius of the torus decreases until break-up occurs; this explains the presence of steps in figure 2.7(a). Furthermore, we observe that the torus breaks when the aspect

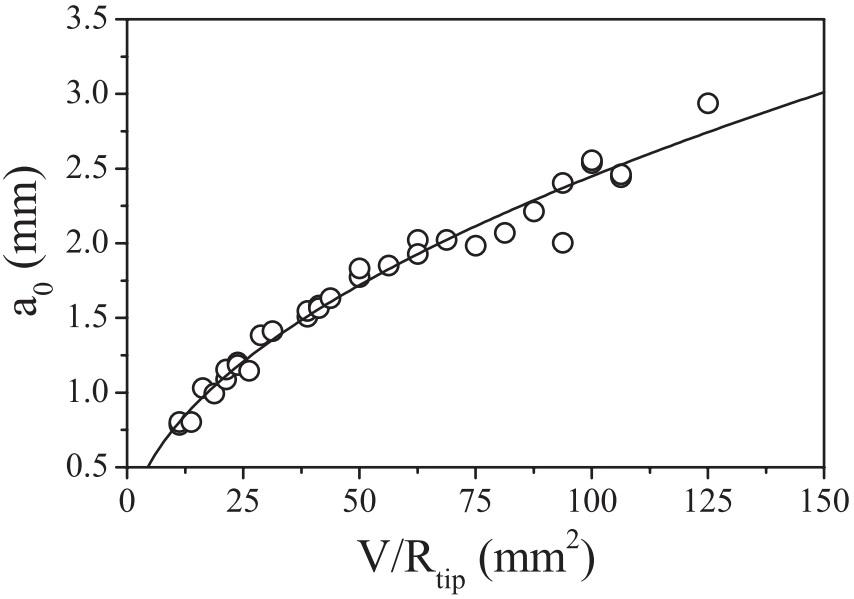

Figure 2.4: Diagram showing resulting tube radius as a function of the injected volume V and R_{tip}. The line represents $a_0 = \sqrt{V/2\pi^2 R_{tip}}$.

ratio reaches the leftmost point of the step. For example, a torus in figure 2.7(b) which has an initial aspect ratio of $\sim$ 10 and is indicated by the position of the arrow in figure 2.7(a) will evolve into the torus in figure 2.7(c) which has the aspect ratio of $\sim$ 8.3, corresponding to the leftmost point in the step; at this point, the torus will break into five large droplets of similar size, as shown in figure 2.7(d). Based on this observation, we hypothesize that when the torus reaches the leftmost point of each step, the mode inducing the observed n-breakup corresponds to the mode with the largest growth rate possible; among all unstable modes, there is one which is the fastest [40] and we believe it is this mode that is responsible for the break-up. Based on this hypothesis, a torus will shrink only until n wavelengths of this fastest mode can fit in the available contour length. As a result, irrespective of the aspect ratio, it is always the same mode that causes the break-up of the torus, with the only difference being the number of wavelengths that can fit in its contour length. Consistent with this hypothesis, the leftmost points of each step in figure 2.7(a) scale linearly with the aspect ratio, as shown by the linear fit in the same figure. We obtain $n \approx 0.57\xi$, which we can re-write as $(n/R_0)a_0 = (2\pi/\lambda)a_0 \approx 0.57$ using equation 2.1; this provides the wavelength of the fastest unstable mode in our experiments. Remarkably, the classical stability analysis of Tomotika for a viscous cylindrical jet inside another viscous liquid [43] predicts that the unstable mode with largest

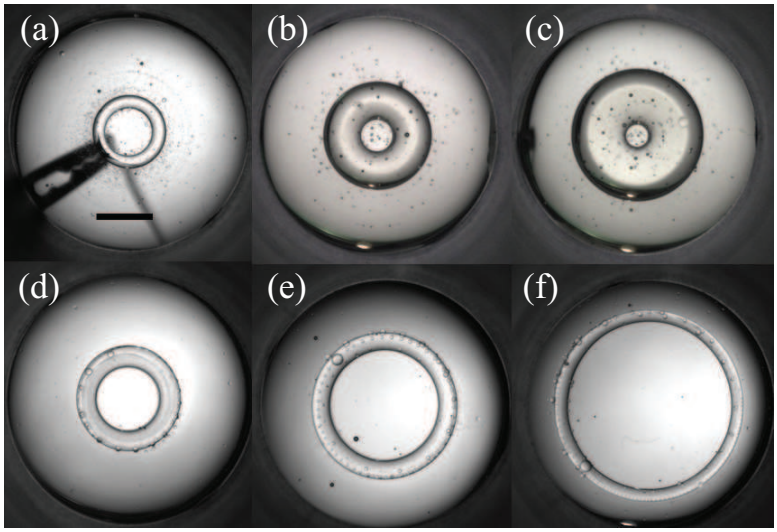

Figure 2.5: Tori of different size and aspect ratio. (a)-(c) R_0 approximately constant. (d)-(f) a_0 approximately constant. The scale bar corresponds to 5 mm.

growth rate corresponds to $(2\pi/\lambda)a_0 = 0.54$ for $\kappa \approx 1/20$; this value agrees with our experimental results, confirming our hypothesis.

We recall that for fluid cylinders such that $\kappa \to 0$ or $\kappa \to \infty$, the unstable mode with the largest growth rate corresponds to $\lambda \to \infty$ [43]. This implies that only breakups with small n are expected in these situations. Consistent with this expectation, we only see breakups with $n = 1$ for a low viscosity ratio, $\kappa \approx 1/30000$, as shown in figure 2.8, in contrast to the multiple breakups observed when $\kappa \approx 1/20$ (see figure 2.6). In this case, there is only a single wavelength growing in the torus, and it corresponds to the fastest unstable mode that can grow. The fact that inner circle of breaking toroidal droplets in this viscosity ratio seem to remains circular throughout the breakup (see figure 2.8) also means that we can use it to further investigate the effect of shrinking during the breakup of toroidal droplets in more detail. To do this, we plotted the time evolution of a swelling a_s and necking (breaking) a_n tube radius (see figure 2.9(a)) normalized by the initial tube radius for different ξ in the same graph, as shown in figure 2.9(b). For large aspect ratios, we find that the growth in $a_s(t)$ and the reduction in $a_n(t)$ are symmetric with respect to the initial state, $a_s(0) = a_n(0) = a_0$. If $a_n(t)$ decreases, $a_s(t)$ must increase, since the volume of the torus is conserved. However, the degree of symmetry becomes lower as we decrease the aspect ratio. This indicates that the impact of shrinkage behavior on the breakup of toroidal droplets is more dominant

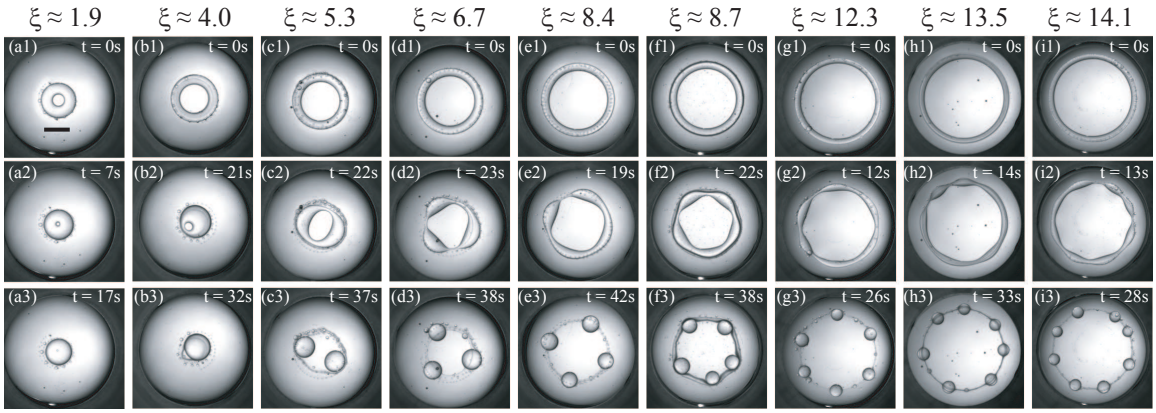

Figure 2.6: Snapshots for the time evolution of a torus (from top to bottom) for different aspect ratios. The scale bar is 0.5 mm. In these experiments, the injected liquid is glycerin and the liquid in the continuous phase is silicone oil ($\kappa \approx 1/20, \Gamma \approx 27$ mN/m, see Appendix A).

at lower aspect ratio. By plotting the inner radius of the torus, $R_{in}(t)$, normalized by the inner initial radius, $R_{in}(0)$, as a function of time, as shown in figure 2.9(c). We confirmed that the torus shrinks towards the center irrespective of the aspect ratio. This behavior is noticeable only at the beginning for large ξ and gradually becomes more relevant throughout the breakup as ξ decreases.

2.3.1 Quantifying Growth Rate

Following Rayleigh's linear stability analysis on cylindrical liquid thread, the deformation of $a_s(t)$ and $a_n(t)$ evolve as $a_0 + \epsilon e^{\sigma t}$ and $a_0 - \epsilon e^{\sigma t}$, respectively, where ϵ is the initial amplitude of the surface perturbation and σ is the growth rate associated with the mode causing the breakup. Hence, if we want to obtain the value of σ, we have to monitor a_s and a_n as a function of time. In the case of $\kappa \approx 1/20$, toroidal droplets often break in multiple locations, thus we assigned index to each individual swelling and necking tube radius. For example, each swelling and necking tube radius of a torus that breaks in five locations are labeled with $a_{s\nu}$ and $a_{n\nu}$, respectively, with the index ν starting from 0 and increment by 1 up until 4 in the clockwise direction for a torus shown in figure 2.10(a). Then the value of σ can be obtained from the slope of the logarithmic plot of either the growth of the relative swell, $a_{s\nu} - a_0$, or the relative neck, $a_0 - a_{b\nu}(t)$, or the difference between swelling and breaking, $a_{s\nu}(t) - a_{n\nu}(t)$, in the linear regime as shown in see figure 2.10(b)-(d); note that in this case we stop monitoring $a_{s\nu}$ and $a_{n\nu}$ after the formation of satellite droplet becomes noticeable. These plots show that the linear trend does not occur right away. Due to the effect

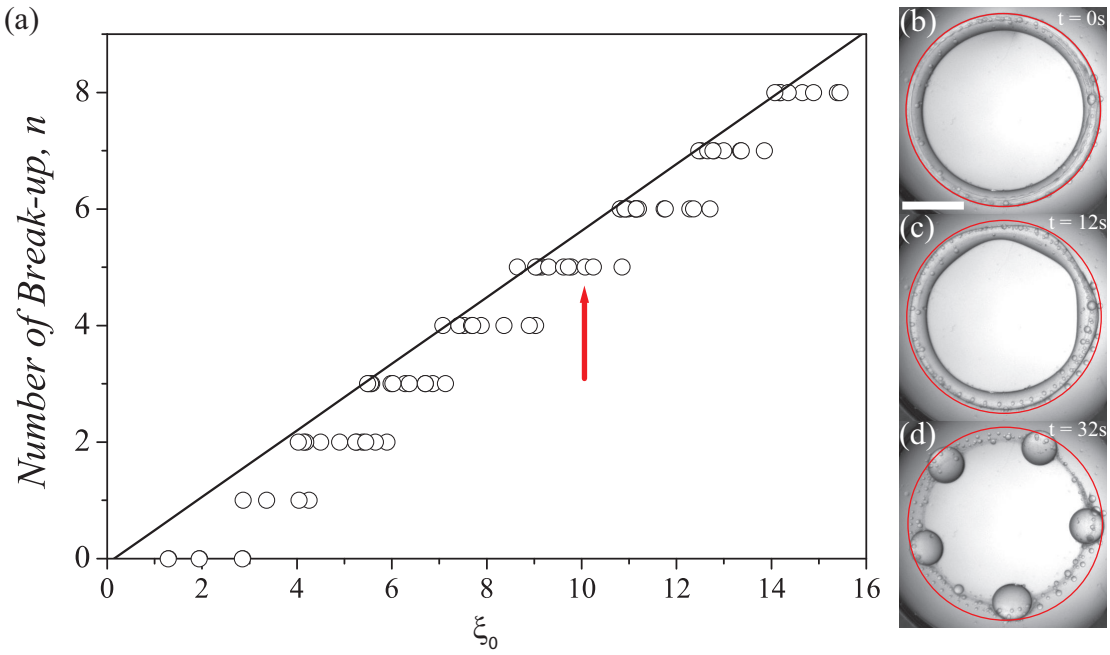

Figure 2.7: (a) Number of break-up points in the torus, n, as a function of its initial aspect ratio, ξ. The line corresponds to a linear fit of the leftmost points in the steps versus the initial aspect ratio, we obtain $n \approx 0.57\xi$. (b-c) Time evolution of a torus made of glycerin immersed in silicone oil ($\kappa \approx 1/20, \Gamma \approx 27$ mN/m). (b) Toroidal droplet right after formation with initial aspect ratio $\xi \approx 10$. (c) After some time the toroidal droplet has shrunk until it can accommodate an integer number of wavelengths of the most unstable mode, $\xi \approx 8.3$. (d) After the breakup, the number of spherical beads left behind indicated the number of wavelengths fitted inside the torus. Red circle in (b)-(d) illustrate outer circumference of the torus at $t = 0$ s. Scale bar in (b) represents 5 mm.

of shrinking of toroidal droplet, there is an overall increase in tube radius which tends to be most prominent at an early time for thin toroidal droplets. This enhances the growth of $a_s(t) - a_0$ while diminishing the growth of $a_0 - a_n(t)$ as they show a sharper and slower increases (or even decreases for some cases), respectively, at the beginning. However, this shrinking effect can be considerably reduced in the case of $a_s(t) - a_n(t)$ as their logarithmic plot seems to be more linear right from the beginning. Similar to the case of $\kappa \approx 1/20$, we also observed similar trend in the logarithmic plot of $a_s - a_0$, $a_0 - a_b(t)$ and $a_s(t) - a_n(t)$ for $\kappa \approx 1/30000$, as shown in figure 2.11.

Then using the same method as [41, 42], the value of σ is taken from the average of all the slopes of all the different logarithmic plots. The results for this is then plotted in terms of dimensionless growth rate, $\sigma\eta_o a_0/\Gamma$, as a function of the dimensionless wave number ka_0 which we rewrite as n/ξ, as shown in figure 2.12. The solid lines correspond to Tomotika's theoretical predictions for a cylindrical viscous thread [43]. Our results show that, without taking the shrinking effect into

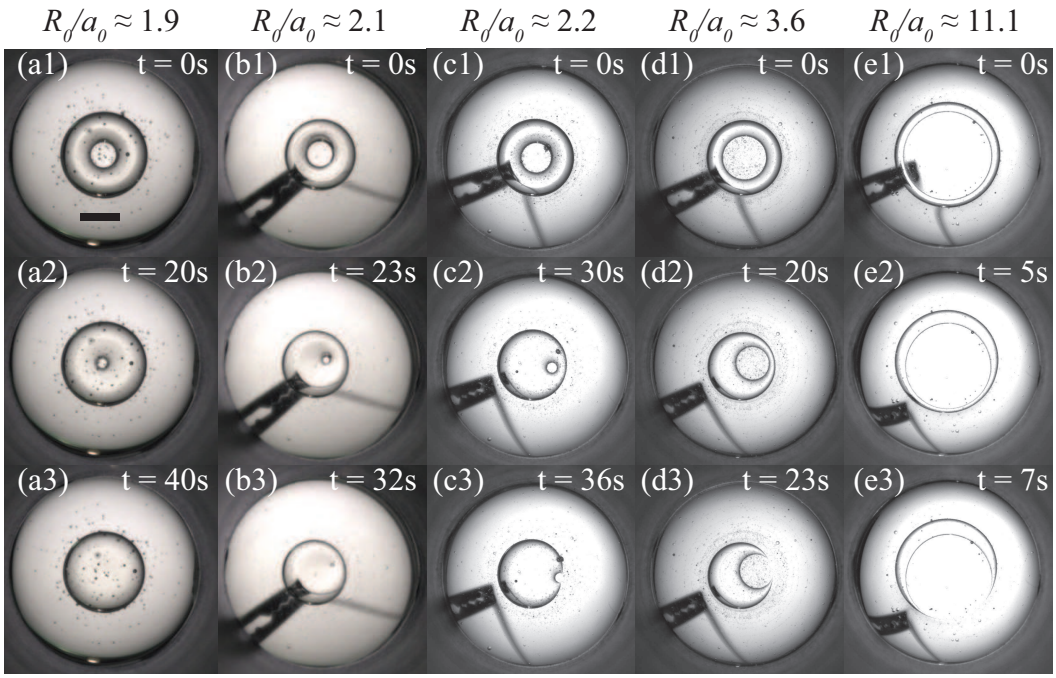

Figure 2.8: Snapshots for the time evolution of a torus (from top to bottom) for different aspect ratios. The scale bar is 0.5 mm. In these experiments, the injected liquid is water with 60 mM Sodium Dodecyl Sulfate (SDS), which is used as a surfactant to lower the surface tension between water and silicone oil, and the liquid in the continuous phase is silicone oil ($\kappa \approx 1/30000, \Gamma \approx 10$ mN/m).

account, the breakup mode of a toroidal droplet is the same as that of a cylindrical threads with its number and size of the associated wavelength is constrained by the aspect ratio of a torus.

For $\kappa \approx 1/20$, we observed that the breakup only occurs near the most unstable mode confirming our hypothesis in the previous section. In this case, the shrinking of a torus is the key which allowing it always accommodate an integer number of wavelength of the most unstable mode. For $\kappa \approx 1/30000$, the size of the wavelength associated with the most unstable mode corresponds directly to the central circumference ($2\pi R_0$) of the torus because the number of breakup n is constraint to 1. Thus allowing us to freely select the breakup mode by changing the aspect ratio of the torus. Hence, we were able to obtained data for broader spectrum of ka_0 in this case. However, we cannot collect data beyond $ka_0 > 0.5$ because beyond this point shrinking behavior dominates and a torus no longer breaks.

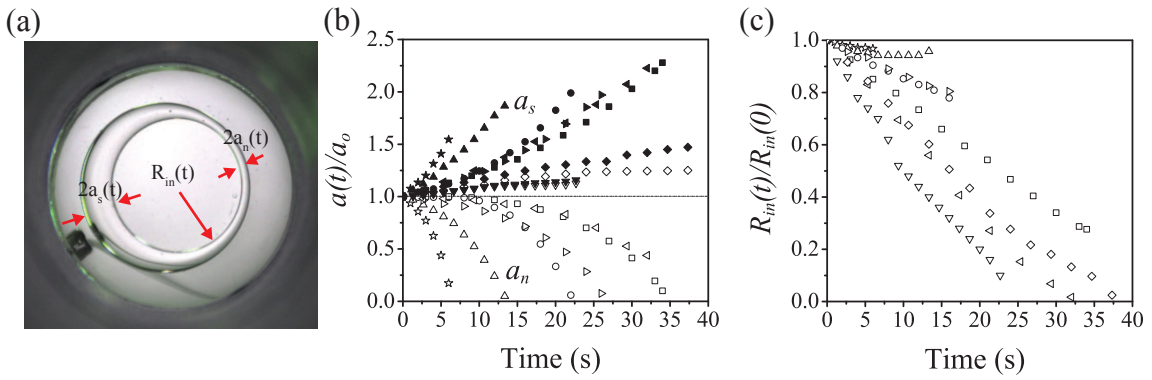

Figure 2.9: (a) Snapshot of breaking toroidal water droplet with the locations of a_s and a_n. (b) Time evolution of the swelling (closed symbols) and neck (open symbols) radii normalized with the initial radius. (c) Time evolution of the torus dimensions, quantified through $R_{in}(t)$ normalized by $R_{in}(0)$, for different values of the aspect ratio: (★,☆) $\xi_0 \approx 11.1$, (▲,△) $\xi_0 \approx 5.6$, (●,○) $\xi_0 \approx 3.6$, (►,▷) $\xi_0 \approx 2.6$, (■,□) $\xi_0 \approx 2.2$, (◄,◁) $\xi_0 \approx 2.1$, (◆,◇) $\xi_0 \approx 1.9$, (▼,▽) $\xi_0 \approx 1.4$.

2.4 Shrinking Instability

For $\xi < 2$, this shrinkage becomes very relevant. In fact, in these situations, there is no break-up and the torus relies on this mechanism in order to transform into a single spherical droplet; the torus simply shrinks towards its center to coalesces onto itself, as shown in column (a) of figure 2.6 and 2.8. As a result, there is no neck anywhere along the contour of the torus and both a_s and a_n increase with time as shown in figure 2.9(b).

Interestingly, the condition $R_0 \approx 2a_0$ corresponds to a torus having a tube radius equal to R_{in}. Based on this measure, the contour length of such torus would be $2\pi R_{in} \simeq 2\pi a_0$. This condition is reminiscent of the classical limit of Plateau and Rayleigh [46, 47] separating stable and unstable modes in a linear tube; only those modes with a wavelength larger than $2\pi a_0$ are unstable. We emphasize, however, that the connection between our experiments and this classical result only holds if R_{in} is taken as the relevant dimension: When $R_{in} \lesssim a_0$, we find that no unstable mode grows in the torus, which simply shrinks to finally form a single spherical droplet.

To quantify this shrinkage behavior, we measure the initial speed, v, of the process and plot the result as a function of a_0 in figure 2.13. We observe that the speed of the shrinkage process does not appreciably depend on a_0. Instead, the speed is constant and equal to $34 \pm 6\,\mu$m/s. To account for this value, we balance the two relevant forces in the process: surface tension, which provides the driving force, and a viscous drag per unit length, which opposes the shrinkage process. We

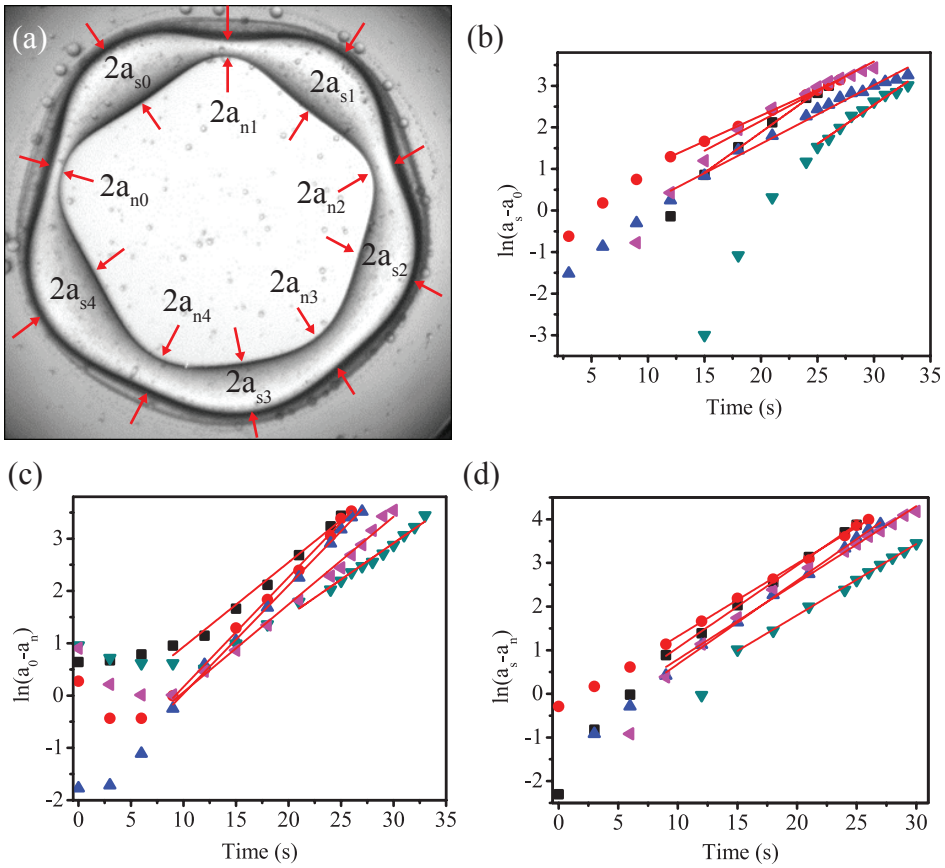

Figure 2.10: (a) Snapshot of breaking toroidal glycerol droplet ($\kappa \approx 1/20$) indicating the locations of a_s and a_n. (b) Natural log plot of the difference between the swelling and the neck radius, (c) the difference between the initial tube radius and the neck, (d) the difference between the swelling and initial tube radius for different regions: ■ (a_{s0}, a_{n0}), ●(a_{s1}, a_{n1}), ▲ (a_{s2}, a_{n2}),▼ (a_{s3}, a_{n4}),◀ (a_{s4}, a_{n4}).

estimate the drag on our tori by considering the drag on a cylinder [48], $F/L = 4\pi\eta_o v/ln(7.4/Re)$, where $Re = \rho v a_0/\eta_o$ is the Reynolds number and L is the length of the cylinder. From the condition $F/L \approx \Gamma$, we get $v \approx 390\,\mu$m/s, which is an order of magnitude larger than the experimental result [49]. This model fails to capture the quantitative picture. However, since the drag only depends on a_0 through the logarithm of Re^{-1} and $Re \approx O(10^{-6})$, v should not depend on a_0, also consistent with our experimental observations. A more accurate model which was able to accurately capture the closing speed of the inner hole of a torus has been proposed by [34, 50]. In this model the shrinking speed of the inner radius

$$\dot{R}_{in}(t) = -\frac{\Gamma}{12\eta_o}\frac{2\xi+1}{\xi^2-1/2}, \tag{2.2}$$

is found by balancing the viscous dissipation, $\dot{E}_{vis} = -24\pi^2\eta_o(\xi^2 - \frac{1}{2})a_0\dot{a}_0\dot{R}_0$ and the surface energy

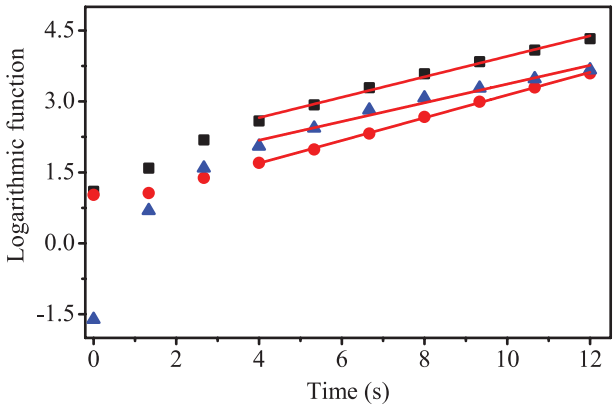

Figure 2.11: Logarithmic plot of: ■ $a_s - a_n$, ● $a_s - a_0$, ▲ $a_0 - a_n$ as a function of time for the breakup of droplet made out of water droplet ($\kappa \approx 1/30000$). The slope of the red line is the grow rate.

dissipation rate, $\dot{F} = 2\pi^2 \Gamma a \dot{R}_0$. For a very thin tori $\xi \to \infty$, $\dot{R}_{in} \to 0$ indicating that there is no shrinking for cylindrical threads.

2.4.1 Free Energy and Laplace Pressure Analysis for Toroidal Droplet

Toroidal droplets breakup due to capillary instabilities in a way that is very similar to the breakup of a cylindrical jet. However, the shrinking process of the toroidal droplets is an *intrinsic* effect that occurs due to its geometry. We can prove this statement by first looking at the surface free energy, which can be written as $F = \Gamma A$, where $A = 4\pi^2 R_0 a_0$ is the surface area of a torus. Since the system will always try to minimize the surface free energy, it will always evolve in such a way that $\dot{F} < 0$. By taking the time derivative of F and then replacing a_0 with $\sqrt{V/2\pi^2 R_0}$, we obtain [34, 50]:

$$\dot{F} = 2\pi^2 \Gamma a_0 \dot{R}_0 \,. \tag{2.3}$$

This equation can only be negative when $\dot{R}_0 < 0$, which implying that the toroidal droplets must always shrink.

An alternative way to show that the toroidal droplets must shrink is to consider the jump in pressure across the interface of a toroidal droplet's surface at different locations using the Laplace's equation [34, 50]:

$$p - p_0 = \Gamma H \,, \tag{2.4}$$

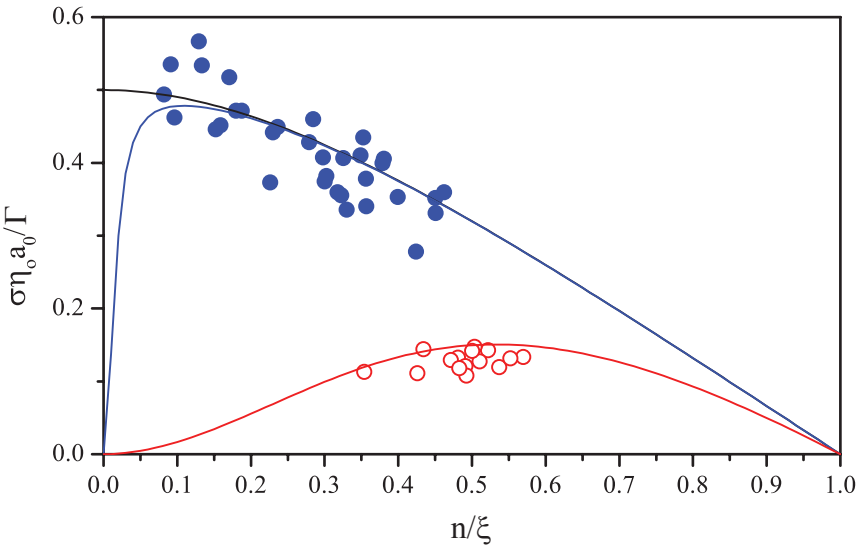

Figure 2.12: Dispersion curve for toroidal glycerin droplets in 30000 cP silicone oil. Each point represents the breakup of one toroidal droplet. The line is the theoretical result of Tomotika's calculation for $\kappa \approx 1/20$ respectively. $\Gamma \approx 27$ mN/m. Dispersion curve for toroidal water droplets in 30000 cP Silicone Oil. Each point represents one toroidal droplet. The black and blue lines are the theoretical result of Tomotika's calculation for $\kappa \to 0$ and $\kappa \approx 1/30000$ respectively. The surface tension is approximately 10 mN/m.

where $H = \frac{R_0+2a_0\cos\alpha}{a_0(R_0+a\cos\alpha)}$ is the mean curvature of a toroidal surface (assuming that a_0 is constant) with α as the polar angle, as shown figure 2.14. By taking the difference between pressure at the exterior of the drop, where $(r = a_0, \alpha = 0)$, and pressure at the interior of the drop, where $(r = a_0, \alpha = \pi)$ we obtain: $p(r = a_0, \alpha = 0) - p(r = a_0, \alpha = \pi) = \frac{2\Gamma\xi}{a(\xi^2-1)}$. Since for a torus, ξ is always greater than one and as a result $p(r = a_0, \alpha = 0) > p(r = a_0, \alpha = \pi)$ driving the fluid from the exterior to the interior of toroidal droplet. Again for a very thin toroidal case $\xi \to \infty$, $p(r = a_0, \alpha = 0) - p(r = a_0, \alpha = \pi) \to 0$ indicating that there is no shrinkage for a cylindrical jet and confirming that the shrinking process is unique only to droplets with the toroidal geometry.

2.4.2 Calculation of Pressure Distribution inside of Toroidal Droplet

For a collapsing toroidal droplets in our experiments, the Ohnesorge number is large ($Oh \equiv \sqrt{\eta_o^2/\rho a_0\Gamma} >> 1$ with ρ as the density of the droplet) indicating that the velocity $\vec{v}$ and pressure p of the fluid can be described using the Stokes equation:

$$0 = -\vec{\nabla}p + \eta\Delta\vec{v}. \tag{2.5}$$

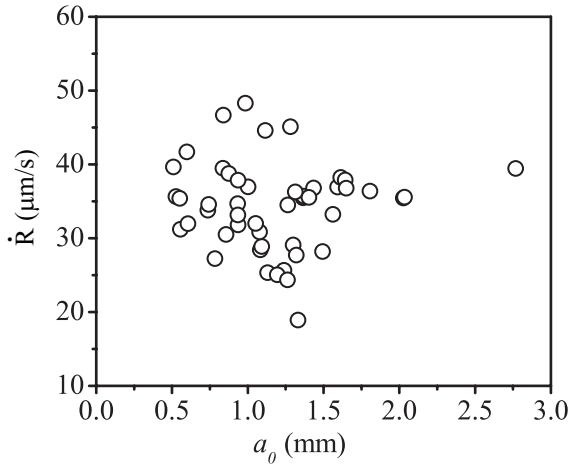

Figure 2.13: Velocity of the shrinkage process as a function of the initial tube radius a_0. The velocity is equal to 34 ± 6 μm/s and independent of a_0.

For an incompressible fluid, $\vec{\nabla} \cdot \vec{v} = 0$, we can write $\vec{v} = \vec{\nabla} \times \vec{\psi}$, where $\vec{\psi}$ is the vector potential. Then by taking the divergence of the equation (2.5), we obtain the equation:

$$\Delta p(r, \alpha) = 0\,. \tag{2.6}$$

Thus, the problem of finding the pressure distribution inside a toroidal droplet consist of solving the Laplace's equation (2.6) with equation (2.4) as the boundary condition.

Following the calculation in [34, 50], the pressure and the velocity distribution inside toroidal droplet were solved using toroidal coordinates:

$$\vec{x} = \begin{pmatrix} \frac{d \sinh\zeta \cos\theta}{\cosh\zeta - \cos\chi} \\ \frac{d \sinh\zeta \sin\theta}{\cosh\zeta - \cos\chi} \\ \frac{d \sin\chi}{\cosh\zeta - \cos\chi} \end{pmatrix} \tag{2.7}$$

where $\cosh\zeta = R_0/r$, $d = r\sinh\zeta$ is the radius of the reference circle in figure 2.15(b), and $\cos\chi = \frac{(R_0/r)\cos\alpha + 1}{(R_0/r) + \cos\alpha}$ with (r, α, θ) defined in figure 2.14(b). To better understand what the components in toroidal coordinates means in the physical space, we look at how to generate toroidal surface using the coordinates. First to generate the cross-section of a toroidal tube, ζ is kept constant and then χ is swept from 0 to 2π; note that each different circle in figure 2.15 represents different ζ. Then the solid torus can be generated by revolving these circles about the z-axis.

In toroidal coordinates, after taking into account the rotational symmetry about the z-axis,

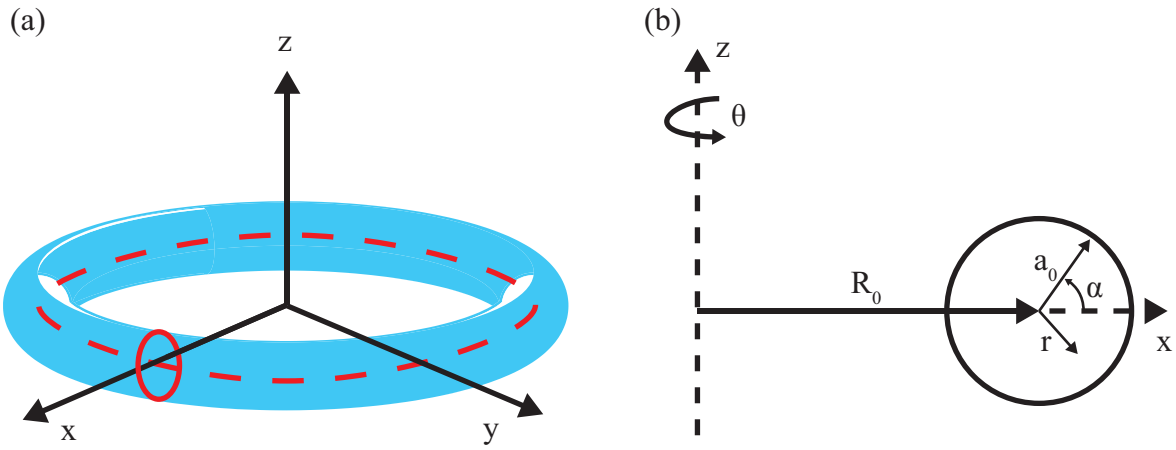

Figure 2.14: Azimuthal toroidal coordinates: (a) 3D schematic of the torus, and (b) the cross section of the tube as indicated in by the red circle in (a).

Laplace equation (2.6) reduces to 2 dimensional problem:

$$\Delta p(\zeta,\chi) = \frac{(\cosh\zeta - \cos\chi)^3}{d^2 \sinh\zeta}\left(\frac{\partial}{\partial\zeta}\left[\frac{\sinh\zeta}{\cosh\zeta-\cos\chi}\frac{\partial p}{\partial\zeta}\right] + \frac{\partial}{\partial\chi}\left[\frac{\sinh\zeta}{\cosh\zeta-\cos\chi}\frac{\partial p}{\partial\chi}\right]\right) = 0\,. \tag{2.8}$$

This equation has the general solution [51]:

$$p(\zeta,\chi) = \sum_{\nu\in\mathbb{Z}} \alpha_\nu \sqrt{\cosh\zeta - \cos\chi}\begin{Bmatrix} P^0_{\nu-1/2}(\cosh\zeta) \\ Q^0_{\nu-1/2}(\cosh\zeta)\end{Bmatrix}\begin{Bmatrix}\cos\nu\chi \\ \sin\nu\chi\end{Bmatrix}. \tag{2.9}$$

The solution is the linear combination of all permutations of the terms inside the curly brackets, where $P^0_{\nu-1/2}(\cosh\zeta)$ and $Q^0_{\nu-1/2}(\cosh\zeta)$ are the Associated Legendre functions of the first and second kind, respectively. Since the pressure must be finite as $r \to 0$ or equivalently when $\cosh\zeta \to \infty$, $Q^0_{\nu-1/2}(\cosh\zeta)$ is the only acceptable term in the solution because it is the only one that converges when $\cosh\zeta \to \infty$; it converges to $\pi/\sqrt{2}$ if $\nu = 0$ and to zero if $\nu \neq 0$. Note also that $\sin\nu\chi$ is eliminated because the pressure must be symmetric above and below the xy plane at $z = 0$. Thus the acceptable solution is [34, 50]:

$$p(\zeta,\chi) = \sum_{\nu\in\mathbb{Z}} \alpha_\nu \sqrt{\cosh\zeta - \cos\chi}\, Q^0_{\nu-1/2}(\cosh\zeta)\cos\nu\chi\,, \tag{2.10}$$

where the coefficients α_ν are determined numerically by matching the pressure at the liquid interface boundary conditions, equation (2.4). We always expand equation (2.10) up to the fifth-order term

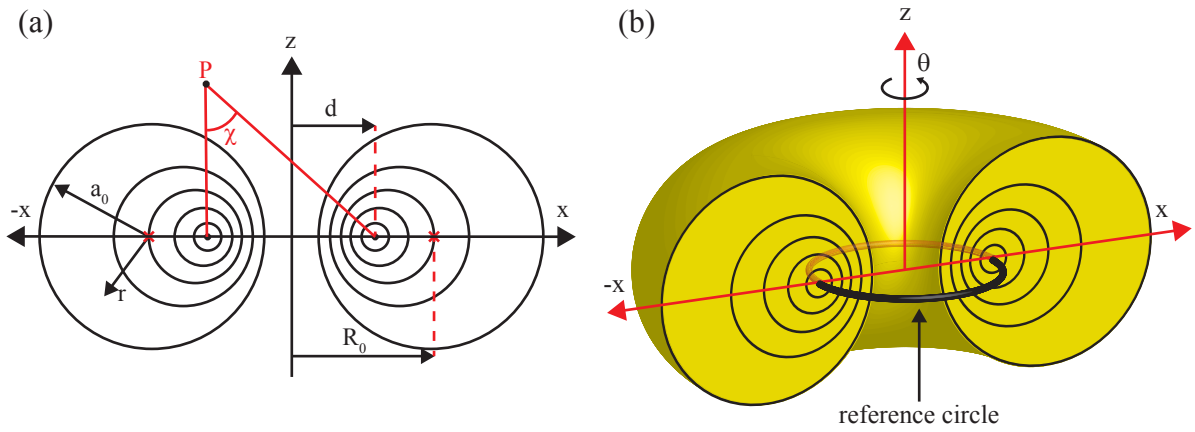

Figure 2.15: (a) Bipolar coordinates with ζ isosurfaces; foci are at (-d,0) and (d,0). (b) A torus is generated by rotating the circle around the z-axis.

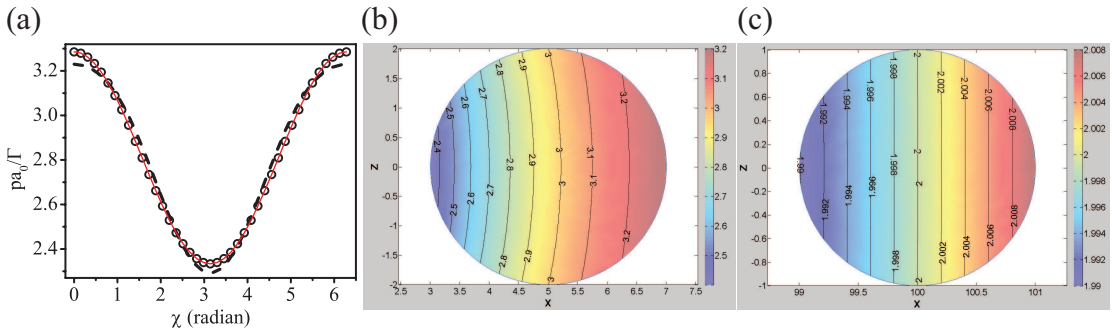

Figure 2.16: (a) Diagrams of pressure at the interface of the toroidal droplet, $\xi = 5/2$. The dashed and solid line each represents the fit from the equation (2.10) expanded up to the first ($\nu = 1$) and fifth-order ($\nu = 5$), respectively with the points representing the pressure calculated using equation (2.4). (b,c) Pressure distribution inside the cross section of the tube of the toroidal droplet for $\xi = 5/2$ and $\xi = 100$, respectively

because this provides a better fit to the boundary pressure. As an example, in figure 2.16(a), we compare the fit using the first-order (dashed line) and fifth-order (solid line) to the expected pressure normalized by Γ/a_0 for $\xi = 5/2$; note also that we set the external pressure p_0 to 1. We illustrate the corresponding normalized pressure magnitude in the cross section of the tube using a colormap, as shown in figure 2.16(b), where we can clearly see that the pressure is greatest at the exterior ($r = a_0, \alpha = 0$) and gradually decreases to smallest as we move toward the interior of the torus ($r = a_0, \alpha = \pi$). Thus driving the liquid in the cross section toward the interior causing the torus to shrink. For a large ξ, the pressure distribution is almost constant, as shown in figure 2.16(c) for $\xi = 100$, emphasizing that there is no shrinkage for a cylindrical thread.

2.4.3 Calculation of Velocity Distribution inside Toroidal Droplet

If we take a curl of the Stokes equation (2.5) and imposing $\vec{v} = \vec{\nabla} \times \vec{\psi}$ and fixing $\vec{\psi}$ by applying the transverse (or Coulomb) gauge, $\vec{\nabla} \cdot \vec{\psi} = 0$, we get a bi-harmonic equation:

$$\Delta^2 \vec{\psi} = 0\,. \tag{2.11}$$

Due to the azimuthal symmetry of the system, all components of $\vec{\psi}$ except the θ component, ψ_θ, must vanish. Equation (2.11) can then be simplified to a scalar differential equation in toroidal coordinates [52]

$$E^2(E^2\psi_\theta) = 0\,, \tag{2.12}$$

where E is a second-order partial differential operator, defined by:

$$E^2 = wh^2\left[\partial_\zeta\left(\frac{1}{w}\partial_\zeta\right) + \partial_\chi\left(\frac{1}{w}\partial_\chi\right)\right], \tag{2.13}$$

with $w = \frac{d\sinh\zeta}{\cosh\zeta - \cos\chi}$ and $h = \frac{\cosh\zeta - \cos\chi}{d}$. The general solution to equation (2.12) is [52]

$$\psi_\theta(\zeta,\chi) = \frac{d\sinh\zeta}{(\cosh\zeta - \cos\chi)^{3/2}} \sum_{\nu\in\mathbb{Z}} \begin{Bmatrix} P^1_{\nu+1/2}(\cosh\zeta) \\ Q^1_{\nu-3/2}(\cosh\zeta) \end{Bmatrix} \begin{Bmatrix} \cos\nu\chi \\ \sin\nu\chi \end{Bmatrix}. \tag{2.14}$$

where $P^1_\nu(x)$ and $Q^1_\nu(x)$ are the Associated Legendre functions of first and second kind, respectively. We can eliminate $\cos\nu\chi$ from equation (2.14) due the reflection symmetry about the xy plane. It is also required that v_x is finite while v_z is zero at $r = 0$ or when $\cosh\zeta \to \infty$ therefore terms involving $P^1_{\nu+1/2}(\cosh\zeta)$ must also be eliminated. Thus, the physically acceptable solution can be written as [34, 50]:

$$\psi_\theta(\zeta,\chi) = \frac{d\sinh\zeta}{(\cosh\zeta - \cos\chi)^{3/2}} \sum_{\nu\in\mathbb{Z}} C_\nu \sin\nu\chi\, Q^1_{\nu-3/2}(\cosh\zeta)\,. \tag{2.15}$$

Then from $\vec{v} = \vec{\nabla} \times \vec{\psi}$ yields

$$v_\zeta = -\frac{g_{\zeta\zeta}}{\sqrt{|\mathbf{g}|}}\partial_\chi\psi_\theta\,, \tag{2.16a}$$

$$v_\chi = \frac{g_{\chi\chi}}{\sqrt{|\mathbf{g}|}}\partial_\zeta\psi_\theta\,, \tag{2.16b}$$

where $|\mathbf{g}|$ is the determinant of the matric tensor in toroidal coordinates and g_{ij} is its component. Note that $v_\theta = 0$ due to symmetry around the z axis. As a result, we get [34, 50]:

$$v_\zeta = \frac{\cosh\zeta - \cos\chi}{\sinh\zeta}\sum_{\nu\in\mathbb{Z}} C_\nu\Bigg[\frac{3\sinh\zeta\sin\chi}{2(\cosh\zeta-\cos\chi)^{5/2}}(\sin\nu\chi) - \frac{\sinh\zeta}{(\cosh\zeta-\cos\chi)^{3/2}} (\nu\cos\nu\chi)\Bigg]Q^1_{\nu-3/2}(\cosh\zeta)\,, \tag{2.17a}$$

$$v_\chi = \frac{\cosh\zeta - \cos\chi}{\sinh\zeta}\sum_{\nu\in\mathbb{Z}} C_\nu\Bigg[\frac{5-4\cosh\zeta\cos\chi-\cosh 2\zeta}{4(\cosh\zeta-\cos\chi)^{5/2}}Q^1_{\nu-3/2}(\cosh\zeta)+ \frac{\sinh\zeta}{(\cosh\zeta-\cos\chi)^{3/2}}\partial_\zeta Q^1_{\nu-3/2}(\cosh\zeta)\Bigg]\sin\nu\chi\,. \tag{2.17b}$$

This equation can also be rewritten in terms of Cartesian coordinates as:

$$v_x = v_\zeta\hat{e}_\zeta\cdot\hat{e}_x + v_\chi\hat{e}_\chi\cdot\hat{e}_x\,, \tag{2.18a}$$

$$v_z = v_\zeta\hat{e}_\zeta\cdot\hat{e}_z + v_\chi\hat{e}_\chi\cdot\hat{e}_z\,, \tag{2.18b}$$

where we have used the relation between the unit vectors in toroidal coordinates and in Cartesian coordinates:

$$\hat{e}_\zeta = \frac{(1-\cosh\zeta\cos\chi)\cos\theta}{\cosh\zeta-\cos\chi}\hat{e}_x + \frac{(1-\cosh\zeta\cos\chi)\sin\theta}{\cosh\zeta-\cos\chi}\hat{e}_y - \frac{\sinh\zeta\sin\chi}{\cosh\zeta-\cos\chi}\hat{e}_z\,, \tag{2.19a}$$

$$\hat{e}_\chi = -\frac{\sinh\zeta\sin\chi\cos\theta}{\cosh\eta-\cos\chi}\hat{e}_x - \frac{\sinh\zeta\sin\chi\sin\theta}{\cosh\zeta-\cos\chi}\hat{e}_y + \frac{\cosh\zeta\cos\chi-1}{\cosh\eta-\cos\chi}\hat{e}_z\,, \tag{2.19b}$$

$$\hat{e}_\theta = \sin\theta\hat{e}_x + \cos\theta\hat{e}_y\,. \tag{2.19c}$$

The coefficients C_ν in equation (2.17) can also be found by numerically matching it with velocity at the interface. In order to do find the velocity at the interface, it is assumed that a point (x_0, z_0) at the interface of a toroidal droplet (non-slip boundary condition) with the center of its tube moving at a velocity $\dot{R}_0\hat{e}_x$, as shown in figure 2.17, is moving at a velocity $\dot{R}_0\hat{e}_x + v_r\hat{e}_r$, where $v_r = -\dot{R}_0\frac{a_0}{2R_0}$ is the tube expansion speed (found from taking the time derivative of the volume of a torus) and $\hat{e}_r = \frac{R_0-x_0}{a_0}\hat{e}_x + \frac{z_0}{a_0}\hat{e}_z$. Then by rewriting the boundary velocity in terms of Cartesian coordinates we get:

$$v_{x0} = \dot{R}_0\left(1 - \frac{R_0-x_0}{2R_0}\right)\,, \tag{2.20a}$$

$$v_{z0} = -\frac{\dot{R}_0 z_0}{2R_0}\hat{e}_z\,. \tag{2.20b}$$

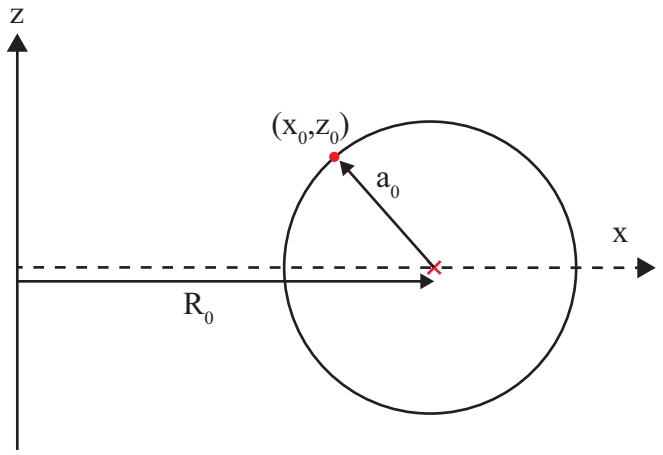

Figure 2.17: A diagram indicating a particle at location (x_0, z_0) at the interface, where the origin is the point at the center of the tube's cross section.

From numerical calculations, we have found that for a thin torus ($\xi = 5/2$), we can vary C_1 in the equation (2.17) until the resulting velocity components at the interface match with the expected velocity from equation (2.20), as shown by the dashed lines in figure 2.18(a,b). Thus the leading order $\nu = 1$ in the velocity is sufficient to describe the velocity field inside a thin toroidal droplet ($\xi >> 1$). However, for a fat torus ($\xi = 5/4$), the velocity plotted using only the first-order $\nu = 1$ deviates from the expected velocity, as shown in figure 2.18(c,d), noticeably for the v_χ component. In order to solve this problem, we expanded the velocity up to the tenth-order and plotted the results together with the velocity with only the first-order term and the expected velocity (see the solid red lines in the figure 2.18). From the comparison in figure 2.18(c,d), we can see that, for a fat torus, the results calculated by expanding the velocity up to the tenth-order term fit the expected velocity better than the results from the velocity with only the first-order term. There is no difference in the first and tenth order expansion fits with the expected boundary velocity in the thin torus case, as shown in figure 2.18(a,b).

To get a better comparison on how accurate the first and the tenth-order velocity expansion fits for the expected interface boundary velocity are for a fat torus ($\xi = 5/2$), we plotted both the first and tenth-order expansion velocity components on top of the expected velocity field at the interface, as shown in figure 2.19(a) and (b), respectively. From this illustration, both the first and tenth-order velocity expansions fit the boundary velocity very well near the interior ($r = a_0, \alpha = \pi$) of the torus;

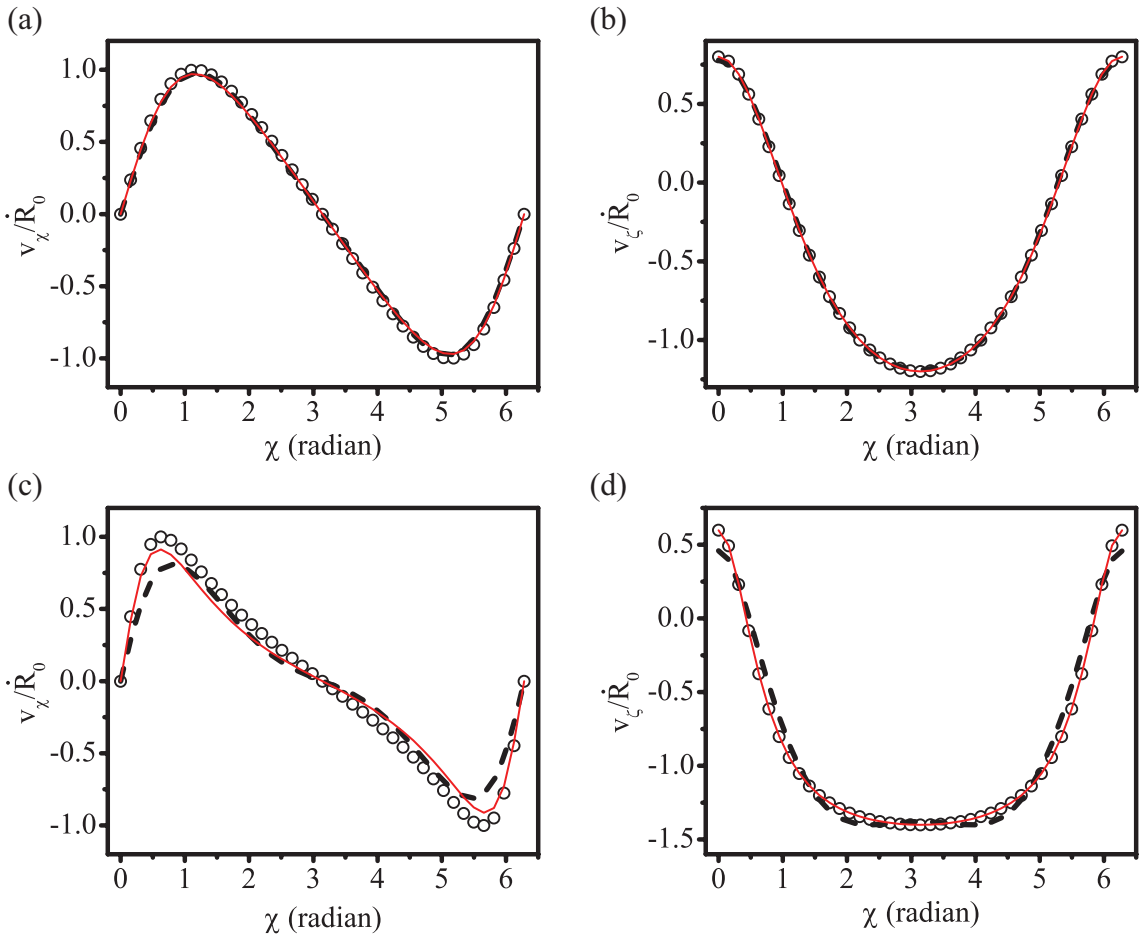

Figure 2.18: Diagrams of matching velocity components v_χ and v_ζ at the interface with a no-slip boundary condition. (a,b) are the fits for thin torus, $\xi = 5/2$. (c,d) are the fits for the fat torus, $\xi = 5/4$. The solid lines are the fits using the expansion of the velocity up to tenth-order ($\nu = 10$), the dashed lines are the fits using only the first-order ($\nu = 1$) of the velocity expansion, and the points are the velocity field calculated using equation (2.20).

however, the vectors plotted using only the first-order term become less accurate toward the exterior ($r = a_0, \alpha = 0$) of the torus, while the velocity with more terms in the expansion remains accurate. This comparison becomes very clear when observed in the magnified view, as one of the vectors of the velocity of only the first-order term is about one third shorter than the expected value (see figure 2.19(a)), while the vector of the velocity with more terms in the expansion fits the expected velocity vector almost perfectly (see figure 2.19(b)). Therefore, all of the velocity vector fields are plotted up to the tenth-order term.

We plotted the theoretical velocity field showing a cross section of a tube moving to the left toward the center of a torus for different ξ, as shown in figure 2.20(a1)-(d1) for a laboratory frame.

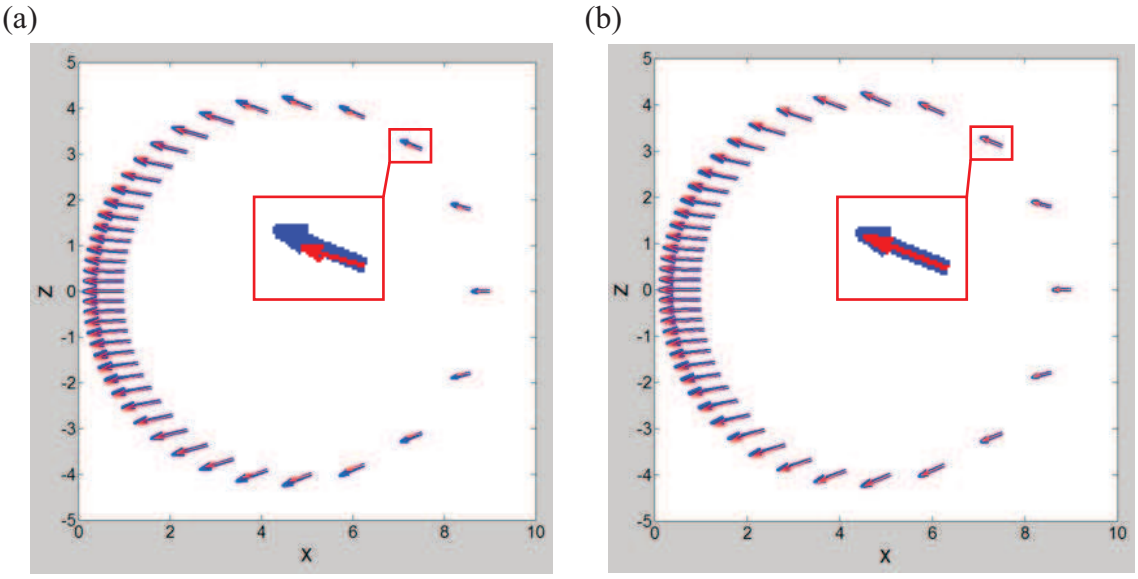

Figure 2.19: The fitting velocity at the interface of a fat torus with $\xi = 5/2$: (a) a fit using the velocity expansion to the first-order ($\nu = 1$), and (b) a fit using the velocity expansion up to tenth order. The blue arrow indicates the velocity derived from the boundary conditions and the red arrow indicates the velocity derived from the theoretical equation.

In this frame of reference, the direction of the velocity field indicates that toroidal droplets shrink irrespective of the value of ξ, which is consistent with our experimental results. We can also see that the speed distributions are greater near the interior ($r = a_0, \alpha = \pi$) of the torus and gradually decrease as we move toward the exterior ($r = a_0, \alpha = 0$) of the torus. This contrast also gradually becomes more noticeable as ξ decreases. Then by subtracting the shrinking speed from the velocity field, we can see the existence of a source, which is the center of expansion of a tube's cross-section where velocity is zero, as shown in figure 2.20(a2)-(d2). Here, the existence of a source indicates growth in the cross-section. Here we can clearly see that the location of a source moves closer to the interior ($r = a_0, \alpha = \pi$) of a torus as ξ gets smaller. Notice also here that in a very thin torus case, cross-sectional growth is reminiscent of the swelling region of a breaking torus or of a cylindrical jet. In addition, we also mapped the vorticity onto the velocity field after subtracting a shrinking speed to see how the flow circulates inside of a cross-section. From the observation, the locations of the maximum vorticity move toward the interior ($r = a_0, \alpha = \pi$) of a torus with decreasing ξ. The sign of vorticity also indicates that the circulation is counter clockwise for the cross section above $z = 0$ and clockwise below $z = 0$.

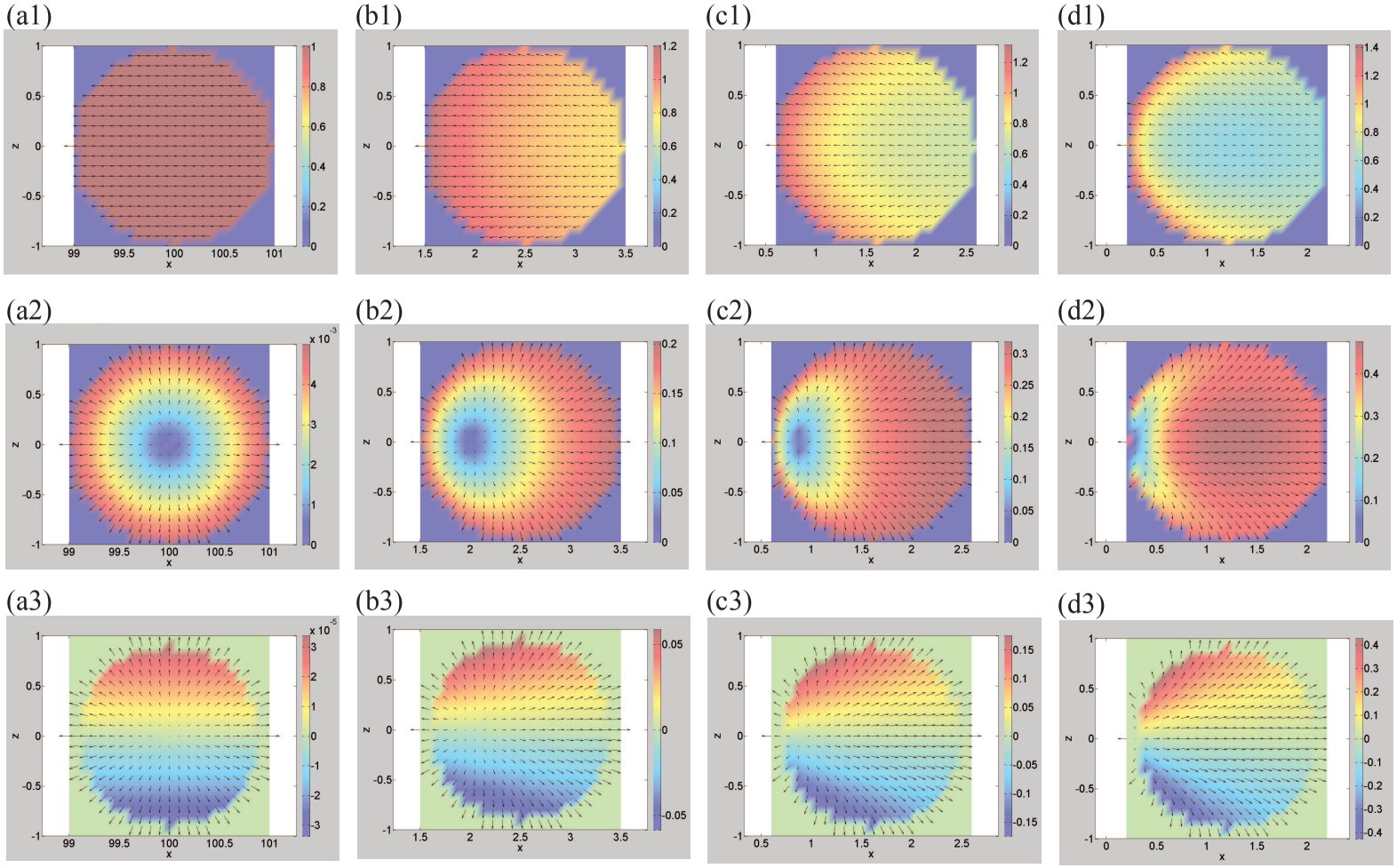

Figure 2.20: The velocity field inside the toroidal droplet in the xz-plane: (a1)-(d1) are the velocity fields in the stationary frame for $\xi = 100$, $\xi = 5/2$, $\xi = 8/5$ and $\xi = 5/4$, respectively. (a2)-(d2) and (a3)-(d3) are the corresponding velocity fields in the co-moving reference frame of center of the tube mapped with the speed and vorticity, respectively. All of the velocities and vorticities are normalized by the shrinking speed $\dot{R}_0$.

2.5 *PIV Analysis of the Collapsing Toroidal Droplets*

Particle Image Velocimetry (PIV) involves monitoring changes in the optical heterogeneity created by the movement of tracer particles and then creating corresponding vector fields. These vector fields can accurately describe the position, velocity, and vorticity of a moving medium. In order to use PIV to study a medium, one must first design a method for accurately capturing the movement of this optical heterogeneity. Typically, such methods involve a light sheet shining through the medium and a CCD camera to capture the motion. Once videos have been captured, they can be analyzed with PIV analysis software. Our goal in this experiment is to capture the flow field of the cross-section of the tube of the torus as it is collapsing and compare it to the theoretical prediction in [34, 50].

2.5.1 Preliminary Test

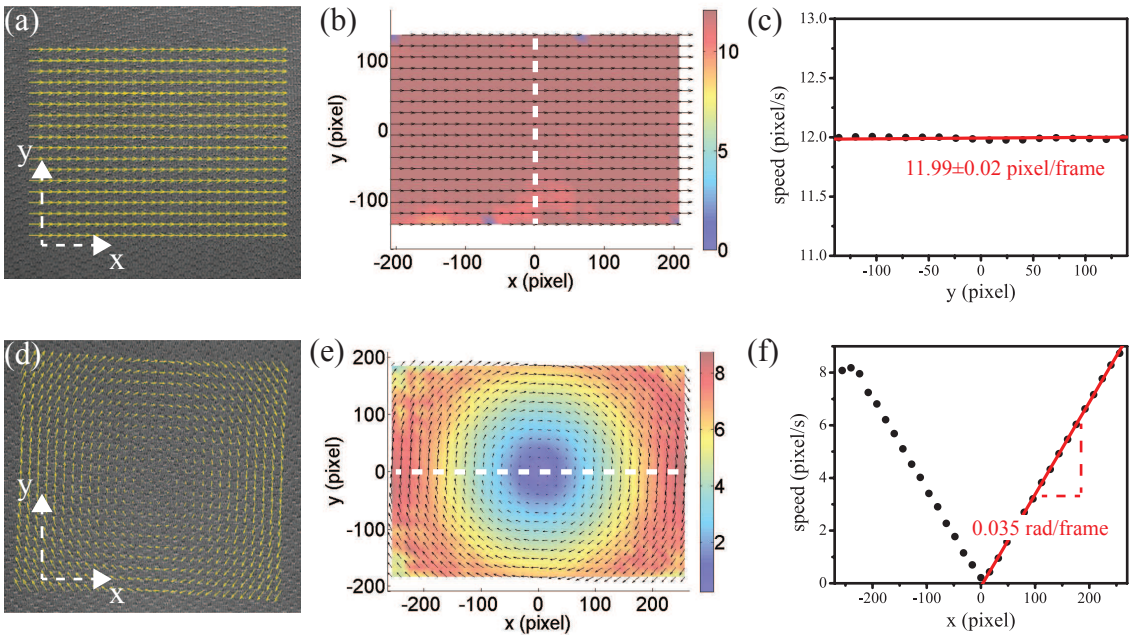

Figure 2.21: (a) A snapshot of a computer generated translating substrate video superimposed by the displacement vector fields generated by the OpenPIV program. (b) Displacement vectors in (a) mapped with colors corresponding to their magnitude. The color bar indicates the speed in pixel/frame. (c) Plot of the speed across the dashed line drawn in (b). (d)-(f) are equivalent to (a)-(c) for computer generated rotating substrate.

In order to verify that the PIV analysis of the flow field of shrinking torus is accurate, we will be performing several tests with known results. The first test that we are going to do is to

check the accuracy of the image-processing software. The software that we use to analyze our flow field images is an open source portable interactive software package called OpenPIV [53]. To verify its accuracy, we used it to analyze two sets of imaging sequences with known parameters that simulated linear translational and rotational motion of particles. These set of sequences were computer-generated by continuously displacing and rotating an image of a pattern substrate. The first substrate was set to move to the right at 12 pixel/frame and the second set was set rotate clockwise at 2° or $\pi/90$ radian/frame, both at a constant rate.

During the analysis, the program displayed a vector field on top of each image to match the displacement between the current and the next image. As a result, a vector field pointing to the right is shown in the analysis for a translating substrate, as shown in figure 2.21(a). After the program finished analysis, the data extracted from the analysis can be replotted with color map representing the magnitude of the vectors, as shown in figure 2.21(b). Here we see that the color on the plot is mostly uniform indicating uniform movement. Then by plotting the speed along the white line in figure 2.21(b), we can extract the quantitative measurement of the speed, as shown in figure 2.21(c). The value of the speed of 11.99 ± 0.02 pix/frame that we obtained from the plot accurately matches with expected value. For a rotating substrate, a vector field indicating circular motion is shown on top of the image during the analysis, as shown in figure 2.21(d). The color map of the corresponding vector field shows a change in color from blue in the center to red as we move to the outer edge of the plot indicating an increase in speed from the center to the edge of rotation (see figure 2.21(e)). Then to better confirm if the program analysis is able to accurately captured the right motion, we plotted the speed of each vector along the line shown in figure 2.21(e), as shown in figure 2.21(f). This plot shows a constant increase of speed from the center to outer edge indicating a uniform rotation and in addition the slope of the graph has magnitude of 0.035 rad/frame accurately matching the expected value. The vector fields and their magnitude from the analysis show good agreement in both of our set values with less 1% discrepancy.

After the accuracy of the image analysis program has been verified, the next test was to capture a video of rotating tracer particles suspension. The experiment is performed without external ambient light sources and the particles are illuminated by a laser sheet generated by passing a laser beam through a cylindrical lens. This experiment was designed to test the illumination system. The type

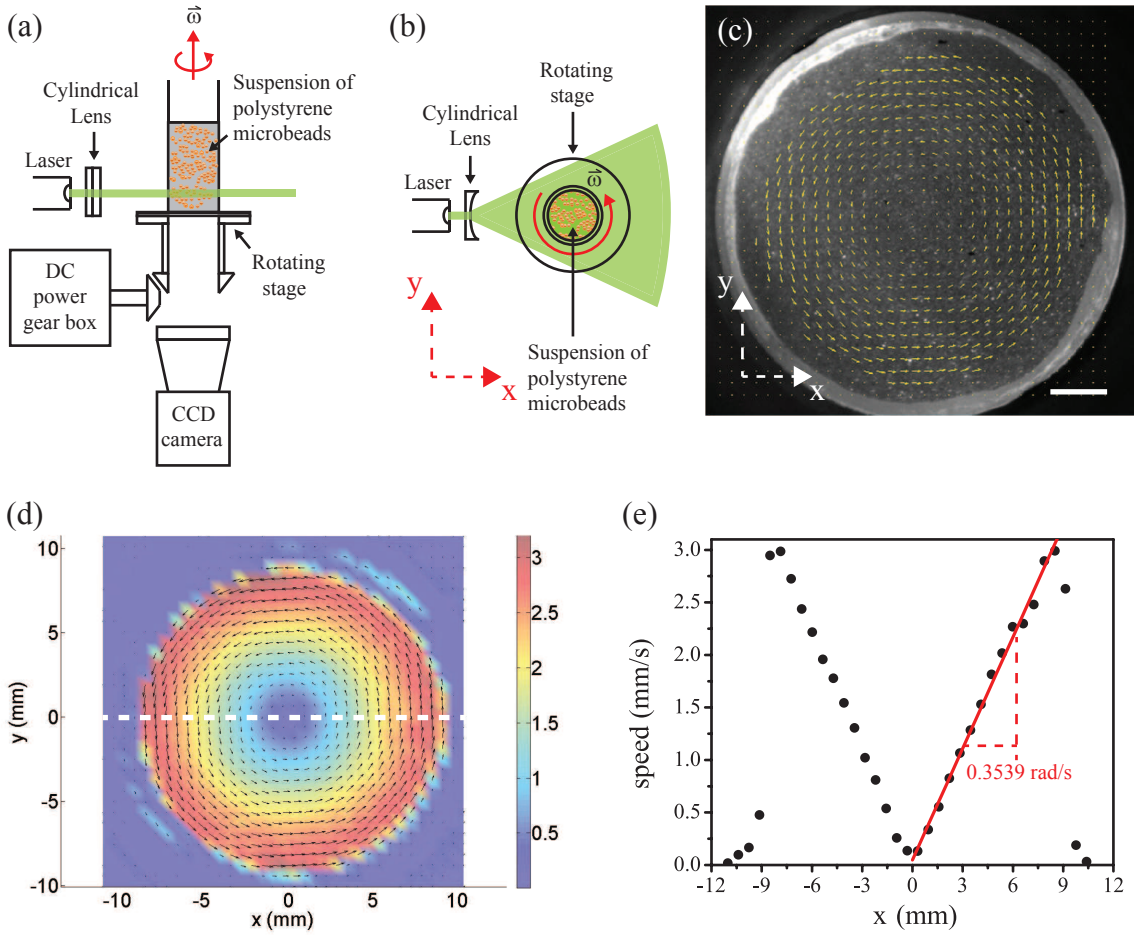

Figure 2.22: (a) Side view and (b) top view schematic of the light and camera testing system. (c) A snapshot of a rotating bath video superimposed by the displacement vector fields generated by the OpenPIV program. (d) Displacement vectors in (c) mapped with colors corresponding to their magnitude. The color bar indicates the speed in mm/s. (e) Plot of the speed across the dotted line drawn in (d). The scale bar in (c) represents 2 mm.

of tracer particles that we use are polystyrene beads of approximately 16.2 μm average diameter and 1.06 g/cm^3 density (obtained from Bangs labs). To prepare a sample of suspension, we added about 0.4 g of particles to a 100 ml of deionized water and placed it on a vortex mixer to stir for about 2-3 minutes. We then placed our sample in an ultrasonic bath for 10 minutes to prevent particles from aggregating. The finished sample texture appeared optically heterogeneous to the naked eye, indicating that the seeding particles well dispersed all over the sample.

Once we had the sample of suspension, we poured it in a cylindrical container attached to the rotating stage. During the rotation, a CCD camera was placed at the bottom to record the video through the opening hole of the rotating stage (see figure 2.22(a) and (b)). The period of rotation

was measured to be constant at approximately 18 s per revolution, which is comparable to the collapsing time of a typical toroidal droplet. During the analysis, we saw that the locations where the vector length was noticeable were mostly within the area that contains tracer particles (see figure 2.22(c)). The corresponding color map of the speed after the conversion of pixel/frame to mm/s in figure 2.22(d) displayed a pattern similar to figure 2.21(e). This is due to the fact that the whole fluid moves as one rigid body, as expected for constant rotation. Then by plotting the speed along the white line in figure 2.22(d), we obtained angular speed ω directly from the magnitude of the slope of speed inside the region containing tracer particles, as shown in figure 2.22(e). Then by converting ω to the period we got the period of approximately 17.75 s which is the expected value for the period.

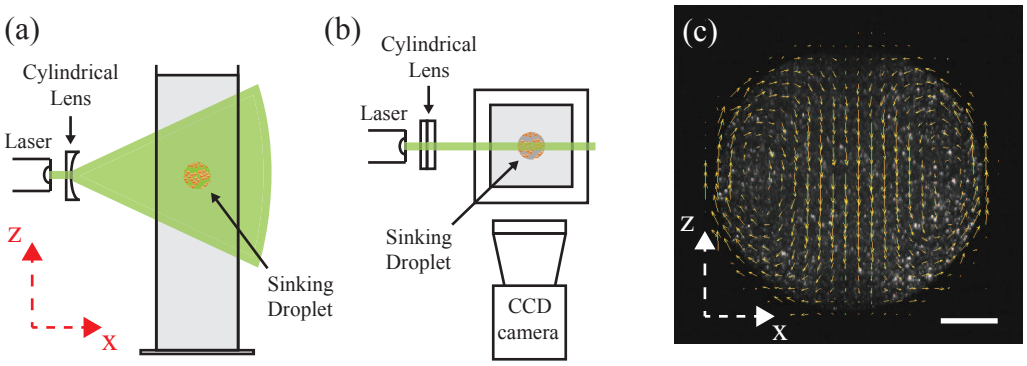

Figure 2.23: (a) Side view and (b) top view schematic of the experimental setup to capture the flow field of a sinking droplet. (c) Snap shot of a sinking water droplet inside 1000 cP silicone oil video superimposed by the displacement vector fields generated by the OpenPIV program after subtracting the sinking velocity. The scale bar in (c) represents 3 mm.

In the previous setup, scattered light from the particles only passed through a flat glass before hitting the camera lens with the tracer particles and surrounding fluid moving together as one solid body. However, scattered light passing through a toroidal surface will inevitably get distorted because of the non-zero curvature that a torus possesses. In addition we also expected that the tracer particles would not move as one solid body due to the variations of flow within the torus. To see how well we can capture a video for PIV analysis under these extra conditions, we chose to perform one final test to measure the velocity field inside a sinking droplet. This experiment was very simple and also had a lot of extensive theoretical [54, 55, 56] and experimental research [57, 58, 59, 60, 61, 62, 63].

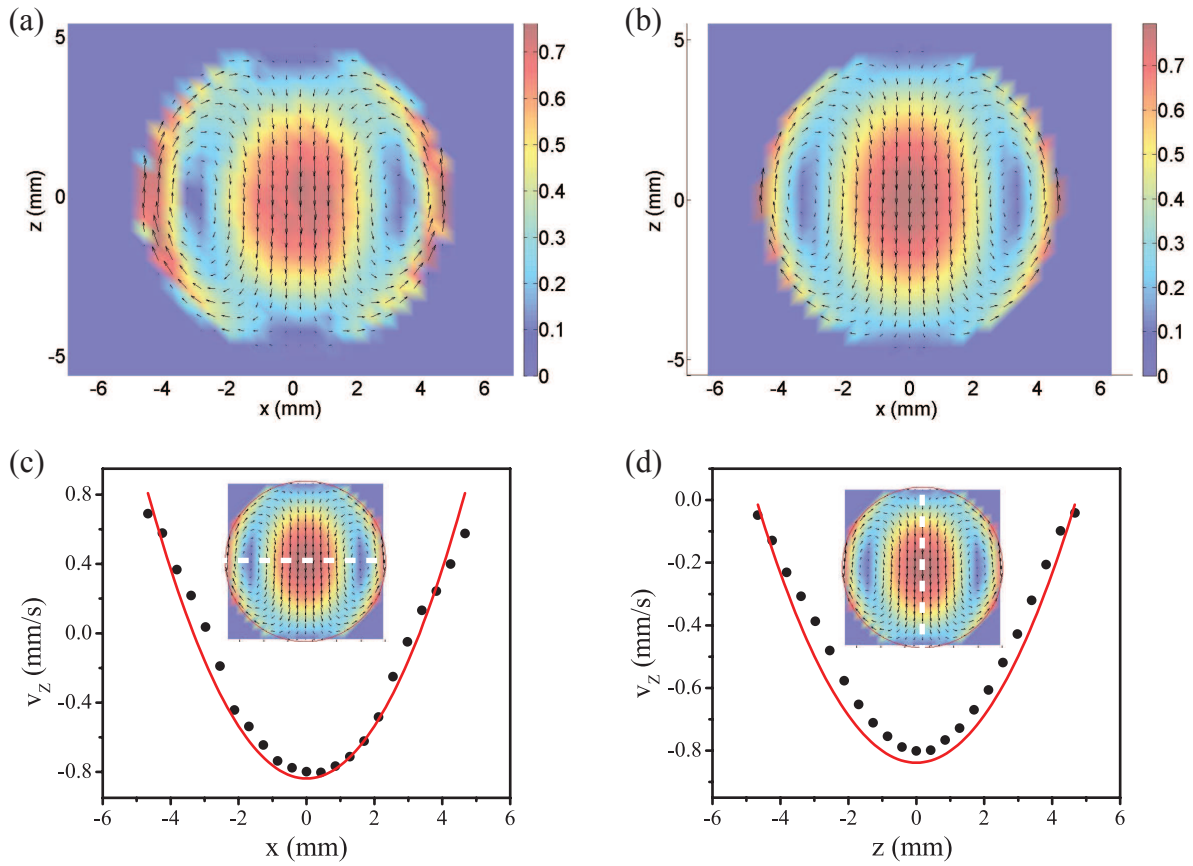

Figure 2.24: (a) Experimental result of a velocity field of a sinking droplet in a co-moving reference frame mapped with colors corresponding to the speed. (b) A corresponding theoretical calculation of a velocity field of a droplet of the same diameter (a = 0.9 mm)sinking at the same speed (U = 0.4 mm/s) under the assumption that $Re \to 0$. (c,d) Comparison of velocity in z-direction across the droplet plotted along dashed line of the corresponding inset between the experimental (•) and theoretical (red line) result.

In this experiment, we let a drop sink a distance of approximately 30 cm inside a rectangular container filled with 1,000 cP silicone oil. In this setup, a laser sheet in the plane parallel to the gravitational direction would illuminate tracer particles inside of a sinking drops (see figure 2.23(a)), with the camera mounted from the side facing a flat side of the container in the direction perpendicular to the plane of the laser sheet (see figure 2.23(b)). In order to let the droplet reach the terminal sinking speed, the video of the droplet was captured after the droplet had fallen about 15 cm. We found that the result was reproducible after performing several tests. An example of an image analysis snapshot after subtracting a sinking speed is shown in figure 2.23(c).

The volume of each sinking drop was kept constant at 0.35 ml and they were observed to have a

perfect spherical shape throughout a whole sinking distance with its radius, a, always measured to be approximately 4.4 mm. The terminal sinking velocity, $U \approx 0.4$ mm/s, as measured directly from the video was the same for every drops. To better see the velocity distribution inside the droplet, we plotted the velocity field after subtracting the sinking speed in figure 2.24(a) with the color mapping indicating the speed in mm/s. To compare this with the theoretical result, we first needed to find out the Reynolds number $Re \equiv \rho U a/\eta$ for our experiment. Then by applying the parameters $\rho \approx 1$ g/cm^3 and $\eta \approx 1000$ cP, we got $Re \sim O(10^{-2})$, indicating that the flow inside our sinking droplet was in a Stoke flow regime. In this flow regime, a well known analytic solution for the stream function inside and outside of a sinking droplet can be written in terms of polar coordinates (r, θ) as [56, 48, 64]:

$$\psi_i = \frac{U r^2 \sin^2\theta}{(1+\kappa)}\left(1 - \frac{r^2}{a^2}\right), \tag{2.21a}$$

$$\psi_o = -2U r^2 \sin^2\theta\left(1 - \frac{a(2+3\kappa)}{2r(1+\kappa)} + \frac{\kappa a^3}{2r^3(1+\kappa)}\right). \tag{2.21b}$$

Then by applying $\vec{v} = \nabla \times \vec{\psi}$ to equation (2.21a), we get the velocity in the r and θ directions inside the droplet as:

$$v_r = 2U\cos\theta\left(1 - \frac{r^2}{a^2}\right), \tag{2.22a}$$

$$v_\theta = -2U\sin\theta\left(1 - \frac{2r^2}{a^2}\right), \tag{2.22b}$$

(assuming $\kappa \to 0$). Using the experimental parameters, we plotted equation (2.22) in figure 2.24(b). In comparison with the experimental result in figure 2.24(a), we bserved good visual comparison. By plotting the experimental result of v_z in the horizontal (along the dashed line in the inset of figure 2.24(c)) and vertical (along the dashed line in the inset of figure 2.24(d)) direction across the droplet together with the theoretical prediction, we found that they were also in good agreement, confirming that our PIV experimental setup could capture good video suitable for the image analysis program.

2.5.2 Velocity Field of Shrinking Torus

For this experiment, a torus was illuminated from the side with a laser sheet, as shown in figure 2.25(a). After each torus was made, we manually adjusted the rotation stage until the flat side of container was facing the camera, then proceeded to capture the image sequences of the collapsing

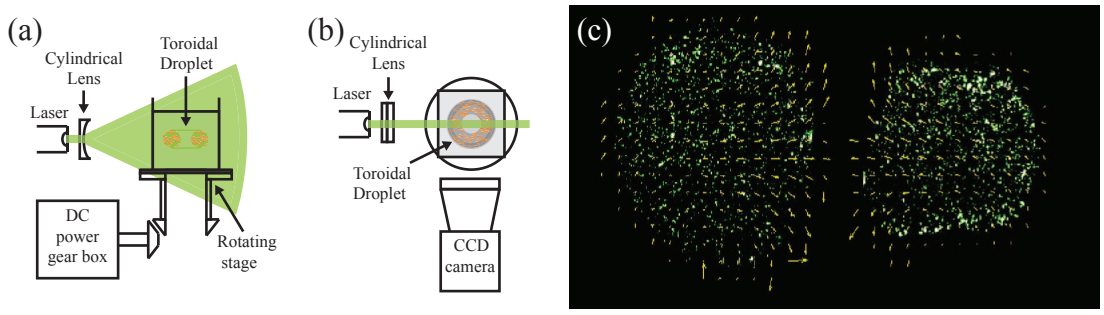

Figure 2.25: (a) Side view and (b) top view schematic of the PIV setup. (c) The snap shot of a collapsing toroidal droplet superimposed with the displacement vector

torus, as shown in figure 2.25(b). The resulting video shows two cross-sections where light sheet passes through. Since the torus is collapsing, the resulting vector field from video analysis program shows that two cross-section are moving toward each other (see figure 2.25(c)). Note also that tori break when $\xi > 2$, so we were only able to capture the velocity fields of shrinking tori with $\xi < 2$.

An example of typical development of the velocity and vorticity fields are shown in figure 2.26, with their corresponding cross-sectional profile shown in the first row. From the visual observation, we noticed that the tube's cross-section begins to resemble a rectangular shape as the torus gets fatter, especially in figure 2.26(d1). Thus from here on we will redefine ξ as $\frac{R_{out}+R_{in}}{R_{out}-R_{in}}$, where R_{out} is the outer radius and R_{in} is the inner radius of a torus (see figure 2.26(a1)); note that for a circular cross-section $\frac{R_{out}+R_{in}}{R_{out}-R_{in}} \rightarrow \frac{R_0}{a_0}$. In the laboratory frame (see figure 2.26(a2)-(d2)), in all aspect ratio, the vector plots of velocity profile all seem to show a general trend such that the magnitude is greater near the interior of the torus ($r = a_0, \alpha = \pi/2$) and then gradually decreases toward the exterior of the torus ($r = a_0, \alpha = 0$). By subtracting the shrinking velocity $\dot{R}(\xi)$ from the overall velocity field, we get the velocity at the co-moving reference frame with the center of the tube's cross-section (see figure 2.26(a3)-(d3)). Here we observed that the source where the velocity is zero indicated that the tube's cross-section was expanding, especially at $\xi \approx 1.6$ and $\xi \approx 1.3$. The location of the source started out near the center of the cross-section at $x = R_0$ (see figure 2.26(a3)) and then grew bigger and moved toward the exterior of the torus ($r = a_0, \alpha = 0$) as the torus got fatter. To show the flow circulations, we mapped the vorticity on to the velocity field after subtracting the shrinking speed (see figure 2.26(a4)-(d4)). Here the sign of the vorticity shows that the circulation is clockwise for the cross section above $z = 0$ and counter clockwise below $z = 0$. From the visual observation the

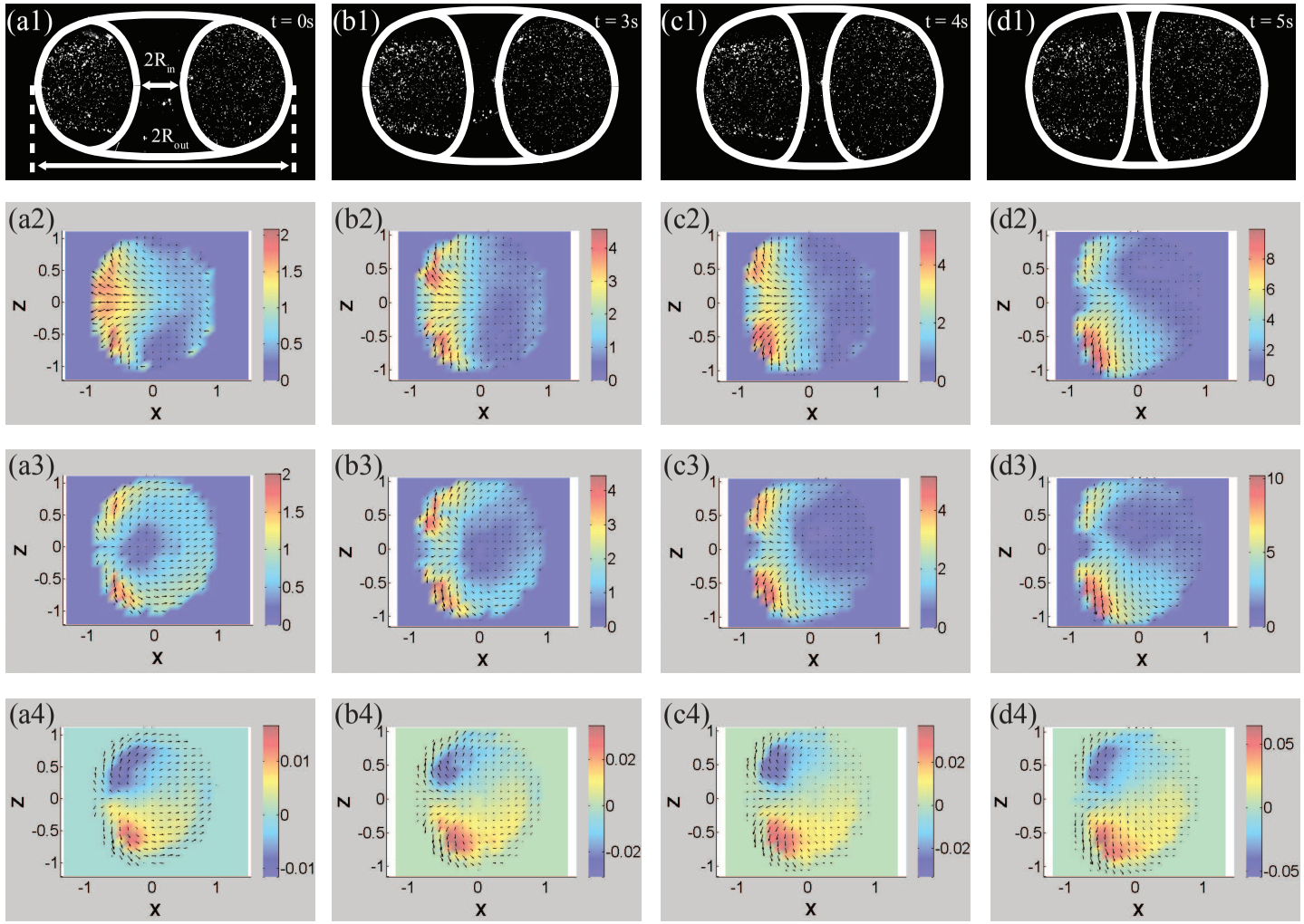

Figure 2.26: (a1)-(d1) The droplet profile at $\xi \approx 1.6$, $\xi \approx 1.3$, $\xi \approx 1.2$ and $\xi \approx 1.1$, respectively. (a2)-(d2) Corresponding velocity field at stationary frame of reference. (a3)-(d3) and (a4)-(d4) are the corresponding velocity fields in the co-moving reference frame of center of the tube mapped with the speed and vorticity, respectively. All of the velocities and vorticities are normalized by the shrinking speed $\dot{R}_0$ and the cross-section is normalized by the tube radius a_0.

maxima of the vorticity are located at the same locations for all aspect ratios.

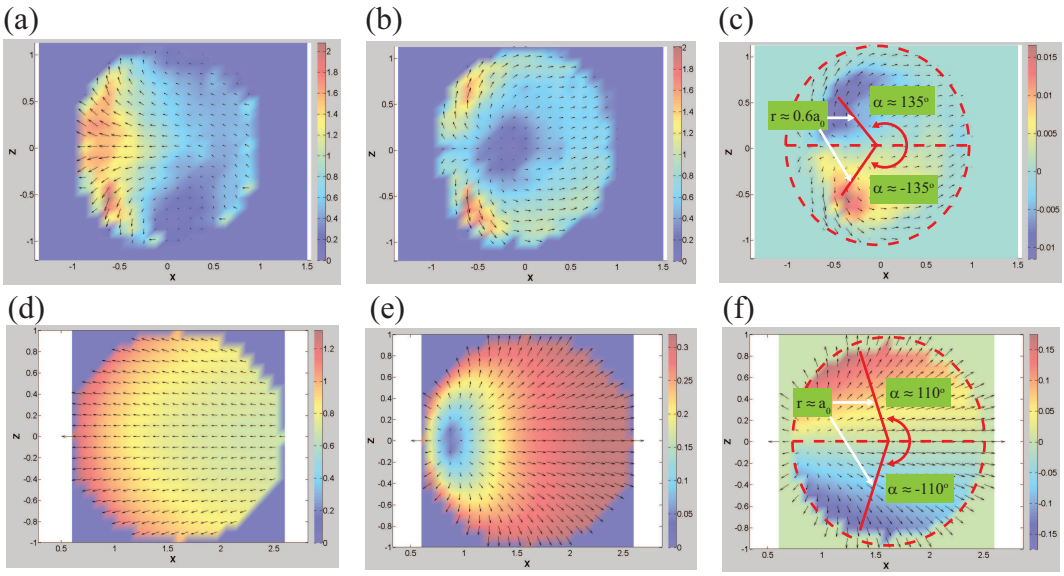

Figure 2.27: Diagram showing the velocity field comparison between the experiment and theoretical result at $\xi \approx 1.6$. (a) Plot of velocity field at stationary frame of reference for experimental result. (b) and (c) are the corresponding velocity fields in the co-moving reference frame of center of the tube mapped with the speed and vorticity, respectively. (d)-(f) are the corresponding theoretical plots for (a)-(c). All of the velocities and vorticities are normalized by the shrinking speed $\dot{R}_0$ and the cross-section is normalized by the tube radius a_0.

To see how accurately the theoretical predictions described our experimental results, we compared our experimental results with the theoretical prediction in [34, 50]. First, we visually compared the results. From the observation, the theoretical prediction seemed to have captured the right velocity distribution in the laboratory frame of reference where the speed showed the decreasing trend from the greatest value at the interior to the exterior of the torus (see figure 2.27(a) and (d)). In the co-moving reference frame at the center of the tube, both experimental and theoretical showed the existence of the source which indicated the growth of the cross-section due to the volume conservation (see figure 2.27(b) and (e)). The maximum vorticity in both the experimental and theoretical results indicated that it is at an angle $\alpha > 90°$ ($< -90°$ for $z < 0$) for tori of all aspect ratios, but are located the different locations (see figure 2.27(c) and (f)). However, the main difference here is the sign of the vorticity indicating flow circulation at the cross section predicted by the theory is opposite from the experimental result. Note also that the locations of the maximum vorticity are always approximately at the same location for the experimental results (see figure 2.26(a4)-(d4))

but for the theoretical results the location for the maximum vorticity is a function of ξ (see figure 2.20(a3)-(d3)).

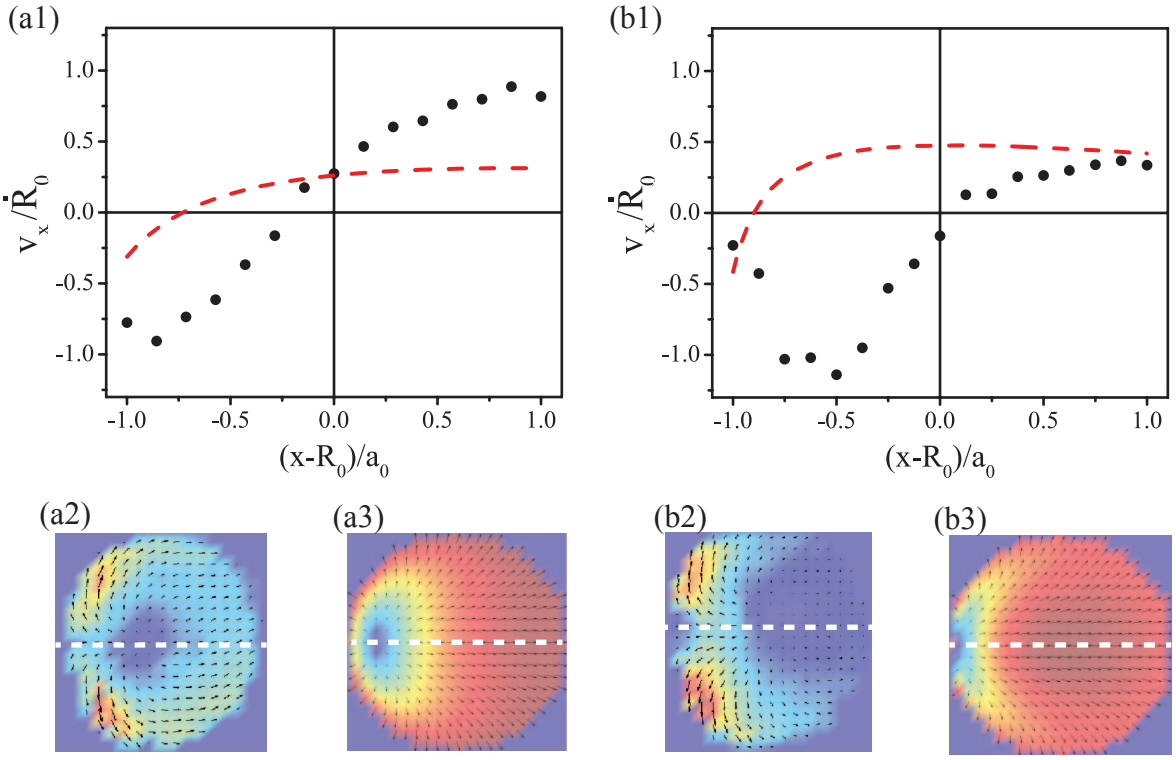

Figure 2.28: (a1) A graph of the x-component of the velocity along the white dashed line for the experimental result shown in (a2) (•) and theoretical calculation shown in (a3) (red dashed line) for $\xi \approx 1.6$. (b1), (b2) and (b3) are the corresponding figures for $\xi \approx 1.2$.

In order to quantitatively compare the experimental and theoretical results, we plotted the x-component of the velocity v_x normalized by the shrinking speed $\dot{R}_0$, along across the tube cross section from the interior ($r = a_0, \alpha = \pi$) to the exterior ($r = a_0, \alpha = 0$) of a torus at a height where fluid flow started to flow in the opposite direction across the tube cross section for $\xi \approx 1.6$ (see figure 2.28(a)) and $\xi \approx 1.2$ (see figure 2.28(b)). Here we extracted the precise location of the source by locating where $v_{xc}/\dot{R}_0 = 0$. For $\xi \approx 1.6$, the experimental results showed that the source is located near $x = R_0$, however the theoretical prediction showed that the source is located closer to $x = R_{in}$, as shown in figure 2.28(a1). This corresponded directly to the blue region within the cross section where the velocity is zero in figure 2.28(a2) and (a3) for experimental and theoretical result, respectively. We also observe that the velocity at the interface are different. At later time when the torus shrinks to $\xi \approx 1.2$, the location of the source predicted by theory moves even closer toward the

interior of the cross section but remaining approximately at the same location for the experimental result, as shown in figure 2.28(b1). The experimental result also show that the velocity of the flow to the right of the source also decreases, which also corresponds to the spread of the blue region in figure 2.28(b2). To the left of the source for the experimental result, we also observe the more prominent feature of the minimum in the velocity and the stagnation of the flow near the interior of the cross section. This indicate the stronger shearing affect resulting from the approaching cross section from the opposite direction.

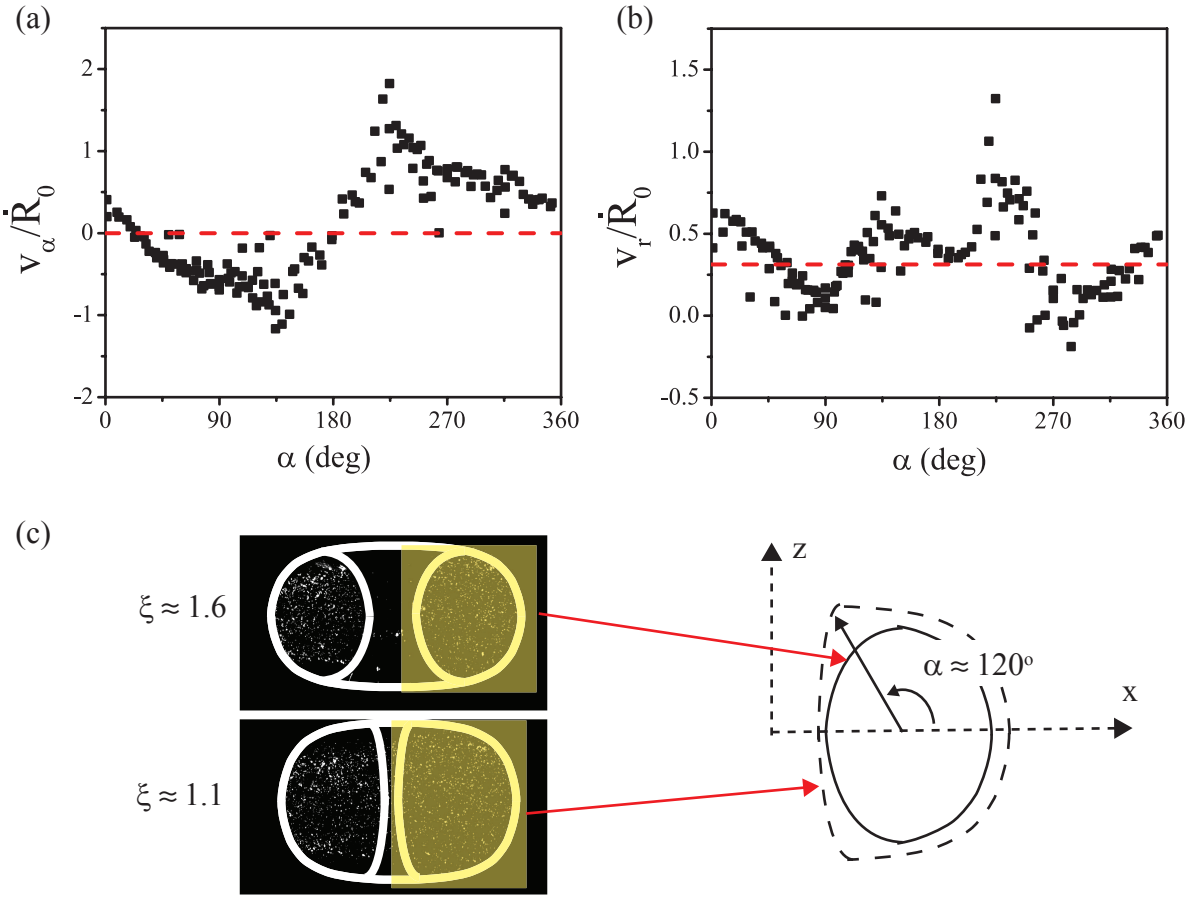

Figure 2.29: (a) and (b) are plot of experimental tangential and radial velocity, respectively, as a function of α at the torus interface for $\xi \approx 1.6$. The red dashed line in both (a) and (b) is the corresponding theoretical assumption. (c) A diagram showing show the cross-sectional shape changes with ξ

Finally, we addressed some possible reasons that the velocity fields predicted in [34, 50] were quantitatively difference from our experimental result. Recall that the two theoretical assumptions on the boundary velocity at the interface are: (i) there is no tangential velocity $v_\alpha = 0$ and (ii) radial

velocity is constant $v_r = \dot{R}_0 \frac{a_0}{2R_0}$. These assumptions did not accurately describe our experiment because in the experimental result $v_\alpha \neq 0$ and v_r is not constant. To show this, we plotted the normalized v_α and v_r at the boundary for $\xi \approx 1.6$ for the experiment and theoretical prediction, as shown in figure 2.29(a) and (b), respectively. For v_α, we found that our experimental data resembled the boundary conditions of the sinking viscous droplet [48] and infinite cylindrical thread [65] in another viscous liquid which assumes $v_\alpha \propto -\sin\alpha$. This indicated that the theory used no-slip boundary condition instead of the proper stress force and as a result the sign of the vorticity is not captured by the theoretical calculation. Note also that the maximum in speed is shifted to $\alpha \approx \pm 135^\circ$ instead of $\alpha = \pm 90^\circ$. This also explain why the maximum in vorticity found in the experiment is located at $\alpha \approx \pm 135^\circ$ because if the cross-section remains circular then the maximum in vorticity should also located at $\alpha = \pm 90^\circ$. In addition, the plot of boundary values of v_r also shows the local maximum at $\alpha \approx \pm 135^\circ$ and $\alpha = 0$. The maximum found at $\alpha \approx \pm 135^\circ$ is a direct consequence of the evolution of the tube's cross-sectional shape. In order for the shape of the tube's cross-section found in $\xi \approx 1.6$ to evolve into the shape found in $\xi \approx 1.1$, the interface at $\alpha \approx \pm 135^\circ$ and $\alpha = 0^\circ$ has to travel more than the rest of the interface (see figure 2.29(c)). Thus, it seems that the deviation of a tube's cross-section from a perfect circular shape played a major role in determining the hydrodynamic of a collapsing torus. In the end the assumption that the tube's cross-section remains circular is not valid for our experiment.

2.6 Conclusions

We were able to successfully generate and control the aspect ratio of a toroidal droplet. Our results provide insight on when a toroidal droplet transforms into a spherical droplet, there is an interesting interplay between the two relevant length scales in the problem. The radius of the contour length, R_0, and the radius of its circular cross-section, a_0. The classical hydrodynamic breakup competes with a shrinkage mechanism in a race to induce the transition to the energetically favored spherical shape. For thin tori, $\xi > 2$, classical hydrodynamic instabilities induce breakup. The measurement of the growth rate of the capillary instability also suggest that tori break up in the same way as a cylindrical jet. However, there is the additional requirement that only the most unstable modes with an integer number of wavelength can induce a breakup of a torus. This condition is often achieved

by shrinking of the torus. For tori, $\xi < 2$, the shrinkage mechanism dominates and in this case the tube of the torus continues to grow until it coalesces onto itself.

By performing PIV analysis on the flow field of collapsing torus and then comparing the result with the only known theoretical prediction by [34, 50], we found that the theory was able to qualitatively capture some features of a shrinking torus. These features include: (i) in the lab frame of reference, the velocity distribution where the speed is greatest at the interior of a torus and gradually decreases as we moved the exterior of a torus along the cross-section and (ii) after subtracting the shrinking speed, the source can be seen which indicates the growth of the tube's cross-section due to the volume conservation. However, when comparing to the theoretical prediction, we found that the quantitative results are quite different. We deduced that this could be due to the following issues: (i) the tangential velocity at the interface boundary was neglected in the theoretical study and (ii) the deviation in the tube's cross-sectional shape from a circle seems to play a major role in shaping the hydrodynamics inside a torus. Thus, we suggested that future theoretical work should incorporate these changes in order to better capture the experimental results.

CHAPTER III

STABILIZING TOROIDAL DROPLETS

3.1 Introduction

Bubbles and droplets are ubiquitous in nature. Surface tension forces them to conform to a spherical geometry to minimize their surface area for a given volume [24]. As a result, droplets or bubbles with nonminimal surface shape, such as a torus, are rarely seen in nature. In spite of this, there are several instances where such droplets can be observed. For example, toroidal droplet can be generated transiently from the impact of a free-falling droplet onto solid surface [66] or by injection of a liquid into a rotating viscous bath [67]. It was also shown there that thin torus breaks into a certain number of equal size drops, while sufficiently fat torus shrinks toward its center to coalesce onto itself. The former is a result of the capillary instability analogous to the Rayleigh-Plateau instability of straight cylindrical jets [47, 43], while the later is because of the unique pressure distribution as a result of the toroidal geometry [50]. Stabilization of toroidal droplets, therefore, requires an opposing force. Stabilizing toroidal geometry would enable us to perform unique experiments to probe ordered materials confined within droplets that are topologically different from a sphere. A striking demonstration of this would be the observed double twist configuration in torus filled with a nematic liquid crystal (see chapter 4). It also has potential to study the disclination patterns of hexagonal order embedded in the toroidal geometry, which so far has only been explored theoretically [35, 36].

In this chapter, we report a novel yet simple way to generate and stabilize toroidal drops using a yield stress material. Our technique enables us to stabilize torus with precise control over their aspect ratio. Through the experimental investigations, we established the relationship between the yield properties of the outer material and the dimension of the torus that can be preserved.

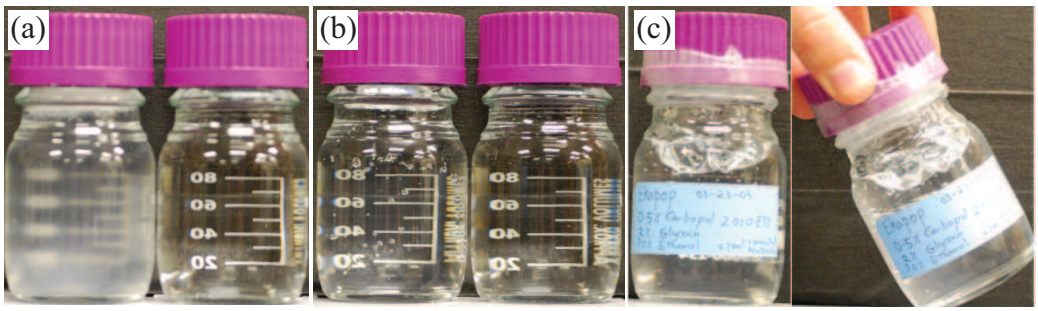

Figure 3.1: Pictures of aqueous Carbopol solution, (a) & (b) comparison of 0.3% Carbopol solution (on the left) and water (on the right): (a) Carbopol solution before neutralization, (b) Carbopol solution after neutralization. (c) 0.5% Carbopol solution after neutralization.

3.2 Preparation and Properties of Carbopol Solution

3.2.1 Preparation Method

We prepared yield stress samples using an ionic microgel called carbopol (Carbopol ETD 2020 provided by Essential Ingredient) as the thickener. It is a white powder with very low wetability. Carbopol can be added to aqueous solutions to give them a yield stress and shear-thinning properties; which make them a key thickener in many cosmetic, and pharmaceutical products. This is because shear-thinning allows sample to easily spread and yield stress allows it to conform to the shape of the skin surface after it has been applied.

To prepare samples, we use 30% wt. ethanol, 2% wt. glycerol, variable concentrations of carbopol (0.1%-1% wt.), and de-ionized water. First, carbopol was dispersed in a de-ionized water, glycerol and ethanol. Then, the mixture was shaken by hand and left at room temperature overnight for the carbopol to fully hydrate and swell. The next day, we re-examine the samples, at this point the carbopol should have completely dissolved and the appearance of the samples was a slightly milky turbid solution as shown in the left in figure 3.1(a) besides a container filled with water. Then the dispersion was neutralized with 18% NaOH until the pH reaches around 7. In the neutralization process, the mixture was stirred using a spatula after each NaOH addition until a clear, transparent gel was formed, as shown in figure 3.1(b); note that the numbers at the back of the bottle are clearly visible. We then sealed the containers and kept the samples at rest again for at least another 24 hours before using it. The neutralized carbopol solutions clearly possess yield stress as some air bubbles will remains trapped inside the solution for as long as the solution is usable. The sample of

carbopol concentrations of 0.5% or above will not even flow under the influence of gravity; notice that the free surface of the sample in figure 3.1(c) remains bumpy irrespective of time and of the bottle orientation with respect to the gravitional-force direction.

3.2.2 Rheology of Carbopol Solution

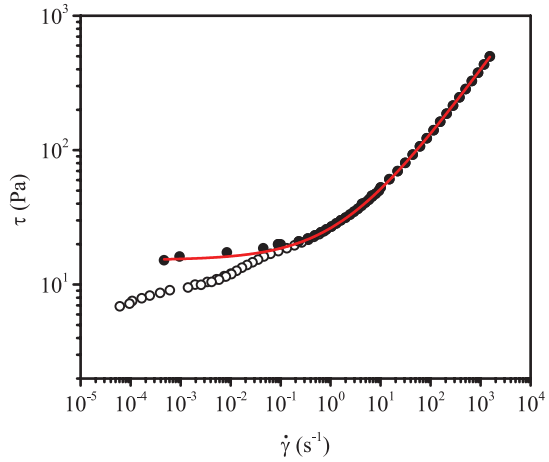

Figure 3.2: Flow properties of 0.4% carbopol solution with slip (open symbol) and without slip (close symbol). The solid line is theoretical fit using Herschel-Bulkley model

Shear experiments were carried out using a stress-controlled rheometer (Anton-Paar Physica MCR-501) equipped with a cone-plate fixture cp25-2s, which has a 25mm-diameter and a 2° cone angle. The tool has a rough sandblasted surface to prevent a slippage between the tool and the sample during the measurement, which were observed when a smooth surface tool is used instead of a sand blasted one. An example of the slip can be clearly observed in the steady-state flow curve plot of the shear stress τ as a function of shear rate $\dot{\gamma}$ will show that a material will flow at a stress lower than an actual yield stress, as shown by the opened circles in figure 3.2. This behavior was observed under microscope in [68]. The temperature was kept at 20°C throughout the measurement process. After we loaded the sample on to the rheometer platform, a ring of water was added around the edge of the platform and the platform was covered with a metal solvent trap to minimize evaporation. Before running any tests, a stress well above the yield stress of the sample was applied for about a minute to break any previous structure that the sample may have processed. This ensures that the sample being measured had the same initial conditions in each test.

First we performed a strain sweep test on the samples. These experiments were all performed

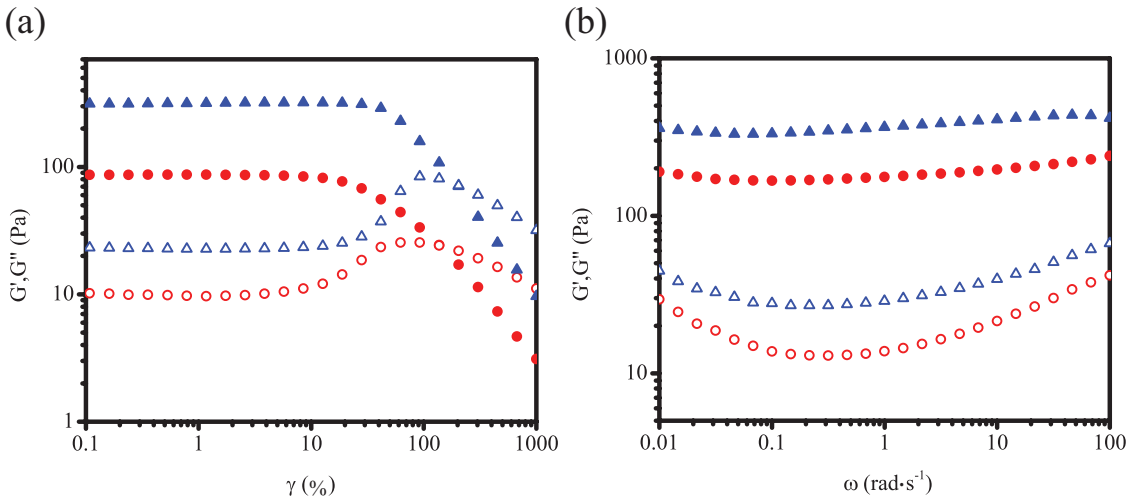

Figure 3.3: Oscillatory responses of storage modulus, G', (closed symbols) and loss modulus, G", (open symbols) for 1% Carbopol solution (▲, △) and 2% Carbopol solution (●, ○): (a) strain sweep at angular frequency of 1 $rad \cdot s^{-1}$; (b) frequency sweep at 1% strain.

at a constant oscillating angular frequency of 1 rad/s. As evident from figure 3.3(a), the storage modulus, G', which represents the elastic portion, is about an order of magnitude greater than the loss modulus, G", which represents the viscous portion, at low strains up to about 10% indicating a glass behavior of the system in a linear elastic regime. Beyond this strain, the storage modulus begins to drop while the loss modulus begins to rise and cross over happens at about 100% strain indicating that a structure breaks down and begins to flow as the sample enters the non-linear regime.

Using small deformation (at 1% strain), where G' and G" do not depend on strain, we performed a 0.01-100 rad/s frequency sweep on the samples. For all of our samples, G' is about an order of magnitude higher than G" indicates that the solutions are largely elastic in these frequency range (see examples in figure 3.3(b)). The minimum in G" also indicating that there is a cross-over between the two moduli at very low ω because of the structural relaxation, where the structure may ultimately flow [70].

Next, we performed a steady-state flow experiment, where we measure the strain shear rate of the sample after applying a constant shear stress. We also performed creep experiments to confirm that, after a small lag time, the measured shear strain is linear with time. The obtained flow curve for each sample is fitted using Herschel-Bulkley model [69]:

$$T_{xy} = \tau_{y,s} + m\dot{\gamma}^{n}\,, \tag{3.1}$$

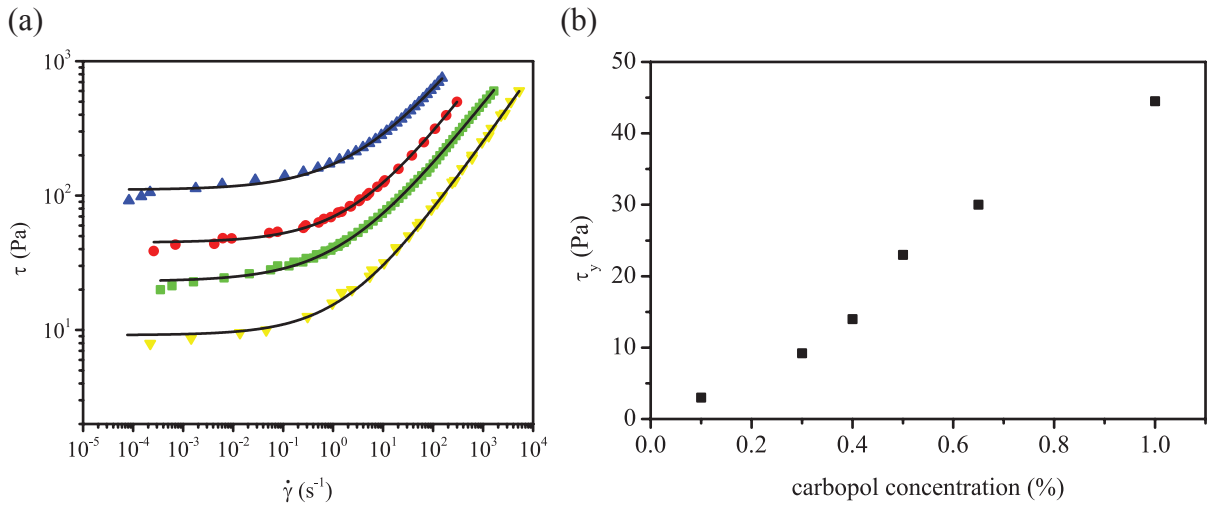

Figure 3.4: (a) Flow properties of 0.3% (▼), 0.5% (■), 1% (●) and 2% (▲) carbopol solution. The solid lines are theoretical fit using Herschel-Bulkley model. (b) The values of yield stress with respect to the carbopol concentration. The concentration of ethanol and glycerol are kept constant at 30% and 2%, respectively.

Table 3.1: Fitted parameters from flow curve experiments

.

Carbopol(%)	τ_y (Pa)	m	n
0.3	9.2	6.3	0.53
0.4	15	11	0.51
0.5	23	17	0.48
1.0	45	25	0.51
2.0	110	61	0.47

as shown in figure 3.4(a), where T_{xy} is the shear stress, $\tau_{y,s}$ is the shear yield stress, m is the consistency index, $\dot{\gamma}$ is the shear rate, and n is the shear exponent. The fit parameters: τ_y, m and n corresponding to all of our sample concentrations are shown in table 3.1. The value of τ_y increases with the carbopol concentration, as shown in figure 3.4(b). This allows us to freely control the yield stress of the sample by varying only the carbopol concentration. If $\tau_y = 0$ the equation (3.1) reduces to the power law model $T_{xy} = k\dot{\gamma}$ [71], where $k = m\dot{\gamma}^{n-1}$ is the effective viscosity ($n = 1$ and k becomes viscosity for a Newtonian fluid). Our fitted results yields $n \approx 0.5$ indicating that k is a decreasing function of $\dot{\gamma}$, which imply that our samples are shear thinning; note that when $n > 1$, the opposite happens and the material becomes shear thickening.

3.2.3 Surface Tension Measurement for Carbopol Solution

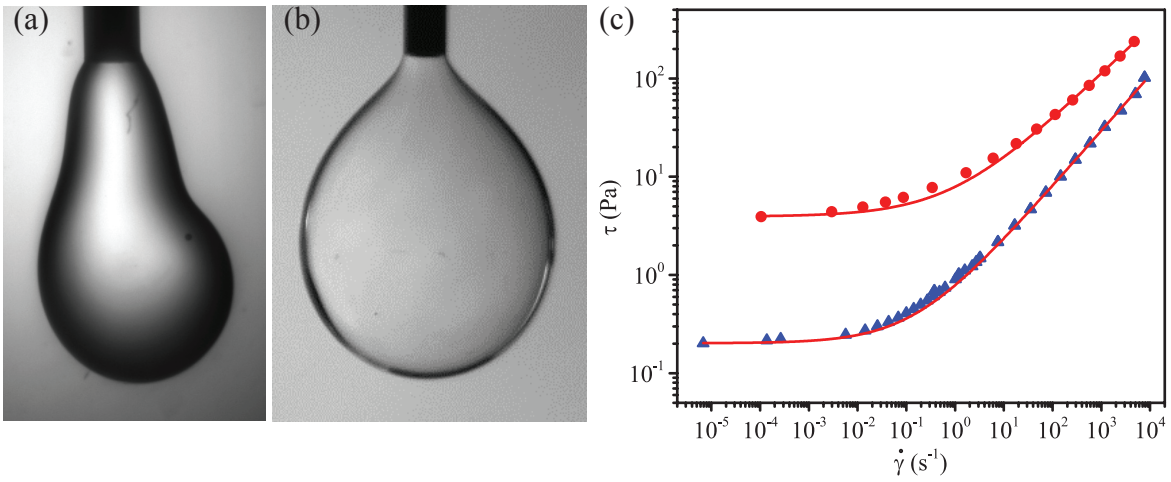

Figure 3.5: (a) 0.1% and (c) 0.075% Carbopol solution extruded from a metallic needle inside 10 cst silicone oil. (c) Flow property of 0.1% (●) and 0.075% (▲) carbopol solution. The solid line is the theoretical fit using Herschel-Bulkley model.

We used the pendant drop method (see Appendix A) to get the value of the interfacial surface tension, Γ, between 0.075% carbopol solution and 10 cst silicone oil from which we obtained $\Gamma \approx 6.6$ mM/m, which could resulted from the high concentration of ethanol (30%). The reason we used a sample with low concentration of carbopol to measure its interfacial surface tension is because a pendant drop generated with 0.1% carbopol solution is distorted, as shown in figure 3.5(a). However, a pendant drop generated using 0.075% carbopol shows a good symmetric shape, as shown in figure 3.5(b). Thus, we hypothesize that a pendant drop with measurable profile can only be obtained using solution with $\tau_y < \Gamma/2a$, here a is considered as a droplet diameter. Then using $\Gamma \approx 6.6$ mN/m and $a \approx 5$ mm, which is typical when using a needle with 1 mm to generate a pendant drop, we get $\Gamma/2a \approx 0.7$ Pa, which is less than 4 Pa for τ_y of 0.1% carbopol (see figure 3.5(c)). Thus we chose the 0.075% carbopol solution with $\tau_y \approx 0.2$ Pa, as shown in figure 3.5(a). We also anticipated that γ is determined mainly by solvent composition, as demonstrated in [72], where the solutions of carbopol with yield stress between 3-80 Pa have almost the same value of surface tension value. Therefore we can assume that the interfacial tension for the samples should be similar if not the same.

3.3 Generation and Stabilization of Toroidal Droplets Inside Yield Stress Media

3.3.1 Experimental Method

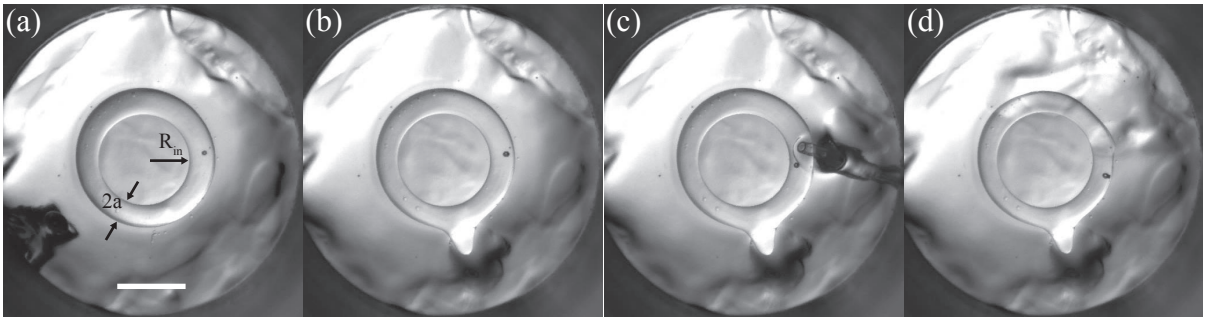

Figure 3.6: Stable toroidal droplet made out of silicone oil inside 0.5% Carbopol solution. The scale bar is 5 mm. (a) Toroidal droplet right after formation. (b) The deformation remains on the droplet after the perturbation. (c) Deformed toroidal droplet getting poked around by the plastic pipette tip. (d) Toroidal droplet remains stable after some heavy perturbations.

A toroidal drop was made by injecting 10 cst PDMS oil through a metallic needle into a rotating bath containing a continuous phase of carbopol solution. As a result of the combination of the rotation and the viscous drag exerted by the outer phase, the inner liquid forms a circular jet and a toroidal drop is formed once the jet makes one revolution. The thickness of the torus can then be controlled by varying the amount of the infused fluid. After the torus was formed and the needle tip removed, we monitored its behavior over time using CCD camera. For each yield stress we generated tori of various tube radius a (note that a is the smallest tube radius measured after the formation of toroidal droplets inside a yield stress material) and inner radius R_{in} (see figure 3.6(a)). If the shape of a torus remains unchanged up-to about 5 minutes after the formation, we assumed that it is stable. In unstable cases, the breaking or collapsing of the torus generally happens soon after the torus is formed (usually in less than a minute after formation). An example of a stable toroidal droplet made in 0.5% carbopol solution is shown in figure 3.6. First, notice that the deformation remains at the bottome of the torus shown in figure 3.6(b) due to us removing some of the external yield stress material near it. This deformation and the toroidal shape both remain during and after we were poking the sample around with a plastic pipette tip, as shown in figure 3.6(c) and (d).

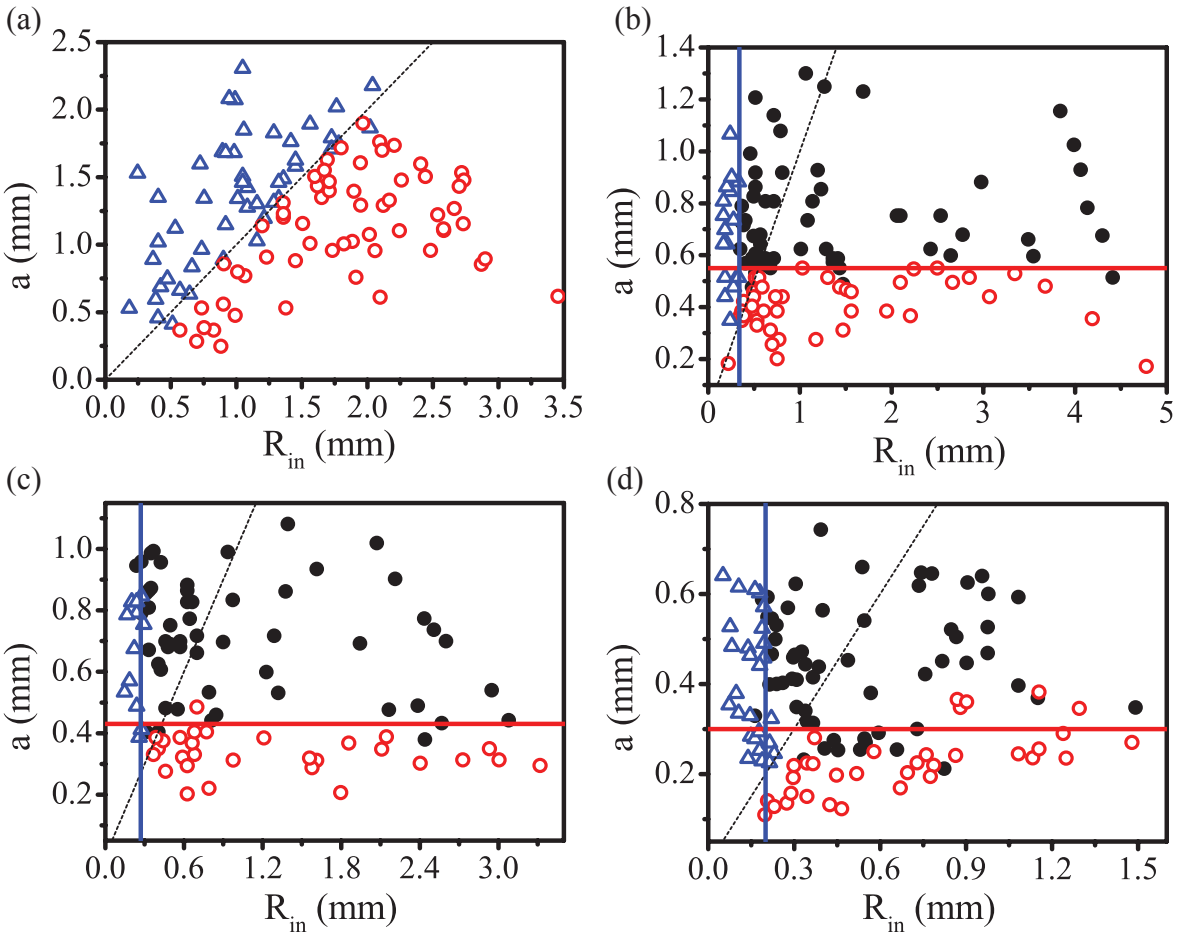

Figure 3.7: Phase diagram of the stability of toroidal droplets. The dashed line corresponds to $a = R_{in}$, which separates the breaking (○) and collapsing region (△). The solid red line corresponds to the value of a_c separating the stable region (●) from the breaking region, while the solid blue line corresponds to the value of R_c separating the stable region from the collapsing region. (a) represents a phase diagram for 60 mM SDS water solution inside 30,000 cst Silicone oil. (b)-(d) represent phase diagrams for 0.3%, 0.35% and 0.4% Carbopol solution respectively.

3.3.2 Results

Toroidal droplet inside of a simple liquid is unstable because without any opposing force, surface tension will drive them into single or multiple spherical droplets. There are two types of transformations, depending on the aspect ratio of the torus. When the inner radius, $R_{in} < a$, a classical hydrodynamic instability induces breakup of the tube. However, when $a > R_{in}$, no unstable modes can grow, and a completely different route of transformation emerges; a continues to grow, while R_{in} continues to shrink (due to volume conservation) until the inner part coalesces onto itself, to finally form a single spherical droplet. Hence the line separating two regions in figure 3.7(a) represents

$a = R_{in}$. This is in reminiscent of Rayleigh-Plateau criterion for a cylindrical jet, where the jet of radius a is unstable if its length, L, is longer than its own circumference, $2\pi a$ and in the torus case $L = 2\pi R_{in}$.

This condition is also true when the outer simple liquid phase is replaced by a yield stress material (see the dashed line in figure 3.7(b)-(d)). However, in this case new thresholds appear. For thin tori, the horizontal line in figure 3.7(b)-(d) indicates a constant critical tube radius of value a_c where the toroidal droplet is stable against breaking if its a is above this value, otherwise it will break. Similarly, for fat tori, the vertical line in Fig. 3.7(b)-(d) represents the critical value of inner radius, R_c, where a toroidal droplet is stable against collapsing provided that $R_{in} > R_c$.

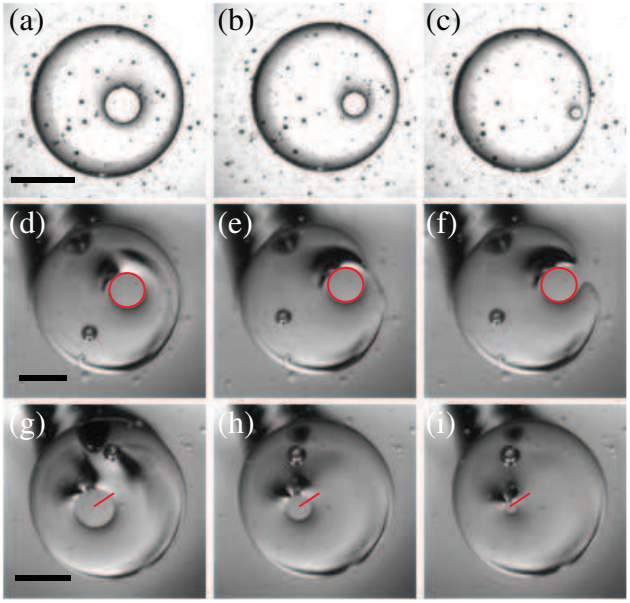

Figure 3.8: Evolution of toroidal droplets: (a)-(c) A toroidal droplet of water with 60 *mM* SDS inside 30000 cst silicone oil simultaneously undergoing both breaking and collapsing process. Silicone oil toroidal droplet inside 0.1% Carbopol solution undergoing: (d)-(f) breaking process and (g)-(i) collapsing process. Each scale bar represents 5 mm.

There are also subtle differences between unstable toroidal droplets made in simple liquid and yield stress material in the way that they transform into spherical droplets. In the previous chapter, we have shown that the shrinkage of toroidal droplet in a viscous liquid is inevitable for all aspect ratios, even when the torus is bound to break. This behavior gets more dominant for a fat torus and completely dominates when $R_{in} < a$. The interplay between the breaking and shrinking are clearly noticeable when a is slightly different from R_{in}, as shown in figure 3.8(a-c). Note that the inner

circle is gradually decreasing in size while moving towards the outside of the torus, indicating that the breaking and collapsing process are happening simultaneously. This behavior is not observed for breaking or collapsing toroidal droplet inside a yield stress material. Here, when the torus is breaking, the inner circle stays constant while the tube is pinching, as shown in figure 3.8(d-f). In the collapsing case, the inner circle simply contracts while its center remains at the same location, as shown in figure 3.8(g-i). These observations illustrate the uncoupling between breaking and collapsing process for an unstable torus inside of a yield stress material.

3.3.3 Stability Analysis

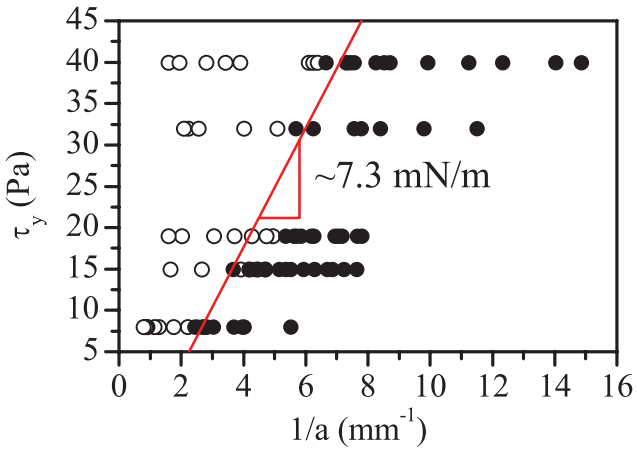

Figure 3.9: State diagram for the stability of thin toroidal silicone oil droplets made inside Carbopol solutions. The yield stress of the Carbopol is tuned directly through the variation of Carbopol concentration. The value of tube radius, a, is a measurement of where the tube radius is the smallest. The line separates regions where the toroidal droplets are stable (○) and where the droplets break (●). The slope of this line is the value of the surface tension between the Carbopol solution and the silicone oil.

For breaking tori, we observe a shift in a_c for different value of $\tau_{y,s}$. To better understand the relation between a_c and $\tau_{y,s}$, we made thin tori and varied a while keeping R_{in} fixed for various $\tau_{y,s}$. By plotting $\tau_{y,s}$ in terms of $1/a$ and separating the region where tori are stable from the region where they break, we observed that the value of a_c decreases with the increasing value of $\tau_{y,s}$, as shown in figure 3.9. The line in this plot which separates the two regions has a slope of approximately 7.3 mM/m. To account for this value, we balance the two relevant parameters: surface tension driven stress, which is trying to break the torus, and $\tau_{y,s}$, which opposes the breaking. We estimate the

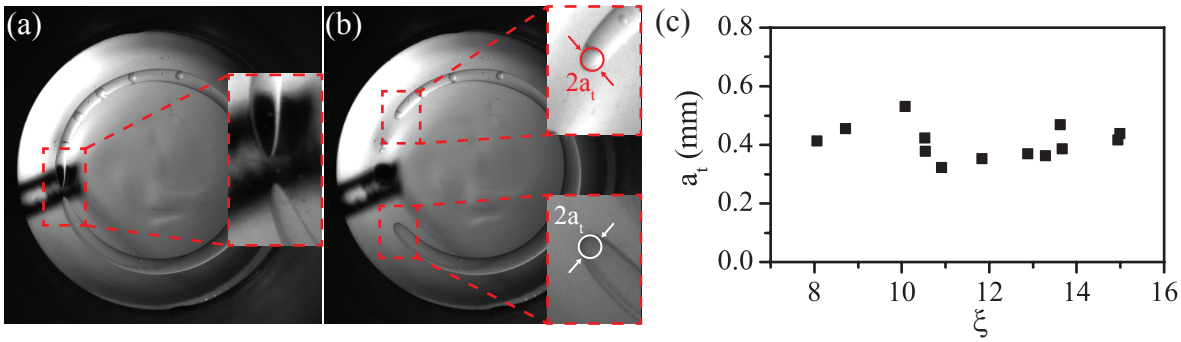

Figure 3.10: (a) Snapshot of a toroidal droplet generated inside 0.35% carbopol concentration ($\tau \approx 12$) right after it broke. (b) Snapshot of a crescent moon shape droplet. (c) The plot of the radius at the tip, a_t, as a function of the initial aspect ratio, $\xi = (R_{in} + a)/a$.

surface tension driven stress to be Γ/a. Hence, the line in figure 3.9 represents:

$$\tau_{y,s} = \Gamma/a_c \,. \tag{3.2}$$

Hence, the slope is $\Gamma \approx 7.3$ mM/m, which is in reasonable agreement with the value 6.6 mM/m obtained from the pendant drop experiment.

From our observations of a broken torus, thin toroidal droplets that pinch inside a yield stress material do not evolve into a sphere. Instead, they always retract into a crescent shape. In a separate experiment, carried out by Hung Le, tori that break were generated in 0.35% carbopol solution and left overnight to allow them to fully retract after they broke. The snapshots of each broken torus are captured right before and after it broke up until it is fully retracted. Right after the breakup, the locations where the torus pinched have very pointy tips, as shown in figure 3.10(a). Once the droplet is fully retracted, the radius of the tips became more round and by fitting a circle on each one, we obtained the final tip radius, a_t, as shown in figure 3.10(b). The data in Fig. 3.10(c) shows that a_t is independent of the original aspect ratio, ξ, and has an average value of 0.45 ± 0.06 mm. Remarkably, this value is consistent with the value of $a_c \approx 4.3$ mm for the tori generated in the same carbopol concentration (see figure 3.7(c)) confirming our hypothesis in equation (3.2).

For all carbopol concentrations, R_c is always less than a_c. In order to quantify their relation, we plot a_c as a function of R_c, as shown in figure 3.11. From the slope of this plot we get

$$a_c \approx 1.85 R_c \,. \tag{3.3}$$

To account for this difference, we need to consider the difference in the deformations of the outer

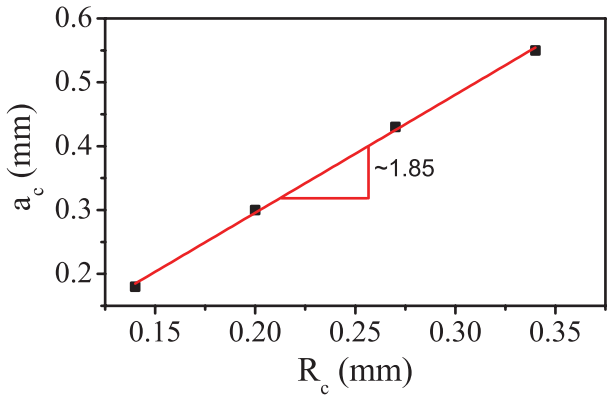

Figure 3.11: Plot of a_c versus the corresponding R_{inc} for different yield stress. The line represents the fit through the data points.

material between the breaking and collapsing process. For instance, during the collapsing process, the outer material in the inner ring of a torus experiences a cylindrical stretching, as shown in figure 3.12(a). In this case, it is the elongation of the outer medium which is the relevant deformation as opposed to shear, and thus the torus will collapses if the normal stress due to surface tension, $T_{yy} - T_{xx} = \Gamma/R$, is greater than the elongational yield stress, $\tau_{y,e}$. However, during the breaking process, the outer material at the interface surrounding the area where the tube pinches must move much more tangentially than in the collapsing case to fill in the space where the inner liquid used to be, as shown in figure 3.12(b). In this case, the way a yield stress material deforms is more of a pure shear than that of an elongation. Thus the torus will break if the shear stress, T_{xy}, is greater than the shearing yield stress, $\tau_{y,s}$, which is consistent with the relation found in equation (3.2). Thus, we can replace a_c and R_c in equation (3.3) with $\Gamma/\tau_{y,s}$ and $\Gamma/\tau_{y,e}$, respectively, and obtain $\tau_{y,e} \approx 1.85\tau_{ys}$. To explain the value of the pre-factor, we consider the Herschel-Bulkley model in a tensorial form [73, 82, 75]:

$$\mathbf{T} = \left[\frac{\tau_{y,s}}{|II_{2D}|^{1/2}} + k|II_{2D}|^{(n-1)/2}\right] 2\mathbf{D}\,, \tag{3.4}$$

where $\mathbf{T}$ and $2\mathbf{D}$ are the extra stress and strain rate tensor, respectively, and $II_{2D} = 1/2[(tr2\mathbf{D})^2 - tr(2\mathbf{D})^2]$ is the second invariant of the strain rate tensor. For steady shear

$$2\mathbf{D} = \begin{bmatrix} 0 & \dot{\gamma} & 0 \\ \dot{\gamma} & 0 & 0 \\ 0 & 0 & 0 \end{bmatrix} \tag{3.5}$$

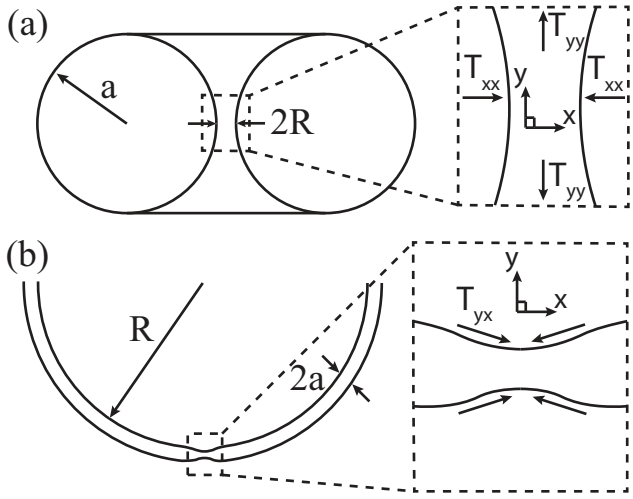

Figure 3.12: (a) Schematic of the side view of a collapsing silicone oil torus inside a viscoelastic solution with a box indicating the region where the viscoelastic filament pinches when the toroidal droplet collapses. (b) Schematic of the top view of a breaking silicone oil torus inside a viscoelastic solution with a box indicating the region where the tube of the toroidal droplet breaks. The bigger boxes are the magnification of the (a) collapsing and (b) breaking region where the stresses responsible for the corresponding transformation to take place are shown.

and for steady uniaxial extension

$$2\mathbf{D} = \begin{bmatrix} 2\dot{\epsilon} & 0 & 0 \\ 0 & -\dot{\epsilon} & 0 \\ 0 & 0 & -\dot{\epsilon}, \end{bmatrix} \tag{3.6}$$

where $\dot{\epsilon}$ is extension rate. Thus, for steady shear, $II_{2D} = -\dot{\gamma}^2$ and equation (3.4) reduces to equation (3.1) and in uniaxial elongational flow, $II_{2D} = -3\dot{\epsilon}^2$, and equation (3.4) reduces to

$$T_{xx} - T_{yy} = \sqrt{3}\tau_{y,s} + 3^{(n+1)/2} k\dot{\epsilon}^n \,. \tag{3.7}$$

From equation (3.7), we see that there is a linear relationship between elongational and shear stress given by:

$$\tau_{y,e} = \sqrt{3}\tau_{y,s} \approx 1.73\tau_{y,s} \,, \tag{3.8}$$

which is in reasonable agreement with our result.

We note that the relationship established in equation (3.8) is found to be consistent with other reports wherein experiments were performed to study the detatchment of carbopol extruding through a circular orifice [75, 83]. However, it was also found that this relation does not apply to other yield

stress materials such as mayonnaise, bentonite or ketchup in the same experiment [75]. Another study on capillary breakup of yield-stress material found the relation to be $\tau_{y,e} \approx 3\tau_{y,s}$ for water-in-oil emulsions [77]. A more comprehensive study of the Laplace pressure in filaments using various type of yield stress fluids has led to the conclusion that equation (3.8) is valid only when the filament life time is approximately equal to fluid relaxation time [78]. In fact, to account for the difference in expected yield stress ratio found using equation (3.8), a more generalized Herschel-Bulkley model has been proposed [77]:

$$\mathbf{T} = \left[\frac{\tau_{y,s}}{|II_{2D}|^{\frac{1}{2}} + m_1 |\frac{III_{2D}}{2}|^{\frac{1}{3}}} + k\left(|II_{2D}|^{\frac{1}{2}} + m_2 |\frac{III_{2D}}{2}|^{\frac{1}{3}} \right)^{n-1} \right] 2\mathbf{D}\,, \tag{3.9}$$

which includes extra material parameters m_1 and m_2, and the contribution from the third invariant $III_{2D} = det|\mathbf{2D}|$. This results in the following nontrivial relationship between elongational and shear yield stress

$$\tau_{y,e} = \frac{\tau_{y,s}}{\sqrt{3} + m_1}\,. \tag{3.10}$$

If the contribution of III_{2D} is neglected (i.e., $m_1 = m_2 = 0$), then equations (3.9) and (3.10) reduces to equations (3.4) and (3.8). The results obtained in our experiment suggested that $m_1 \to 0$.

3.4 Summary

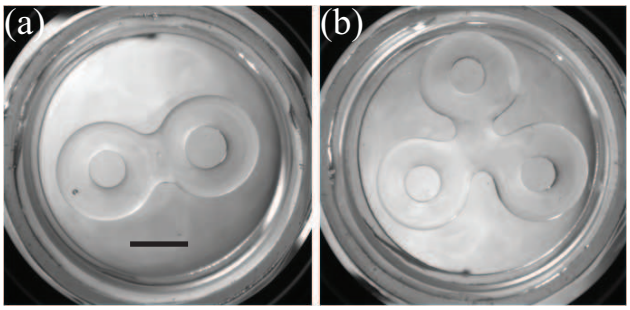

Figure 3.13: (a) Droplet with two handles. (b) Droplet with three handles. Scale bar represents 1 cm.

We demonstrated that it is possible to generate and stabilize a toroidal droplet inside a yield stress material. By controlling the yield stress of the medium surrounding the torus we can control the size of a torus that we can stabilized. We found that the torus is stable against breaking if its tube radius, a, is larger than the critical tube radius, $a_c = \Gamma/\tau_{y,s}$ and stable against collapsing if its

inner radius, R_{in}, is larger than the critical inner radius, $R_c = \Gamma/\tau_{y,e}$. From our investigations, an unstable toroidal droplet in yield stress material also follows similar instability criterion as those generated inside of a viscous medium. That is, it will breaks if $a < R_{in}$ and collapses if $a > R_{in}$. However, unlike a torus inside of a viscous medium, the breaking and collapsing of a torus inside of a yield stress medium happens separately. This happens because the medium surrounding torus is subjected to different kind of flow depending on the type of the instability. The surrounding medium around the breaking tube experiences more shear when the torus is breaking, while the filament at the center of the torus experiences more stretch if the torus is collapsing. Hence, the two processes are decoupled from one another resulting in a constant value of a_c and R_c for a given concentration of carbopol. In addition, $a_c \approx 1.85R_c$ due to the relationship between the elongational and shear yield stress of carbopol solution is expected to follow $\tau_{y,e} = \sqrt{3}\tau_{y,s}$. Thus, the relationship between a_c and R_c may be different if we use different yield stress material that does not follows this relationship. Understanding the stable conditions may also help us generate other exotic shapes, as it is possible to generates droplet with more than one handle inside a yield stress material, as shown in figure 3.13.

CHAPTER IV

NEMATIC LIQUID CRYSTAL DROPLETS OF MULTIPLE GENUS

4.1 Introduction

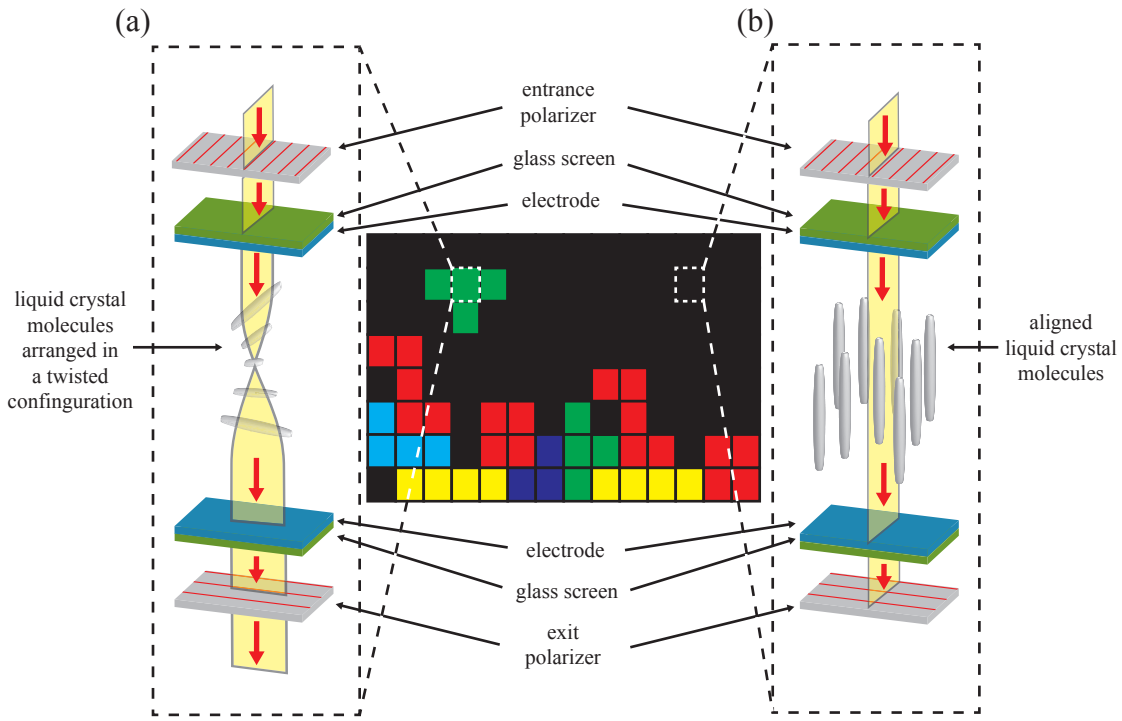

Figure 4.1: Schematic showing light passing through the spacing containing liquid crystal molecules pixelated in each pixel on an LCD screen. (a) The light passes through a twisted liquid crystals molecules. (b) The light passes through liquid crystal molecules arranged in a straight line.

By manipulating the orientation of liquid crystal molecules in the pixels of the LCD display using electric fields, an image can be generated (see figure 4.1). When the electrode is off, the liquid crystal molecules are arranged to twist 90° and the light passes through them following the twist, which as a result passes through the exit polarizer, as shown in figure 4.1(a). If the electrode is turned on, then the molecules rearrange themselves along the direction of the electric field and as a result the light will not be de-polarized and will be blocked by the the exit polarizer, as shown in figure 4.1(b). More exotic structures can emerge when the liquid crystal is confined by curved rather

than flat surfaces. The topology and geometry of the bounding surface can drive the system into structures that would not be achieved without the presence of external fields. In this sense, the shape of the surface can be thought of as playing a role akin to an external field. Thus under confinement by curved surfaces, the molecules can self-assemble into complex hierarchical structures with emergent macroscopic properties not observed for flat liquid crystal cells. However, the design principles and properties of structures generated by this geometric route are still largely unknown.

The lowest energy state of an ordered material, such as a liquid crystal or a simple crystal, is typically defect-free since any disruption of the order raises the elastic energy. However, the situation can be very different if the material is encapsulated within a confining volume and there is strong alignment of the molecules at the bounding surface. In this case, the preferred local order might be lost in certain spatial regions. Such a material will then be geometrically frustrated and will possess a ground state containing topological defects, which are spatial regions where the characteristic order of the material is lost.

For nematic liquid crystals, the molecules tend to align along a common director, **n**. The presence of defects at the boundaries, which we characterize with their topological charge, s, giving the amount of **n**-rotation at the boundary as we encircle the defect, raises the energy of the system. Thus the formation of defects is normally disfavored due to this increase in energy. However, when a liquid crystal is confined in a closed volume with tangential anchoring of the molecules at the boundary surface, the Poincaré-Hopf theorem establishes that the total topological charge on the bounding surface must be equal to its Euler characteristic, χ, a topological invariant given by $\chi = 2(1 - g)$, where g is the genus of the surface or its number of handles [9]. This theorem implies that the ground state of the system will, in many cases, incorporate topological defects. This is indeed the case when the closed surface is spherical [10, 84, 4], since $\chi = 2$ for the sphere. Surfaces that are obtained by twisting, bending, stretching or generally deforming the sphere without breaking it are topologically equivalent to the sphere because none of these transformations introduce handles. Thus a nematic confined by these kind of surfaces would also contain defects in its ground state. In contrast, since a toroidal surface is topologically different from a sphere, as it has a handle and consequently $\chi = 0$, a nematic confined inside its volume may or may not have defects in the order. If it does, however, the added charge of these defects must equal to zero.

Spherical nematics have been thoroughly studied from experimental, theoretical and numerical points of view [13, 14, 15, 11, 16, 12, 17, 18, 19, 20] and their intriguing technological potential for divalent nano-particle assembly has been already demonstrated [21]. In contrast, there are virtually no controlled experiments with ordered media in confined volumes with handles. A notable exception is the optically induced formation of cholesteric toroidal droplets [22]. This largely reflects the difficulties in generating stable handle objects with imposed order. While the sphere is relatively easy to achieve in liquids due to surface tension, the generation of stable droplets with handles remains a formidable challenge.

In this chapter, we experimentally generate stable handled droplets of a nematic liquid crystal using a continuous host with a yield stress. This approach allows us to perform the first experiments that probe nematic materials confined within droplets that are topologically different from the sphere. We observe that the toroidal nematic droplets formed are defect-free. However they exhibit an intriguing twisted structure irrespective of the aspect ratio of the torus. The stability of this configuration, which is in contrast with existent theoretical expectations [23], results from the often-neglected saddle-splay contribution to the elastic free energy. Upon switching from one to multiple-handled droplets, we observe both in experiments and simulations the presence of two defects, each with topological surface charge -1, per additional handle. These defects are nucleated in regions with local saddle geometry to minimize the nematic distortions and hence the corresponding elastic free energy.

4.2 Generation of Nematic Toroidal Droplets and Anchoring Control

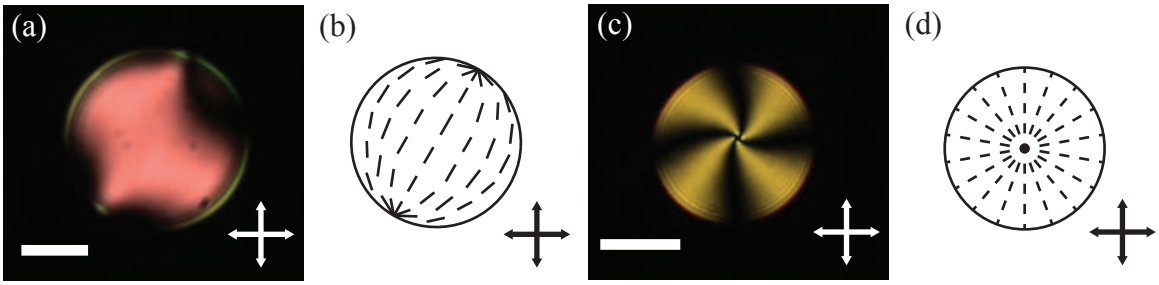

Figure 4.2: A nematic droplet compressed between glass plates in dilute carbopol solution with 1% PVA when view (a) in between a cross-polarizers with the corresponding schematic of the molecules arrangement displayed in (b). (c) and (d) represent the same point of view a nematic droplet in dilute carbopol solution with 16 mM of SDS. Scale bars represent 10 μm.

To make nematic toroidal droplets, we inject a liquid crystal (4-n-pentyl-4'-cyanobiphenyl, 5CB) through a needle into a rotating bath containing a yield-stress material consisting of (i) 1.5 wt% polyacrylamide microgels (carbopol ETD 2020), (ii) 3 wt% ethanol, (iv) 1 wt% polyvinyl alcohol (PVA) and (v) 64.5 wt% ultrapure water. The presence of PVA guarantees degenerate tangential (or planar) anchoring for the liquid crystal at the surface of the droplets; we confirmed this by making spherical droplets and checking their bipolar character under a cross polarizer (see an example in figure. 4.2(a)). For a bipolar droplet, the liquid crystal molecules are expected to arrange in the same fashion as the one shown in figure 4.2(b). Notice that the center is bright because around this location the molecules makes an angle of around 45° to the polarizers which converted a linearly polarized beam into an elliptically polarized state, thus, allowing the beam to pass through the analyzer. We would like to mention that we can also achieve a normal anchoring if we added 16 mM of SDS to a carbopol solution, as seen in figure 4.2(c). In this case, a droplet shows a defect in the center together with four black brushes along the direction of polarization axis of the entrance and exit polarizers. This leads to a molecular arrangement shown in figure 4.2(d). We also note that the continuous phase is neutralized to pH 7, where the sample transmission is more than 90% [85]. However, the most relevant property of this phase is its yield stress, τ_y. During the formation of the torus, the stresses involved are larger than τ_y and hence the continuous phase essentially behaves as if it were a liquid. The combination of the viscous drag exerted by the outer phase over the extruded liquid crystal and its rotational motion causes the liquid crystal to form a curved jet, as shown in figure 4.3(a), which eventually closes onto itself resulting in a toroidal nematic droplet, such as that shown in figure 4.3(b) in bright field and in figure 4.3(c) between cross-polarizers. Once the torus has been formed, the elasticity of the continuous phase provides the required force to overcome the surface tension force that would naturally tend to transform the toroidal droplet into a spherical droplet, as discussed in Chapter 2. The relevant length scale that changes in break-up is the tube radius, a, while for the shrinking it is the inner radius, R (see figure 4.3(b)). The minimum yield stress required to stabilize the toroidal droplet against either transformation is $\tau_y = \Gamma/a_c$ or $\tau_y = \Gamma/R_c$, as discussed in Chapter 3. Using this technique we can successfully generate stable nematic toroids with an aspect ratio or slenderness $\xi = [R + a]/a$.

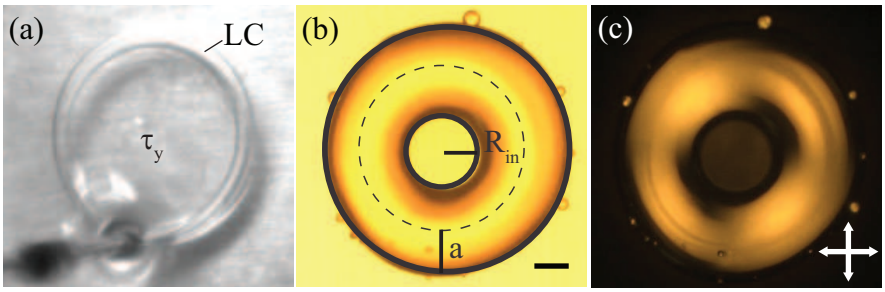

Figure 4.3: (a) Formation of a toroidal liquidcrystal droplet inside a material with yield stress τ_y. The top view of a typical stable toroidal droplet of nematic liquid crystal, having tube and inner radii a and R, is shown in (b) when viewed in bright field and (c) when viewed under cross-polarizers. Scale bar: 100 m.

4.3 Toroidal Nematic Liquid Crystal Droplets

4.3.1 Observations Suggesting a Twisted Nematic Structure

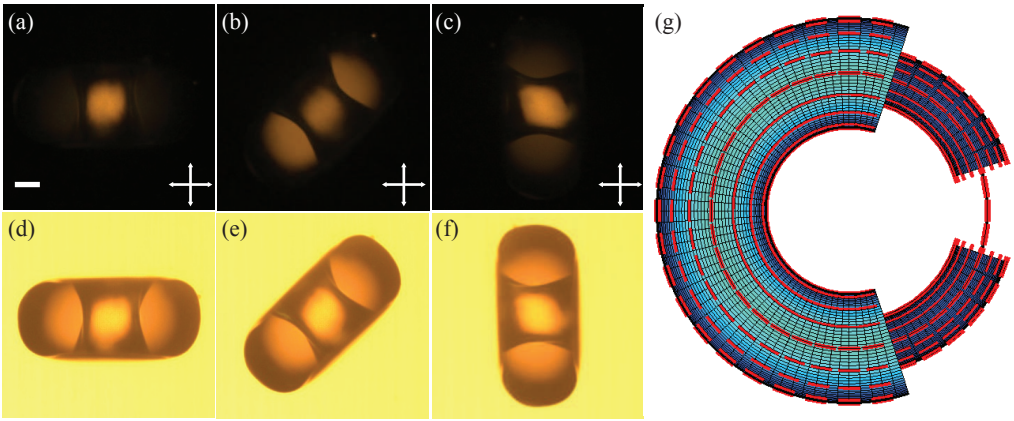

Figure 4.4: (a-c) Side view of a typical toroidal droplet with $\xi = 1.8$ when viewed under cross-polarizers for orientations of 0°, 45° and 90° with respect to the incident polarization direction. Note that the center part of the toroid remains bright irrespective of its orientation. (d-f) shows the corresponding bright field images. The dark regions of the toroid in these images are due to light refraction. Scale bar: 100 μm. (g) A schematic of an axial arrangement of liquid crystal molecules.

When toroidal nematic droplets are observed along their side view under cross-polarizers, their central region remains bright irrespective of the orientation of the droplet with respect to the incident polarization direction, as shown in figure 4.4(a)-(c); the corresponding bright field images are shown in figure 4.4(d)-(f). Note that for an axial torus with its director field along the tube (see figure 4.4(g)) the cross-polarized image should appear black for an orientation of 0° and 90° with respect to the incident polarization direction. Hence our result is suggestive of a twisted structure (note how the light is able to pass through the cross-polarizers when there is a twisted nematic liquid crystal

in between, as shown in figure 4.1(a)). In fact, twisted bipolar droplets also have a central bright region, when viewed between cross-polarizers, irrespective of their orientation [12, 86, 87, 88]. In addition, theoretical studies of DNA in toroidal geometries have also show that the DNA condensate can be twisted as, in this case, some of the bending energy of the untwisted axial structure is released at the price of a small amount of twist energy [23].

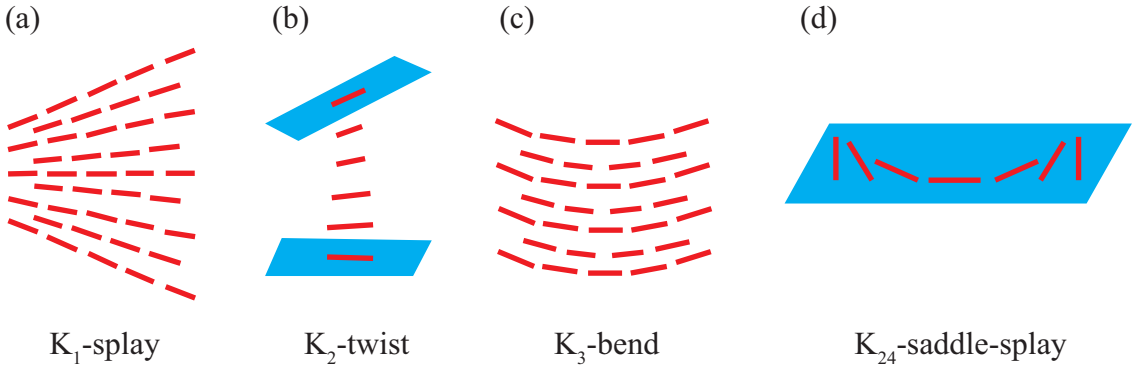

Figure 4.5: A schematic illustrating: (a) splay, (b) twist, (c) bend and (d) saddle-splay arrangement of nematic order.

We consider the distortion energy described using Frank free energy:

$$F = \frac{1}{2}\int dV\left[K_1(\nabla\cdot\mathbf{n})^2 + K_2(\mathbf{n}\cdot\nabla\times\mathbf{n})^2 + K_3(\mathbf{n}\times\nabla\times\mathbf{n})^2\right], \tag{4.1}$$

where, K_1, K_2 and K_3 are elastic constants associated with splay, twist and bend, respectively (see figure 4.5(a)-(c)). All terms in equation (4.1) are all positive indicates that all of the splay, twist and bend arrangement all cost the elastic energy of the system to rise. Therefore, the arrangement for the ground state of the system depends on the relative magnitude of the elastic constant to one another. Note also that the shape of the confining surface also plays a roll in determining the arrangement of the director $\mathbf{n}$. Interestingly, the theory predicts there is a critical value of slenderness, $\xi_c = 1.4$ for 5CB, beyond which the trade off between bend and twist energies is unfavorable and the toroidal DNA condensate remains axial.

To study how the nematic structure changes with the aspect ratio of a torus, we generate toroidal droplets with different ξ and measure the intensity of the central part of the toroidal droplet, when viewed along their side between cross-polarizers, for an orientation of 0° and 45° with respect to the incident polarization direction. We then take the ratio of the two intensity measurements I_{0°/I_{45°, where I_{0° and I_{45° are the average intensities inside the box in figure 4.6(a-c) and (d-f),

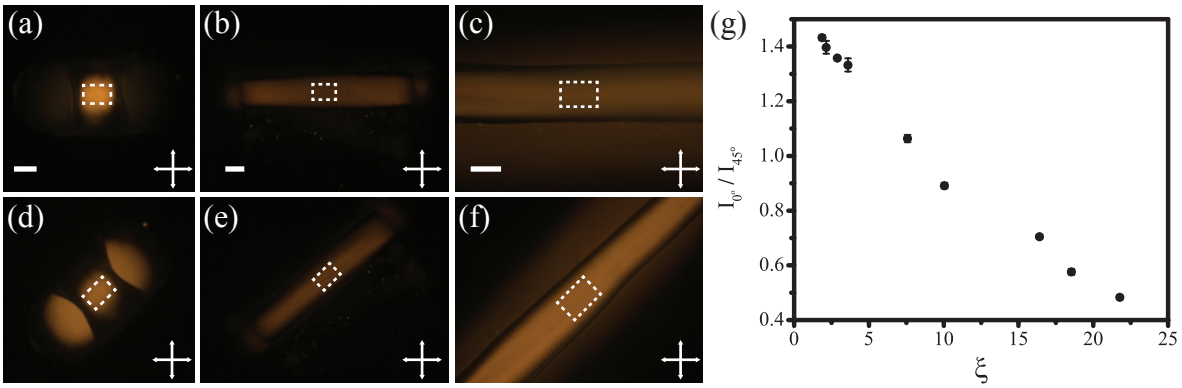

Figure 4.6: Side view of a torus with aspect ratios $\xi = 1.8$ (a,d), $\xi = 7.6$ (b,e), and $\xi = 18.5$ (c,f) when viewed under cross-polarizers for orientations of 0° (a,b,c) and 45° (d,e,f) with respect to the incident polarization direction. The boxes in each diagram indicate the region where the intensities were measured. Scale bar: 200 μm. (g) Ratio of the transmitted intensity through the center of the toroidal droplet when viewed along its side and under cross-polarizers for an orientation of 0° and 45° with respect to incident polarization direction, plotted as a function of its slenderness.

respectively. The ratio I_{0°/I_{45° should be zero for an axial configuration. For a fat toroidal droplet, we find that $I_{0^\circ}/I_{45^\circ} > 1$, suggestive of a highly twisted structure, and a monotonous decrease of I_{0°/I_{45° with increasing ξ, as shown in figure 4.6(g), suggestive of a decreasing twist with increasing slenderness. However, we do not see I_{0°/I_{45° ever approaching zero, even for the highest aspect ratios we explore. Thus we never observe the transition from the twisted to the axial configuration predicted for toroidal DNA condensates.

4.3.2 Theoretical Analysis of Nematic Structure in Toroidal Droplets

To explain the lack of axial structure in our experiments, we consider the full Frank free energy:

$$F = \frac{1}{2}\int dV\left[K_1(\nabla\cdot\mathbf{n})^2 + K_2(\mathbf{n}\cdot\nabla\times\mathbf{n})^2 + K_3(\mathbf{n}\times\nabla\times\mathbf{n})^2\right] - K_{24}\int \mathbf{dS}\cdot(\mathbf{n}\nabla\cdot\mathbf{n} + \mathbf{n}\times\nabla\times\mathbf{n}), \tag{4.2}$$

which, besides the well-known bulk terms representing splay, twist and bend deformations weighted with elastic constants K_1, K_2 and K_3, respectively, also contains the less familiar surface term representing saddle-splay deformations with elastic constant K_{24} (see figure 4.5(d)). The minus sign in the saddle splay terms suggested that the last term can either be positive or negative meaning that it can either increase or lower the energy. Notice also that it is purely a surface term and it is very hard to observed saddle splay by itself without the presence of the other distortions. Thus it is hard

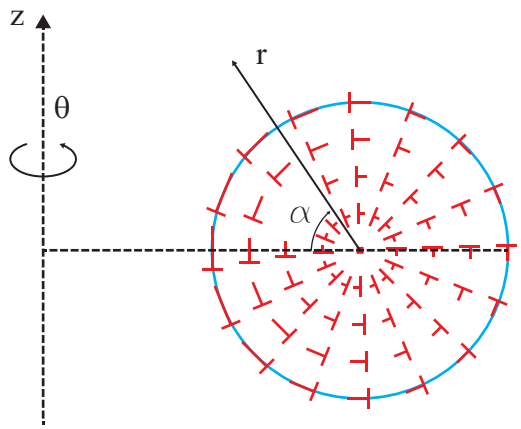

Figure 4.7: Circular cross section of the torus illustrating the relevant coordinates: α is the polar angle, r is the radial distance from the center of the cross section and θ is the azimuthal angle. The nails indicate the tilt direction of the director; it is tilted outwards at the top, where $r = a$ and $\alpha = 90°$, and inwards at the bottom, where $r = a$ and $\alpha = 270°$. The presented configuration corresponds to a twisting strength $\omega = 0.49$, for a torus with aspect ratio $\xi = 2$. Note the structure is doubly twisted. The director configuration inside the whole torus is obtained by rotating the director field in this cross-section around the z-axis.

to measure or study the saddle splay.

Following previous calculations by [23], Vinzenz Koning and Vincenzo Vitelli [102] employ an ansatz for the unit director field, $\mathbf{n} = n_r\mathbf{e}_r + n_\alpha\mathbf{e}_\alpha + n_\theta\mathbf{e}_\theta$, with $\mathbf{e}_r, \mathbf{e}_\alpha$ and $\mathbf{e}_\theta$ the orthonormal basis vectors in the r, θ, α directions, respectively, as shown in figure 4.7. Then the ansatz is built based on several conditions: (i) the director field does not have a radial component $n_r = 0$; this already takes care of the tangential anchoring of $\mathbf{n}$ at the boundary, (ii) the director field is tangential to the central circle of the torus and hence $n_\alpha(r = 0) = 0$, (iii) it is independent of θ due to the rotational symmetry around the azimuthal angle, (iv) we initially assume that there is no splay distortion and thus $\nabla \cdot \mathbf{n} = 0$. The divergence of $\mathbf{n}$ can be written in terms of the metric tensor $g_{\alpha\alpha} = r^2, g_{\theta\theta} = (R_0 + r\cos\alpha)^2$ and $g_{rr} = 1$ of the coordinates $\{r, \theta, \alpha\}$ as following

$$\nabla \cdot \mathbf{n} = \frac{1}{\sqrt{g_{rr}g_{\alpha\alpha}g_{\theta\theta}}}\left[\frac{\partial(n_r\sqrt{g_{\alpha\alpha}g_{\theta\theta}})}{\partial r} + \frac{\partial(n_\alpha\sqrt{g_{rr}g_{\theta\theta}})}{\partial\alpha} + \frac{\partial(n_\theta\sqrt{g_{rr}g_{\alpha\alpha}})}{\partial\theta}\right], \tag{4.3}$$

which after considering the boundary conditions (i) and (iii) reduces to

$$\partial_\alpha(n_\alpha\sqrt{g_{\theta\theta}}) = 0\,, \tag{4.4}$$

where we have used $g_{rr} = 1$. Hence, any anzatz of the form $n_\alpha = f(r)/\sqrt{g_{\theta\theta}}$ with an arbitrary function $f(r)$ would satisfy equation (4.4). To satisfy the condition (ii), we choose $f(r) = \omega\xi r$,

which yields

$$n_\alpha = \frac{\omega \xi r}{R_0 - r\cos\alpha}\,. \tag{4.5}$$

The polar component of $\mathbf{n}$ is obtained from the normalization condition ($|\mathbf{n}| = 1$); then $n_\theta = \sqrt{1 - n_\alpha^2}$. The variational parameter ω determines the nematic organization, which continuously evolves from the axial structure, where $\omega = 0$ and hence $\mathbf{n} = \mathbf{e}_\alpha$, to a twisted configuration, where $\omega \neq 0$. Detailed inspection of the nematic arrangement inside the torus reveals that the configuration is doubly twisted, as shown in figure 4.7, where we use nails to represent the out-of-plane tilt of the director. The stable nematic organization is obtained from minimization of the elastic free energy with respect to ω. After volume integration of equation 4.2 using the previous ansatz, we obtain the energies associated with the bend, twist and saddle-splay distortions:

$$\frac{F_3}{\pi^2 K_3 a} = 2\left(\xi - \sqrt{\xi^2 - 1}\right) + \frac{\left(1 - 9\xi^2 + 6\xi^4 + 6\xi\sqrt{\xi^2-1} - 6\xi^3\sqrt{\xi^2-1}\right)\xi^2}{(\xi^2-1)^{3/2}}\omega^2 + O\left(\omega^4\right)\,, \tag{4.6a}$$

$$\frac{F_2}{\pi^2 K_2 a} = \frac{4\xi^2}{(\xi^2-1)^{3/2}}\omega^2 + O\left(\omega^6\right)\,, \tag{4.6b}$$

$$\frac{F_{24}}{\pi^2 K_{24} a} = -\frac{4\xi^2}{(\xi^2-1)^{3/2}}\omega^2\,. \tag{4.6c}$$

Note that the equation (4.6a) and (4.6b) are the expansion up to the leading order in ω, while the equation (4.6c) is an exact solution.

By combining all the energy terms in equation 4.6, we obtain, to leading order in ω:

$$\frac{F}{\pi^2 K_3 a} \approx 2\left(\xi - \sqrt{\xi^2 - 1}\right) + \frac{\left(1 - 9\xi^2 + 6\xi^4 + 6\xi\sqrt{\xi^2-1} - 6\xi^3\sqrt{\xi^2-1}\right)\xi^2 + 4(K_2 - K_{24})\xi^4/K_3}{(\xi^2-1)^{3/2}}\omega^2\,. \tag{4.7}$$

The physical implications of this equation are better seen in the limit of large ξ, where the Frank free energy to quartic order in ω reads:

$$\frac{F}{\pi^2 K_3 a} \approx \frac{1}{\xi} + \left(4\frac{K_2 - K_{24}}{K_3}\xi - \frac{5}{4\xi}\right)\omega^2 + \frac{1}{2}\xi\omega^4\,. \tag{4.8}$$

Similar to the Landau theory of magnetism [89], the switching of the sign of the quadratic term in equation 4.8 from positive to negative establishes a spontaneous symmetry-breaking transition from axial to the doubly twisted configuration. Since the relevant quadratic term is zero when $\frac{K_2 - K_{24}}{K_3} = \frac{5}{16\xi_c^2}$, the relative magnitude of twist and saddle-splay determines whether the axial or the

doubly twisted structure is the preferred nematic arrangement. When $\frac{K_2-K_{24}}{K_3} > 0$, the quadratic term can be either negative or positive depending on the slenderness. Hence there is a critical ξ_c above which the lowest energy state corresponds to the axial torus; this state is shown by the dashed line in figure 4.8(a). Note, however, that ξ_c can be pushed to much higher values compared to the saddle-splay free case. Hence the saddle-splay modulus acts as an external field that tends to align **n** along the θ direction at the surface of the torus. Below ξ_c, the lowest free energy state has nonzero ω, corresponding to the doubly twisted torus. In this case, there are two minima of equal depth corresponding to the two possible configurations in which the handedness of the twisted nematic director is either positive or negative, as shown by the continuous line in figure 4.8(a). Remarkably, when $\frac{K_2-K_{24}}{K_3} < 0$, the quadratic term is always negative and the only possible structure is the doubly twisted configuration. This result holds irrespective of ξ, as shown in figure 4.8(b), where we plot the phase boundary, obtained from equation 4.7 separating the axial from the doubly twisted regions, in a ξ versus K_{24}/K_2 diagram. For 5CB, $K_{24} \approx K_2$ [90, 91, 92, 93, 94] and hence from the axial to doubly twisted transition is either pushed to extremely slender tori or it is completely lost, consistent with our experiment observations (see section 4.3.5).

4.3.3 Wave Guiding Through Nematic Toroidal Droplets

As indicated by figure 4.6(g), the intensity ratio I_{0°/I_{45° is dependent on the aspect ratio of the torus. This is related to the amount of twist inside the torus. In this section, we will present a way to quantify the twist angle using the formula of Jones matrices. We take a vertical trajectory from $\alpha = 90^\circ$ to $\alpha = 270^\circ$ at certain θ along where **n** progressively rotates, as shown in figure 4.9(a). This path can be considered as consisting of N birefringent plates with the slow axis oriented in the same direction as the local director orientation spanning the tube of the torus. The phase retardation of each plate is given by [96]

$$\frac{\Phi}{N} = \frac{2\pi}{\lambda}\frac{d}{N}(n_e - n_o)\,, \tag{4.9}$$

where λ is the wavelength of the light passing through the nematic medium, n_e and n_o are the indices of refraction of the slow and fast axes of the nematic phase, respectively, and $d = 2a$ is diameter of the circular cross-section. The fast and slow axes of the plate are considered perpendicular and parallel to the local director orientation, respectively. Then the overall Jones matrix for these N

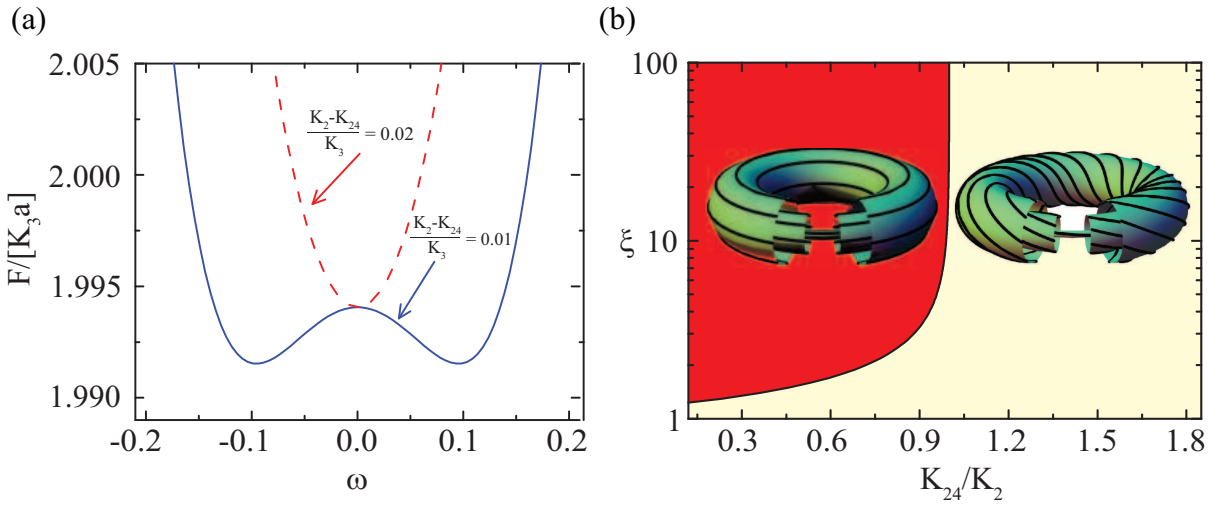

Figure 4.8: (a) Normalized elastic free energy, $F/(K_3a)$, versus the variational parameter ω, for $\xi = 5$ and two different values of $(K_2\text{-}K_{24})/K_3$. For $(K_2\text{-}K_{24})/K_3 = 0.02$ (red dashed line), there is only one energy minimum at $\omega = 0$ corresponding to the axial structure shown schematically on the left in panel (b). For$(K_2\text{-}K_{24})/K_3 = 0.01$ (blue continuous line), there are two minima located at $\omega \approx \pm 0.1$ corresponding to the two possible handedness of the doubly twisted structure shown schematically on the right in panel (b). The ratio $K_{24}/K2$ determines whether there is a transition between the axial and the doubly twisted structure and if so what is the critical value of ξ, or whether the doubly twisted structure remains irrespective of ξ. This is shown in the structural phase diagram of (b), where we have used that $K_2 = 0.3K_3$ for 5CB [101]. Since for 5CB, $K_{24} \approx K_2$ [90, 91, 92, 93, 94] the axial to double twist transition is either completely lost or shifted to very high values of ξ, explaining our experimental observations.

plates is the product of the Jones matrices for all individual plates and is given by

$$\mathbf{M} = \prod_{m=1}^{N} \mathbf{R}(-m\phi/N)\mathbf{W}_0\mathbf{R}(m\phi/N)\,, \tag{4.10}$$

where

$$\mathbf{R}(m\phi/N) = \begin{bmatrix} \cos m\phi/N & \sin m\phi/N \\ -\sin m\phi/N & \cos m\phi/N \end{bmatrix},$$

represents the rotation of the m^{th} plate by angle ϕ/N (where ϕ is the angle between the orientation of the director at the entrance and at the exit) and $\mathbf{W}_0$ is the Jones matrix of a single retardation plate.

The polarization state of the light can be written as a Jones vector

$$\mathbf{V} = \begin{pmatrix} V_e \\ V_o \end{pmatrix}, \tag{4.11}$$

where V_e and V_o are polarization states in the local principle coordinate system (*eo* coordinates

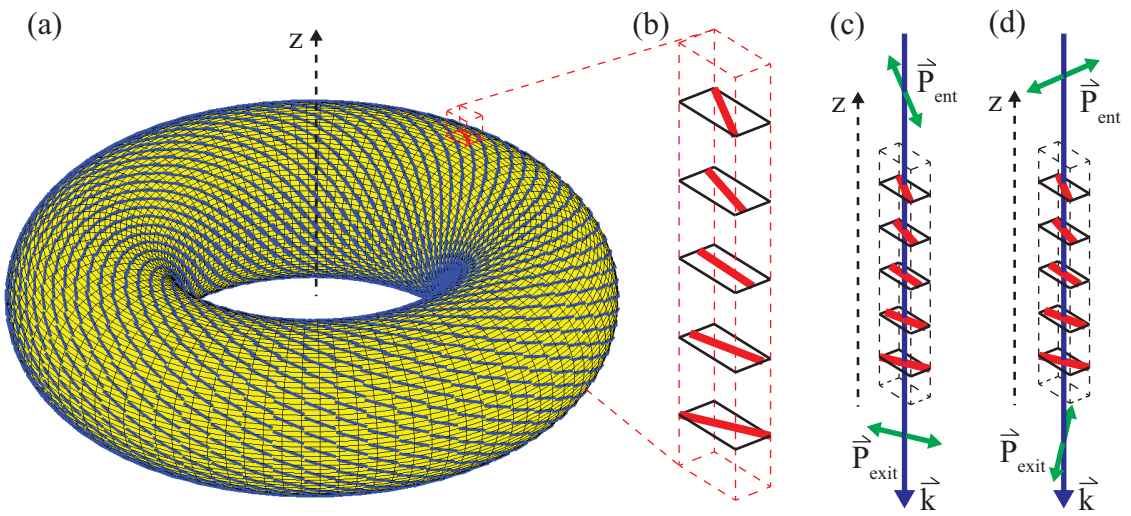

Figure 4.9: (a) Schematic representation of a doubly twisted torus. (b) A section taken from the nematic torus subdivided into a number N of a birefringent plates with their *e* (slow) axis oriented in the same direction as the local director orientation as depicted in thick red line in each plate. (c,d) For *e* (*o*) waveguiding, the initial state of polarization of the incident light $\vec{P}_{ent}$ is parallel (perpendicular) to local orientation of the director at the entrance and follows (rotates in the opposite direction to) the twist of the nematic and then the final state of polarization $\vec{P}_{exit}$ comes out parallel (perpendicular) to the local director orientation at the exit.

system), respectively, and under the same coordinates

$$\mathbf{W}_0 = \begin{bmatrix} e^{-i\Phi/2N} & 0 \\ 0 & e^{i\Phi/2N} \end{bmatrix}, \tag{4.12}$$

provided that the absolute phase difference is neglected.

Using the rotation product $\mathbf{R}(\theta_1)\mathbf{R}(\theta_2) = \mathbf{R}(\theta_1 + \theta_2)$, the overall Jones matrix equation (4.10) becomes

$$\mathbf{M} = \mathbf{R}(-\phi)\left[\mathbf{W}_0\mathbf{R}\left(\frac{\phi}{N}\right)\right]^N. \tag{4.13}$$

Applying Chebyshev's identity for unimodular matrices [97] to equation (4.13) and taking the limit $N \to \infty$ yields

$$\mathbf{M} = \begin{bmatrix} \cos\phi & -\sin\phi \\ \sin\phi & \cos\phi \end{bmatrix}\begin{bmatrix} \cos X - i\frac{\Phi}{2}\frac{\sin X}{X} & \phi\frac{\sin X}{X} \\ -\phi\frac{\sin X}{X} & \cos X + i\frac{\Phi}{2}\frac{\sin X}{X} \end{bmatrix}, \tag{4.14}$$

where $X = \sqrt{\phi^2 + \frac{\Phi}{2}^2}$. Equation (4.14) is the exact expression for the Jones matrix of a linear twisted nematic LC plate.

If we use equation (4.11) as the incident polarization state of light, then the emerging polarization state of light after passing through the twisted nematic LC is

$$\begin{pmatrix} V'_e \\ V'_o \end{pmatrix} = \begin{bmatrix} \cos X - i\frac{\Phi}{2}\frac{\sin X}{X} & \phi\frac{\sin X}{X} \\ -\phi\frac{\sin X}{X} & \cos X + i\frac{\Phi}{2}\frac{\sin X}{X} \end{bmatrix} \begin{pmatrix} V_e \\ V_o \end{pmatrix}, \tag{4.15}$$

Now consider a case where an input beam of light is polarized in the direction parallel to the director of the LC at the entrance of the plate. The Jones vector representing the incident polarization is

$$\begin{pmatrix} V_e \\ V_o \end{pmatrix} = \begin{pmatrix} 1 \\ 0 \end{pmatrix}. \tag{4.16}$$

Using equation 4.15, the output polarization is

$$\begin{pmatrix} V'_e \\ V'_o \end{pmatrix} = \begin{pmatrix} \cos X - i\frac{\Phi}{2}\frac{\sin X}{X} \\ -\phi\frac{\sin X}{X} \end{pmatrix}, \tag{4.17}$$

which in general corresponds to elliptically polarized light.

In our experiment the tube of the nematic toroidal droplet is usually about 200μm in diameter, and the birefringence ($n_e - n_o$) of 5CB is 0.15 at $\lambda \approx 550$ nm [95]. By applying these parameters to equation (4.9) and dividing by the value of the maximum twist angle of $\phi \sim \pi/2$ we get the ratio of the total twist angle to the total phase retardation angle to be $\phi/\Phi \approx 1/200 << 1$; this is called Mauguin limit [96]. Using this approximation, we can re-write equation 4.17 as follows:

$$\begin{pmatrix} V'_e \\ V'_o \end{pmatrix} = \begin{pmatrix} e^{-i\Phi/2} \\ 0 \end{pmatrix}. \tag{4.18}$$

This indicates that (for $\phi << \Phi$) if the direction of polarization of the beam at the entrance is parallel to the entrance director then we can consider the beam's polarization state to follows the twist of the nematic LC medium and as a result the direction of polarization at the exit is also going to be parallel to the exit director, as shown in figure 4.9(c), where $\vec{k}$ is the beam's propagation direction. This is called $e-mode$ wave guiding. Similarly, for an input beam of light with its polarization perpendicular to the local director of the LC at the entrance, the Jones vector is

$$\begin{pmatrix} V_e \\ V_o \end{pmatrix} = \begin{pmatrix} 0 \\ 1 \end{pmatrix}. \tag{4.19}$$

From equation (4.15), the output polarization state of the beam in the limit $\phi/\Phi \to 0$ is given by

$$\begin{pmatrix} V'_e \\ V'_o \end{pmatrix} = \begin{pmatrix} 0 \\ e^{i\Phi/2} \end{pmatrix}, \tag{4.20}$$

where, in this case, the direction of polarization of the beam at the entrance and exit are perpendicular to the entrance and exit director, as shown in figure 4.9(d). This is $o-mode$ wave guiding.

Thus for our experiment, we can assume that if the beam propagating along the z-direction has polarization state parallel or perpendicular to the director at the location ($r = a$, $\alpha = 90°$) then the exit polarization state of that beam will also be the parallel or perpendicular to the director at the exit location ($r = a$, $\alpha = 270°$) as well.

4.3.4 Identifying the Twist Parameter ω

Exploiting wave guiding through our nematic tori, we can determine the twist angle ϕ between the top ($r = a$, $\theta = 90°$) and bottom ($r = a$, $\theta = 270°$) of the nematic torus, which allows for experimental determination of parameter of ω. In order to understand how to experimentally measure ϕ, we investigate the transmitted intensity of the light passing through the nematic toroidal droplet from top to bottom of the torus. First, consider a beam of linearly polarized light of general orientation with respect to the entry director passing through a twisted LC cell, the Jones vectors of the incident and transmitted polarized states are given by

$$\begin{pmatrix} V_x \\ V_y \end{pmatrix} = \begin{pmatrix} \cos\phi_{ent} \\ \sin\phi_{ent} \end{pmatrix}, \tag{4.21a}$$

$$\begin{pmatrix} V'_x \\ V'_y \end{pmatrix} = \begin{pmatrix} \cos\phi_{exit} \\ \sin\phi_{exit} \end{pmatrix}, \tag{4.21b}$$

where ϕ_{ent} and ϕ_{exit} are the angles that the polarization axes of the input and the output polarizer (analyzer) make with the director at the entrance and exit of the twisted LC, respectively, as shown in figure 4.15(a). Applying the Jones matrix method, the transmitted intensity is

$$T = |\mathbf{V}'^{*} \cdot \mathbf{M}\mathbf{V}|^2, \tag{4.22}$$

where $\mathbf{V}$ and $\mathbf{V}'$ are the input and output Jones vectors for the polarization states given by equation (4.21), and $\mathbf{M}$ is given by equation (4.14). After the matrix multiplication we can write the

transmission as [96]

$$T = |A + iB|^2 \,, \tag{4.23a}$$

$$A = \cos X \cos \phi - \phi_{exit} + \phi_{ent} + \phi \frac{\sin X}{X} \sin \phi - \phi_{exit} + \phi_{ent} \,, \tag{4.23b}$$

$$B = -\frac{\Phi \sin X}{2X} \cos \phi - \phi_{exit} - \phi_{ent} \,, \tag{4.23c}$$

where X and Φ are defined in subsection 4.3.3. According to this formula, maximum transmission of $T = 1$ only occurs: (i) at the wave guiding locations ($\phi_{ent} = 0°$ for $e - mode$ or $90°$ for $o - mode$)

$$\tan 2\phi_{ent} = \frac{\phi}{X} \tan X \tag{4.24}$$

and (ii) when the exit polarizer is parallel $\phi_{exit} = \phi$ for $e - mode$ or perpendicular $\phi_{exit} = \phi - 90°$ for $o - mode$ to the exit director

$$\phi_{ent} + \phi_{exit} - \phi = 0 \,. \tag{4.25}$$

This is demonstrated in figure 4.10(b) where we plotted the transmission using equation (4.23a) as a function of ϕ_{exit} with $\phi = 30°$ for $\phi_{ent} = 0$ (solid red line), $\phi_{ent} = 90°$ (solid blue line) and we never see the transmission reaches maximum when $\phi_{ent} = 45°$ (dashed line). While the maximum in T reflects when the direction of polarization of the exit beam is parallel to the analyzer, the minimum in T, which happens when ϕ_{exit} continues to rotate another $90°$, reflects that the direction of polarization is now perpendicular to the analyzer.

To find the twist parameter ω, we will need to express the nematic field in terms of (x, y, z) coordinates using

$$n_x = n_\alpha \sin \alpha \cos \theta - n_\theta \sin \theta \,, \tag{4.26a}$$

$$n_y = n_\alpha \sin \alpha \sin \theta + n_\theta \cos \theta \,, \tag{4.26b}$$

$$n_z = n_\alpha \cos \alpha \,. \tag{4.26c}$$

Let $\theta = 0$. Then $\mathbf{n}_t = \begin{pmatrix} \omega \\ \sqrt{1-\omega^2} \end{pmatrix}$ and $\mathbf{n}_b = \begin{pmatrix} -\omega \\ \sqrt{1-\omega^2} \end{pmatrix}$ for the top and bottom of the torus, respectively. Note that we left out the z-component since it is equal to zero at these locations. Then using $\cos \phi = \mathbf{n}_t \cdot \mathbf{n}_b$, we can derive the expression for the twist parameter in terms of the twist angle

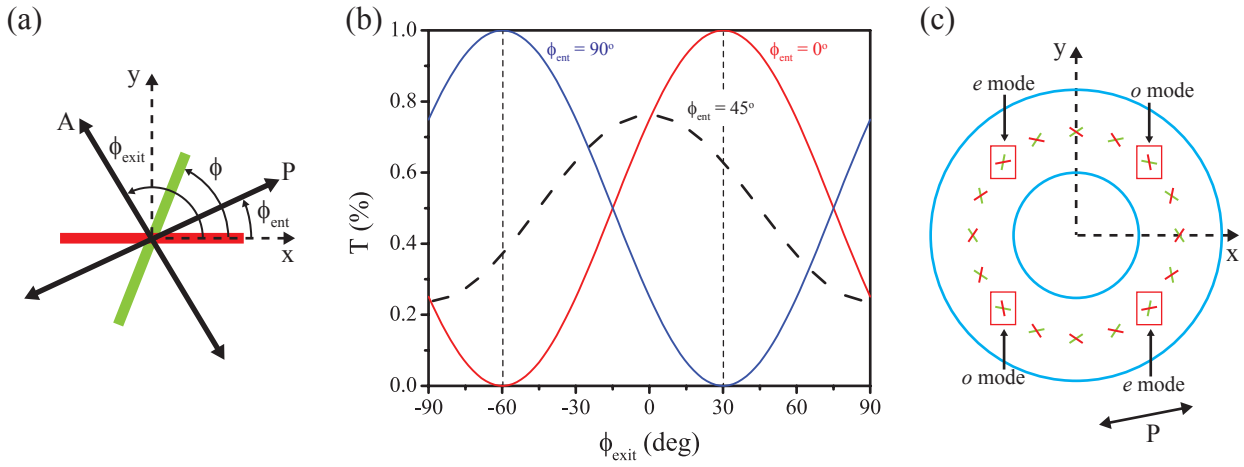

Figure 4.10: (a) Schematic indicating the orientation of the polarizer axes. The entrance director (shown in red) is oriented along the x-axis. ϕ_{exit} is the angle between the entrance polarizer and the entrance director. ϕ is the angle between the entrance and the exit director (shown in green). ϕ_{exit} is the angle between the entrance director and the exit polarizer. (b) Plots of transimission as a function of ϕ_{exit}. The red solid line indicate a transmissions at $e-mode$ waveguiding ($\phi_{ent} = 0°$) while the blue solid line indicate a transmissions at $o-mode$ waveguiding ($\phi_{ent} = 90°$) in both case $\phi = 30°$. The dashed line shows a tranmission at a location where $\phi_{ent} = 45°$. (c) Schematic showing the waveguiding locations for the indicated orientations of polarizer and director orientation at the top ($r = a$, $\alpha = 90°$ shown in red) and at the bottom ($r = a$, $\alpha = \alpha = 270°$ shown in green) of the tube of the torus for positive ω. $\vec{P}$ indicates the orientation of the polarizer.

as

$$\omega = sign(\phi)\sqrt{\frac{1-\cos\phi}{2}}\,. \tag{4.27}$$

Note that the sign of ω is related directly to the sign of ϕ. Thus the director field and the waveguiding locations (for a given polarizer orientation) of a torus from anzatz equation (4.5) can be predicted once ϕ is obtained. Figure 4.10(c) shows a plot for the directors at $r = a$ and $\alpha = 90°$ (shown in red) together with the directors at $r = a$ and $\alpha = \alpha = 270°$ (shown in green) with $\phi = 30°$ and $\xi = 2.5$ indicates that there are four regions where waveguiding occurs and the locations where they are located depend on the direction of polarizer's orientation.

4.3.5 Twist Angle Measurement

The method to measure the twist angle relies on the fact that linearly polarized light follows the twist of a nematic liquid crystal if the polarization direction is either parallel ($e-mode$) or perpendicular ($o-mode$) to the nematic director at the entrance of the sample, provided the Mauguin limit is

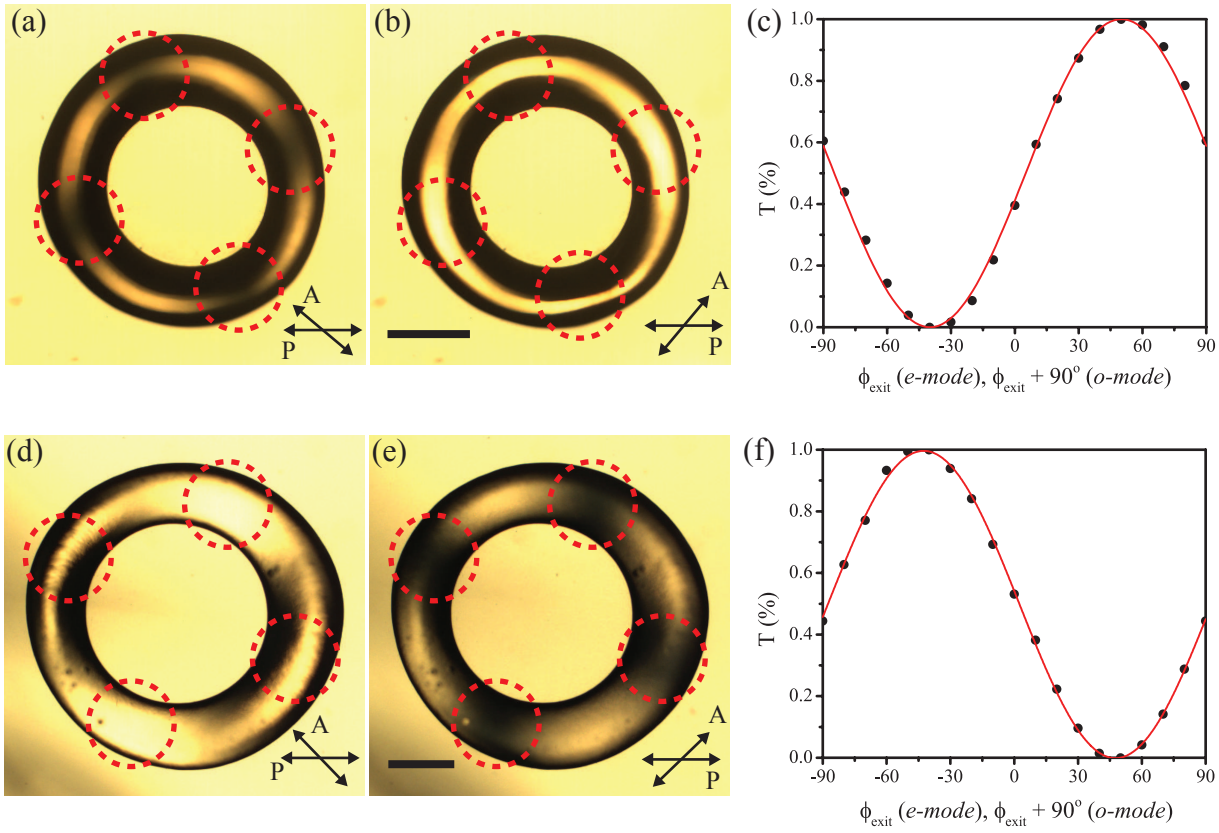

Figure 4.11: The sense of rotation of the analyzer indicates the nematic arrangement is right-handed in the top row ($\xi \approx 3.4$) and is left-handed in the bottom row ($\xi \approx 3.6$). Top view of a torus with (a) $\xi \approx 3.4$ and (e) $\xi \approx 3.6$ when viewed from the top and at the minimum of the transmission curve. Top view of a torus with (b) $\xi \approx 3.4$ and (d) $\xi \approx 3.6$ when viewed from the top and at the maximum of the transmission curve. We measure T along the four wave guiding regions that are observed, which are brightest and darkest for the indicated position of the polarizer and the analyzer. (c,f) Transmission, T, as a function of the angle between the incident polarization direction and the analyzer, ϕ_{exit} for torus with aspect ratio $\xi \approx 3.4$ and $\xi \approx 3.6$, respectively. The line is a fit to the theoretical expectation in the Mauguin limit [96] with the twist angle, ϕ, as the only free parameter. We obtain $\phi \approx 50°$ for (a) and (b) and $\phi \approx -44°$ for (d) and (e).

fulfilled (see section 4.3.3 for more details). We monitor the transmitted intensity, T, of a whole torus by looking down on it from the z-axis, while keeping the polarizer stationary, we rotate the analyzer in the counter clockwise direction with respect to the polarizer.

The location where $e-mode$ or $o-mode$ waveguiding occurs can be identified as a region that, depending on the orientation of the analyzer with respect to the polarizer, exhibits either a maximum or minimum T, as shown in figure 4.11(a) and (b). It is along these regions that we measure T and an example of a result for a torus with for $\xi \approx 3.4$ is plotted as a function of the angle between the analyzer and polarizer, which is equal to ϕ_{exit} for $e-mode$ (or $\phi_{exit} + 90°$ for $o-mode$), as shown in figure 4.11(c). Here the maximum transmission occurs at $\phi \approx 50°$, which as predicted by equation (4.25) corresponds to the twist angle ϕ. This value is confirmed when fitting the results to the theoretically expected transmission equation 4.23a leaving ϕ as free parameter (see solid line in figure 4.11(c)). By inserting the value of ϕ into equation (4.27), we can obtain ω. The positive value of ϕ also indicates that the twist is right-handed. The image of the torus in figure 4.11(a) and (b) exhibits four regions where waveguiding occurs as seen by the predicted theoretical result from the last subsection. For a given polarizer orientation, there are always four waveguiding regions (2 $e-mode$ and 2 $o-mode$) irregardless of the twist angle ϕ. This is also observed for a torus with left-handed twist (see figure 4.11(d)-(f)); note that the value of ϕ obtained in this case is $\approx -44°$.

In order to determine how ω changes with ξ, we generate and monitor ϕ for tori of various ξ. From the observations of the twist angle over the experimentally accessible ξ-range, we find that the twist is non-zero and that it monotonously decreases with increasing aspect ratio, as shown in figure 4.12. Remarkably, these features are captured by our theoretical calculation for large ξ, as shown by the dashed line in the same figure. We note that the deviations of the experiment and the theory for small ξ results from the inadequacy of the ansatz in describing the highly twisted structures observed experimentally at these low values of ξ. This is because under a constrain where $n_\alpha(r, \alpha, \omega) \leq 1$, the maximum value of ω using the current ansatz equation (4.5) is

$$\omega_{max} = 1 - \frac{1}{\xi}. \tag{4.28}$$

and $\omega_{max} \to 0$ as $\xi \to 0$ indicates that the current ansatz cannot provide enough twist at low ξ. This can be partially resolved by introducing a second variational parameter Θ into the ansatz such that

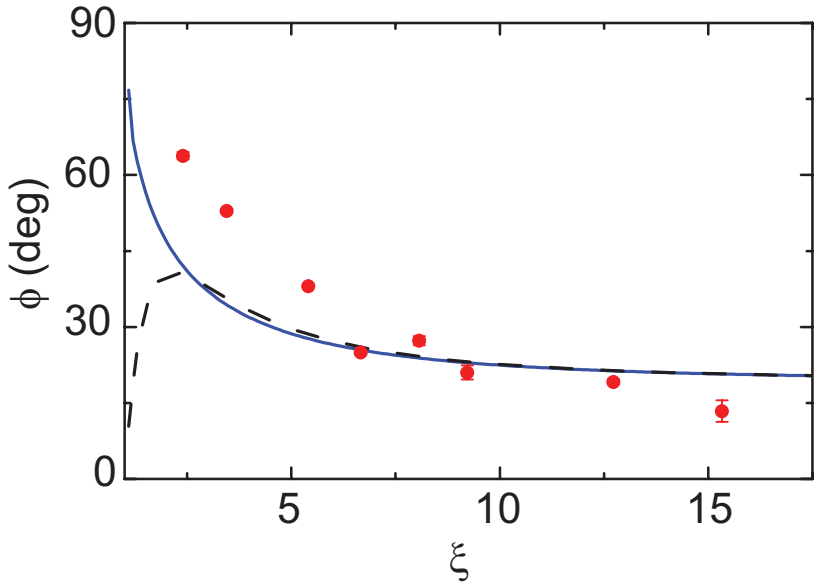

Figure 4.12: Twist angle as a function of ξ. The dashed line represents the theoretical prediction based on equation 4.7, for $K_{24} = 1.02K_2$. The solid line represents the theoretical prediction based on the improved ansatz including the second variational parameter Θ for the same value of K_{24}, where we have used that $K_1 = 0.64K_3$ for 5CB [103].

[102]

$$n_\alpha = \frac{\omega \xi r}{R_0 - \Theta r \cos\alpha}\,. \tag{4.29}$$

Using this improved ansatz,

$$\omega_{max} = 1 - \frac{\Theta}{\xi}\,, \tag{4.30}$$

allowing ω to continue growing as $\xi \to 1$. From equations 4.29 and 4.30, we see that we can affect the value of n_α by varying Θ, while ϕ still depends solely on ω, since ϕ, by definition, is the angle difference between the director orientation at $(r = a, \alpha = \pi)$ and $(r = a, \alpha = 3\pi/2)$. The introduction of Θ, however, allows the nematic field to splay because $\nabla \cdot \mathbf{n}$ is now not equal to zero unless Θ is equal to one. With this improved ansatz, we minimized F with respect to ω and Θ to obtain ϕ as a function of ξ and then plot the result as the solid line in figure 4.12, which qualitatively captures the experimental trend for all aspect ratios. By further comparing the experiment to the theory in the high ξ-region, we obtain a value for the saddle-splay elastic constant of $K_{24} = 1.02K_2$, which is slightly larger than the twist elastic constant, confirming our previous conclusions and supporting our interpretation on the relevance of saddle-splay distortions. However, our analysis

cannot exclude the possibility of a slightly smaller value of K_{24} and hence of a twisted-to-axial transition for extremely large ξ.

4.4 Nematic Droplets with Multiple Handles

4.4.1 Computer simulation of Nematic Double Toroid

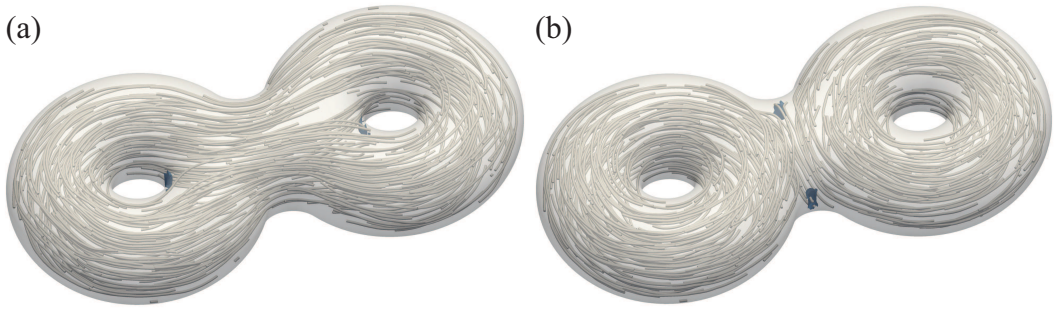

Figure 4.13: The two textures found by computer simulations of a typical double torus. They both have two defects (solid spots) on the surface of the double torus, each with topological charge -1, located in regions of negative Gaussian curvature, either (a) at the innermost regions of the inner ring of each torus or (b) at the outermost regions where the individual tori meet.

Our results indicate that nematic toroids have no defects in their ground state. However, this should not be the case if we add handles since the Euler characteristic and hence the total topological charge decreases by -2 with every additional handle. However, the Poincaré-Hopf theorem provides only a conservation law that prescribes the total topological surface charge. It tells us nothing about the individual defect charges, whether they are point defects (called boojums) or singular lines [98] inside the droplet terminating at the boundaries, the number of defects or their locations. To understand defect formation in higher genus nematic droplets, we take a look at a computer simulation model of nematic texture of double toroid generated by Martin Bates in [102](see the acknowledgement) using a simple nematogenic lattice model [99]. For this model, the elastic constants are equivalent, $K_1 = K_2 = K_3$, and no special consideration of the saddle-splay contributions to the elastic energy is taken. Hence, we do not expect to observe any twist in the resulting structures. For the double torus, we find two types of defect configurations with comparable energy. Both of these are either located at the innermost regions of the inner ring of each torus, as shown in figure 4.13(a), or in the outermost regions where the individual tori meet, as shown in figure 4.13(b).

In both cases, the defects are located in regions of local saddle geometry where the Gaussian curvature, G, defined as the product of the two principal curvatures, is negative. This finding shows similarity with the theoretical insight that negatively charged defects in a two-dimensional curved nematic liquid crystal are attracted to regions with negative curvature [3, 100, 101].

4.4.2 Defects Configuration of Figure Eight Nematic Liquid Crystal

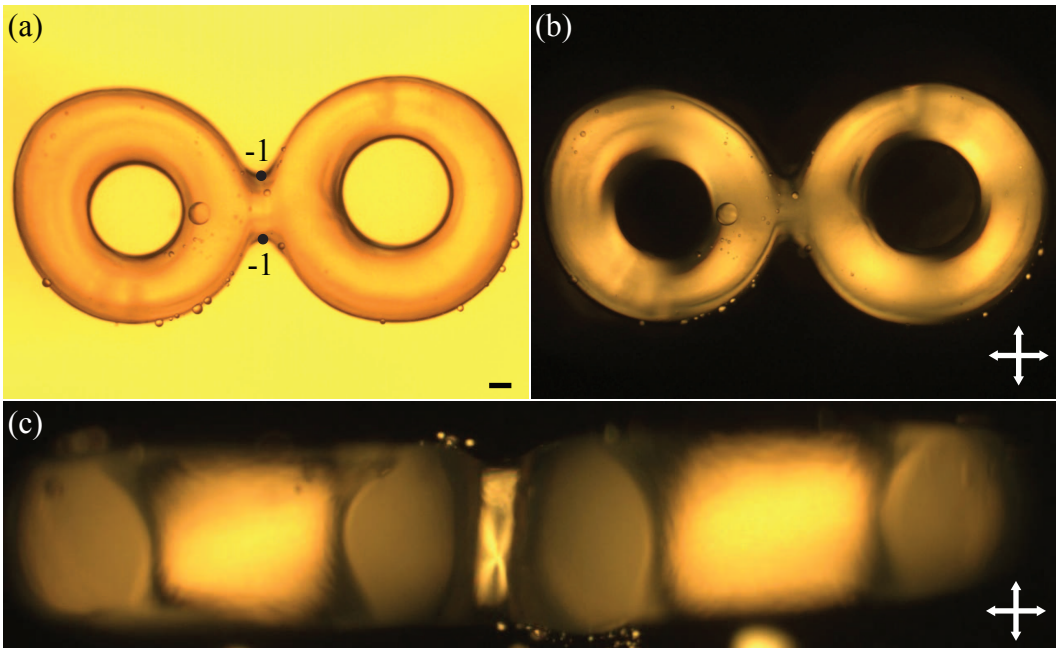

Figure 4.14: (a) Top view of a double toroid in bright field. Solid dark circles indicate the location of the two -1 surface defects. (b) The same image under cross-polarizers. (c) Side view of the double toroid under cross-polarizers when focused at its back. The four black brushes in the region where the two single toroids meet indicate the presence of a topological defect with charge $|s| = 1$. The sign of this charge is determined by rotating the double torus. Since the brushes rotate in the same sense as the rotation, we conclude the defect has charge $s = -1$. By changing the focal plane, we confirm there is another $s = -1$ defect at the front of the double toroid. Scale bar: 100 μm

To investigate handled droplets experimentally, we exploit the elastic character of the continuous phase below the yield stress and generate two nearby single tori which are merged together by the addition of liquid crystal in the region between them (see details in Appendix E). The top view of a typical droplet is shown in figure 4.14(a); the corresponding cross-polarized image is shown in figure 4.14(b). Interestingly, when this droplet is viewed along its side between cross-polarizers, we observe that there is a defect in the very center of the droplet, as shown in figure 4.14(c). We also observe the four-brush texture typical of $|s| = 1$ defects. To determine the sign of this charge, we

rotate the double torus and observe that the black brushes also rotate in the same direction, indicating that the defect has a topological charge of -1 [103]. This defect is in the back of the droplet when looked along its side, with an identical defect on its front. Hence there are two defects of charge -1 on the surface of the double torus, consistent with the constraints imposed by the Poincaré-Hopf theorem. Furthermore, they are located in regions with $G < 0$, consistent with the findings of the computer simulations by Martin Bates. However, the location of the defects obtained experimentally is consistent with just one of the two configurations obtained in the computer simulations. The other configuration has not been observed in our experiments, presumably because the way the double torus is made biases the director towards the structure in figure 4.13(b).

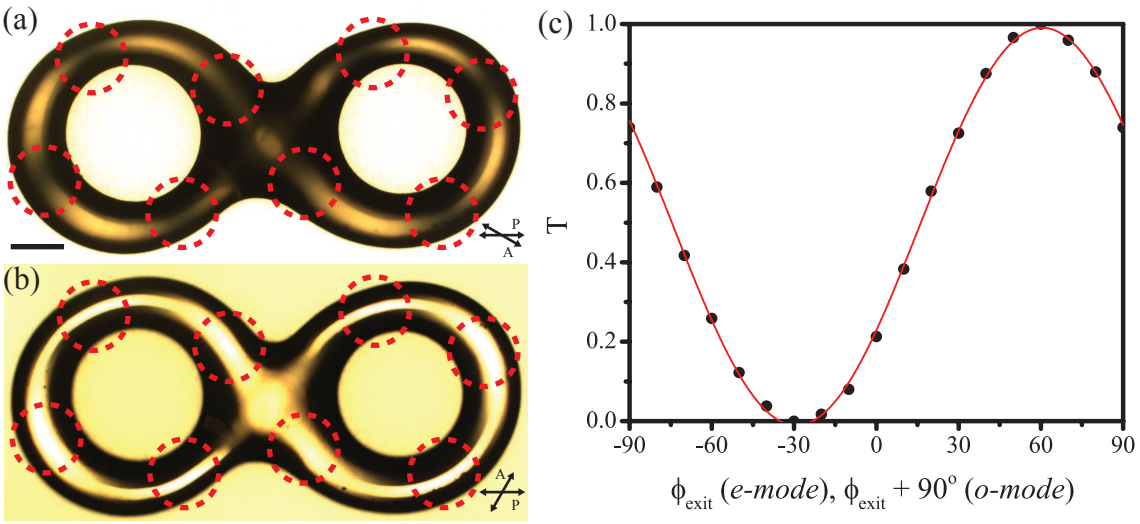

Figure 4.15: (a) Transmission, T, as a function of the angle between the incident polarization direction and the analyzer, ϕ_{exit}. The line is a fit to the theoretical expectation in the Mauguin limit [96] with the twist angle, ξ, as the only free parameter. We obtain $\phi \approx 50°$. The sense of rotation of the analyzer indicates the nematic arrangement is right-handed; this likely results from the way the torus is generated, as all tori generated in the same way have the same handedness. (b) Top view of a torus with $\xi \approx 3.5$ when viewed from the top and at the maximum of the transmission curve. (c) Top view of the same torus at the minimum of the transmission curve. We measure T along the four wave guiding regions that are observed, which are brightest and darkest for the indicated direction of the polarizer and the analyzer in (a).

We also note that the nematic structure of double toroid is twisted; we know this from realizing that the central region of each of the two tori forming our droplet remains bright irrespective of its side view orientation with respect to the incident polarization direction. This is also confirmed when the measurement of T as a function of ϕ_{exit} at a waveguiding region on a double toroid indicates a

non-zero ϕ. As an example, see the plot in figure 4.15(a) where we obtain $\phi \approx 60^\circ$ for a double toroid that composes of two tori of $\xi \approx 3.4$, which is similar to ϕ for a torus of similar ξ (see figure 4.12). In addition, the locations where waveguiding occur are the same on both tori (see the circles in figure 4.15(b) and (c)) suggesting that they share the same twist.

4.4.3 Geometry Variations effects on Defects Locations

Through micro-surgery (see Appendix E), it is possible to control the curvature of certain places on double toroids. Some examples of double toroids with different shape resulting from the modification on some of their curvatures are shown in column (a)-(c) of figure 4.16 with the corresponding viewing plane for each row is shown in column (d). Despite the differences in shape, the defects remain roughly at the same locations for all these double toroids, as indicated in figure 4.16(a1)-(c1). However, upon closer inspection, their placement along the z-axis are all different. For instance, the defects of double toroids that posses a saddle on both sides where the two toroids meet (see figure 4.16(a1)) are located close to the center at $z = 0$. As such, the defects are not visible from the top, as shown figure 4.16(a2), but are clearly seen from the side, as shown in figure 4.16(a3) and (a4). By removing the saddle regions where the two single toroids meet, we get a double toroids in figure 4.16(b1). In this case, both defects drift away from $z = 0$ to $z = a$, which allowing them to be seen simultaneously from the top, as shown in figure 4.16(b2). As a result, when view from the side, we can no longer see the defects at the center, as shown in figure 4.16(b3) and (b4). If we remove only one saddle and then rounded that side while leaving the opposite side with a saddle, we get a double toroids in figure 4.16 instead. For this scenario, we observe that one defect moved to $z = -a$, while another moved to $z = a$ because only one defect is visible when view from the top (see figure 4.16(c2)). This is also confirmed when we review the image from the sides (see figure 4.16(c3) and (c4)). Thus removing both saddle points between the two toroids will force both defects to shift in the same direction along the z-axis, while removing only on saddle point will force defects to shift in the opposite direction along the z-axis. This shift presumably minimizes the elastic free energy, given that the initial location of the defects are in the region where the two single toroids meet.

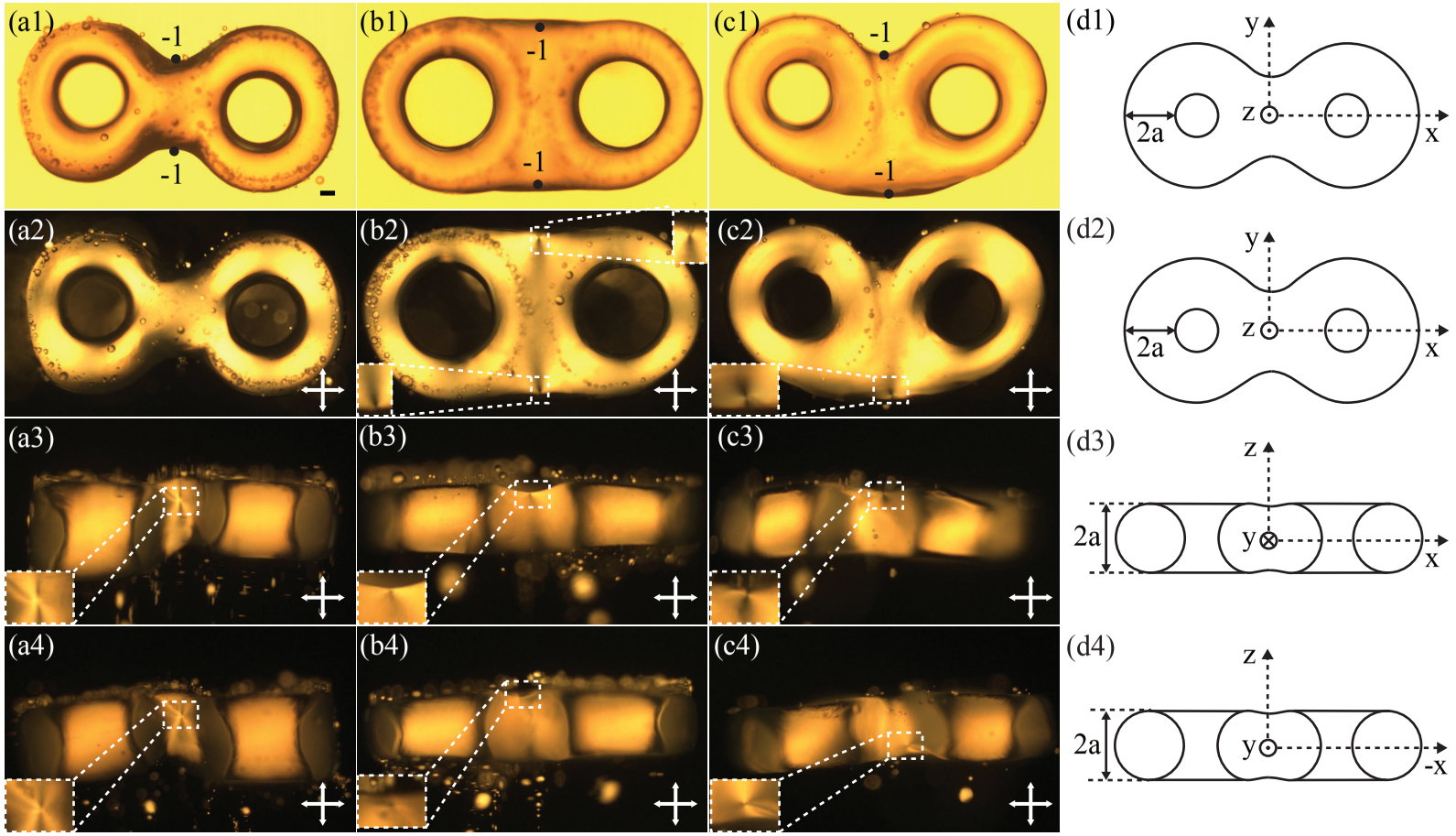

Figure 4.16: (a-c) Top view of a double toroids in bright field. Solid dark circles indicate the location of the two -1 surface defects. (d-f) The same image under cross-polarizers. (g-i) and (j-l) Side view of the double toroids under cross-polarizers when focused at its back from the upper and lower side of (a-c), respectively. The insets are the magnified view of the regions where the topological defect with charge $s = -1$ are located. Scale bar: 100 μm

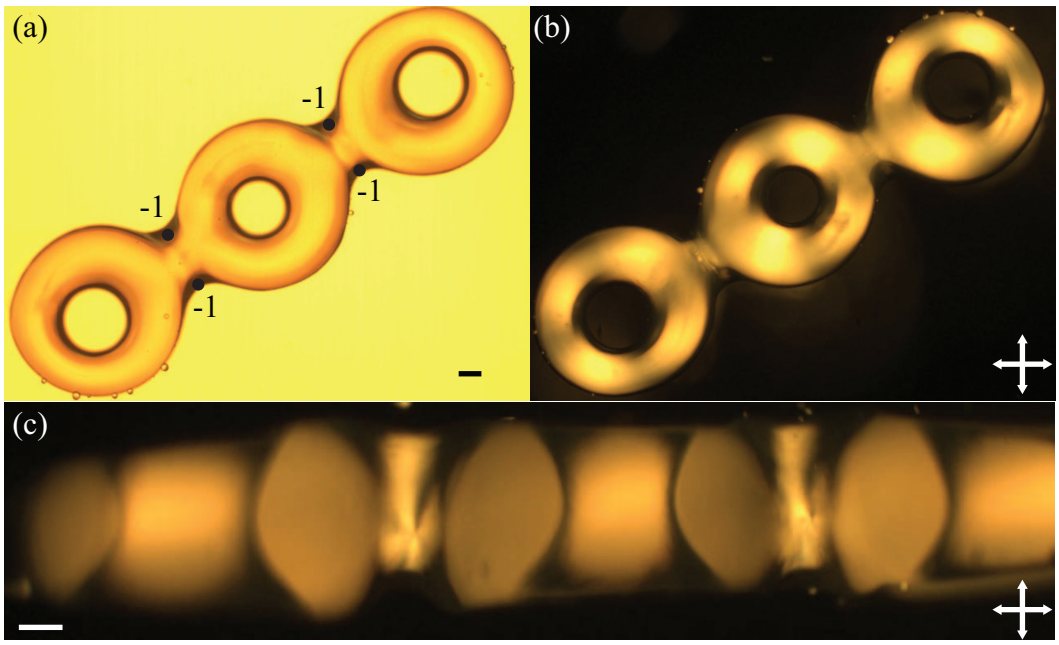

Figure 4.17: (a) Top view image of a triple toroids with a side-by-side arrangement of the handles. (b) The same image under cross-polarizers. (c) Side view of a triple toroids with a side-by-side arrangement of the handles viewed under cross-polarizers. The defects are located in the outer regions where the individual toroids meet. Scale bar: 100 μm

4.5 Nematic Droplet with Three Handles

We can also generate more complex droplets with, for example, three handles aligned along a common axis, as shown by the top view image in figure 4.17(a); the corresponding cross-polarized image is shown in figure 4.17(b), or arranged in a triangle, as shown in figure 4.18(a). In the first case, there are four defects, each of topological surface charge -1, located in the regions where the individual tori meet, as shown when the droplet is viewed along its side between cross-polarizers in figure 4.17(c). In addition, the director is twisted, as expected based on the results for the single and double tori. In contrast, when the handles are arranged in a triangle, there are two -1 defects that cluster together in one of the three regions where the single tori meet, as indicated in figure 4.18(a). In this situation, in addition to the natural frustration imposed by the bounding surface, there is additional frustration arising from the lack of a sufficient number of negative-curvature regions between the single tori to position the defects. There are only three natural regions for the defects to be located and four defects. We find that a possible solution to this problem is to cluster two of the four defects together in one of the three natural regions for them to be located. Figure

4.18(b,c) show the magnified view of the individual defects as view from the side as indicates by the dashed lines in figure 4.18(a). Figure 4.18(d) shows the magnified side view of the remaining area where the two defects are clustered together.

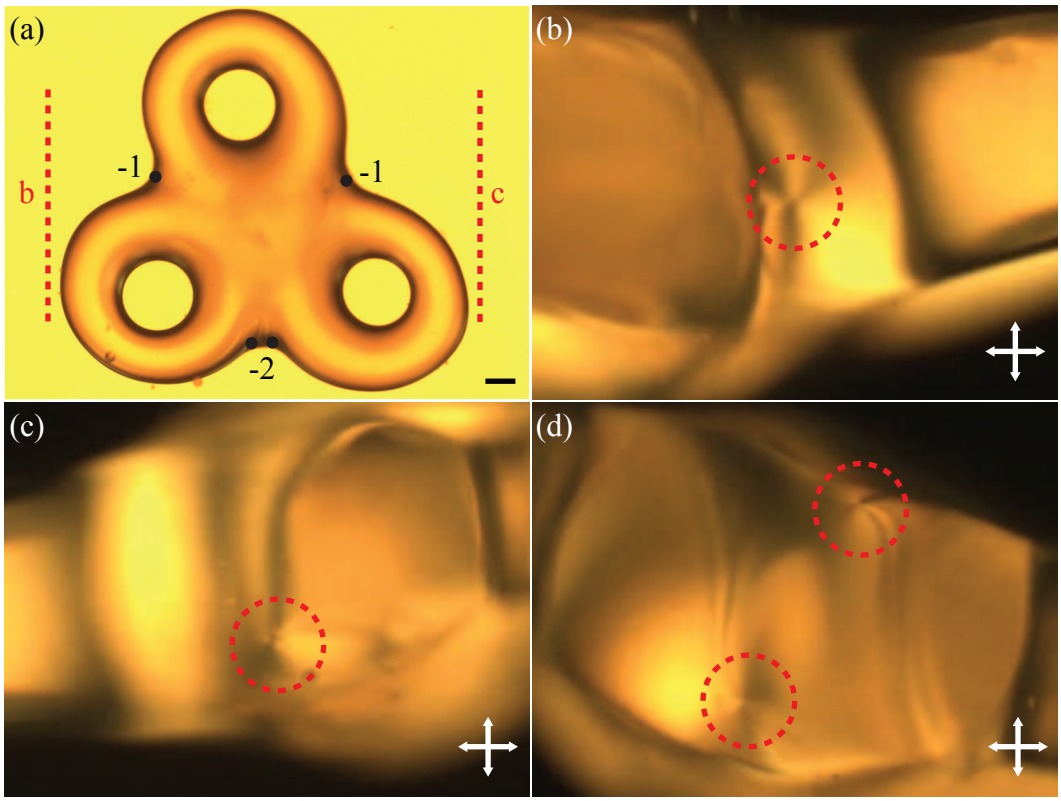

Figure 4.18: (a) Top view image of a triple toroids with a triangular arrangement of the handles. Solid circles show the defect locations found by looking at the droplets between cross-polarizers along different viewing directions (b,c,d). The red circle in (b,c,d) indicate the locations of defects when viewed from the side. Scale bar: 100 μm

4.6 Conclusions

We have generated the first stable nematic droplets with handles using a material with a yield stress as continuous phase to stabilize these otherwise unstable droplets. Nematic toroids have no defects and exhibit a doubly-twisted configuration, similar to that observed in blue phases [104], irrespective of aspect ratio, which in our experiments ranges from $\sim$ 2 to $\sim$ 20; this results from important saddle-splay contributions to the elastic free energy. Interestingly, the comparison of the experimental measurements of the twist angle with our theoretical predictions provides a robust and simple way to measure K_{24}; this is important given the difficulty in determining the value of this elastic

constant with current method [90, 91, 92, 93, 94]. For droplets with additional handles, we observe that there are two -1 surface defects per handle located in regions of $G < 0$ where elastic distortions are minimized.

Our work highlights the role of nematic confinement as a reliable route to induce field configurations with unique geometrical and topological properties. The chiral nematic texture observed in our toroidal droplets closely resembles a Seifert fibration of the 3-spheres, a slightly more general configuration than the celebrated Hopf fibration [105, 106]. Intense experimental effort has been recently directed towards constructing soft structures with non-trivial topological properties using external fields or unique sample preparation. Examples include fluid knots [107], optically created nematic torons [22], hybrid systems composed of nematic dispersions of colloidal particles with various shapes [108, 109] or densely packed filamentous assemblies [23, 110, 111]. Our experiments open up a versatile approach to generate topological soft materials that exploits nematic self-assembly within macroscopic droplets with handles, stabilized using a yield stress material as the outer fluid.

CHAPTER V

CONCLUSIONS

From this Thesis we can extract the following conclusions:

- Toroidal droplets can be generated by injecting a viscous liquid into another rotating imiscible viscous liquid. Our data reveals that we get the formation of toroidal droplet when the capillary number of the outer liquid, $C_o \gtrapprox 2.2R_{tip}/a_{tip}$ with R_{tip} is the distance between the placement of the injected needle and the center of rotation and a_{tip} is radius of the injected needle.

- Toroidal droplets inside a viscous liquid are unstable and will always transform into spherical droplets. They can either break into one or more spherical droplets, if the torus initial tube radius, a_0 is less than its initial inner radius, R_{in}, or it can keep growing fatter until it coalesces onto itself, if the torus initial tube radius, a_0 is greater than its initial inner radius, R_{in}.

- The breakup of thin toroidal droplets is due to Rayleigh-Plateau instabilities analogous to those of cylindrical jet, with an additional requirement that the wavelength of the most unstable mode times an integer number has to equal the overall circumference $2\pi R_0$ of the torus. This condition is often achieved by the shrinking of a torus.

- Inside a Newtonian liquid, toroidal droplets always shrink regardless of their aspect ratio and as a consequence the breaking and shrinking processes happen simultaneously.

- A PIV measurement of the flow field of the shrinking torus suggested that the tube of a torus during the shrinkage grows from the center. In addition, our results reveal that velocity field in the tube cross-section of a torus is significantly influenced by the evolution of the cross-sectional shape.

- A toroidal droplet generated inside a carbopol solution with a finite yield stress is stable against breaking if its thinnest section has a tube radius larger than $a_c = \Gamma/\tau_{y,s}$, where Γ is the

surface tension and $\tau_{y,s}$ is the shearing yield stress, and stable against collapsing if its inner radius is larger than $R_c = \Gamma/\tau_{y,e}$, where $\tau_{y,e}$ is the elongational yield stress. If both conditions are met then a toroidal droplet is stable.

- Similar to instabilities of toroidal droplets in a viscous medium, toroidal droplets in a yield stress medium break only when $a < R_{in}$ and collapse only when $a > R_{in}$. However, unlike toroidal droplets in a viscous medium, the breaking and collapsing of a toroidal droplets in a yield stress medium are decoupled and happen independently.

- In addition, $a_c \approx 1.85R_c$ because the medium surrounding the toroidal droplet is subjected to different kinds of flow depending on the type of instability. The outer medium surrounding the tube near the point of breakup experiences more shear when the torus is breaking, while the outer medium at the center of the torus (in the "donut hole" region) experiences more stretching if the torus is collapsing. Thus, surface tension stress has to overcome the outer medium's shearing yield stress for the torus to break, and it has to overcome the outer medium's elongation yield stress for the torus to collapse. Thus, due to the fact that $\tau_{y,e} = \sqrt{3}\tau_{y,s}$, the expected result for a relationship between the critical tube and inner radii is $a_c = \sqrt{3}R_c$, consistent with our result.

- A broken torus inside of a yield stress material will keep contracting along the length of a torus until the radius of the tip is equal to a_c.

- A toroidal droplet made out of nematic liquid crystal (5CB) with its molecules constrained to planar anchoring at the interface is generally defect free. They do, however, exhibit a double twist configuration for all the observed aspect ratio. The stability of this configuration is due to the contribution from the often-neglected saddle-splay term, which lowers the elastic free energy.

- Nematic configurations on multi-handled toroidal are also doubly-twist with both tori possessing the same twist direction.

- Varying the local curvature of the point where the individual tori meet in a multi-handled droplet generally alters the location where defects are located along the vertical direction

when looking at the torus from the side view.

- Each handle added to a toroidal droplet introduces two more defects of topological charge -1. These defects are located in regions with local saddle geometry to minimize the nematic distortions and hence the corresponding elastic free energy.

- A droplet of more than two handles in a plane, whose centers lie along a straight line, has a pair of -1 defects located at each neck region where the tori meet. In contrast, when the handles are arranged in a triangle, there are three points where the tori meet instead of two. In that case, two meeting points have one -1 defect each, while the third point has two -1 defects clustered together.

APPENDIX A

SURFACE TENSION MEASUREMENT

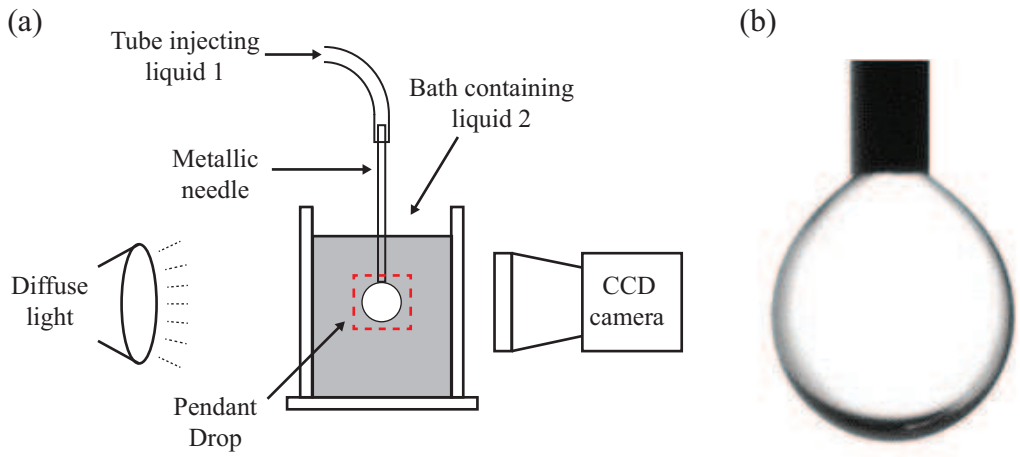

Figure A.1: (a) A schematic of the experiment setup used to photograph a pendant drop. (b) An example picture of a pendant drop taken using this experimental setup. The pendant drop here is glycerol inside 30,000 cps silicone oil.

We use the pendant drop method to measure the interfacial surface tension between two immiscible liquids. The experiment is performed by injecting the first liquid through a metallic needle into a bath of the other liquid. Then the stabilized droplet, while still attached to the needle, is illuminated from behind with diffuse light and its profile is captured using a CCD camera, as shown in figure A.1(a). Figure A.1(b) shows an example of a picture cropped to shows only the pendant drop protruding from the metallic needle captured using this technique. To calculate the surface tension, we first consider the balance between the Laplace pressure change with the change in pressure due to gravity at the apex of the droplet (see figure A.2):

$$\Gamma\left(\frac{1}{R_1}+\frac{1}{R_2}\right)=\frac{2\Gamma}{D}+\delta\rho g z\,, \tag{A.1}$$

where Γ is the surface tension, R_1 is the radius of curvature in the direction parallel to the xz plane, $R_2 = x/\sin\alpha$ is the radius of curvature in the direction perpendicular to the xz plane and about the

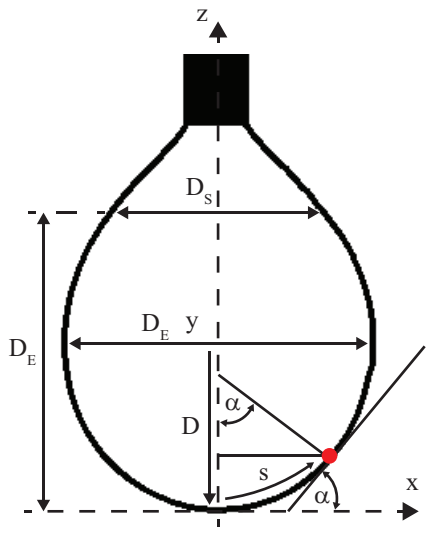

Figure A.2: Geometry of pendant drop.

axis of symmetry of the drop, D is the radius of curvature at the apex of the drop, $\delta\rho$ is the difference between the droplet density and the outer liquid density and $g = 9.81\ m/s^2$ is the gravitational acceleration experienced by the droplet. Assuming that the droplet is symmetric about the z axis, we can denote the coordinate (x, z) in terms of the arc length measured from the apex of the droplet, s, $x = x(s)$ and $z = z(s)$, thus obtaining:

$$\frac{d\alpha}{ds} = \frac{1}{R_1}, \tag{A.2a}$$

$$\frac{dx}{ds} = \cos\alpha, \tag{A.2b}$$

$$\frac{dz}{ds} = \sin\alpha. \tag{A.2c}$$

By replacing $1/R_1$ in equation (A.2a) using equation (A.1), we obtain the following dimensionless differential equations [112]:

$$\frac{d\alpha}{dS} = 2 + \beta Z - \frac{\sin\alpha}{X}, \tag{A.3a}$$

$$\frac{dX}{dS} = \cos\alpha, \tag{A.3b}$$

$$\frac{dZ}{dS} = \sin\alpha. \tag{A.3c}$$

where $\beta = \frac{\Delta\rho g D^2}{\Gamma}$ and the coordinates $S = s/D$, $X = x/D$ and $Z = z/D$ are dimensionless formulation of s, x and z.

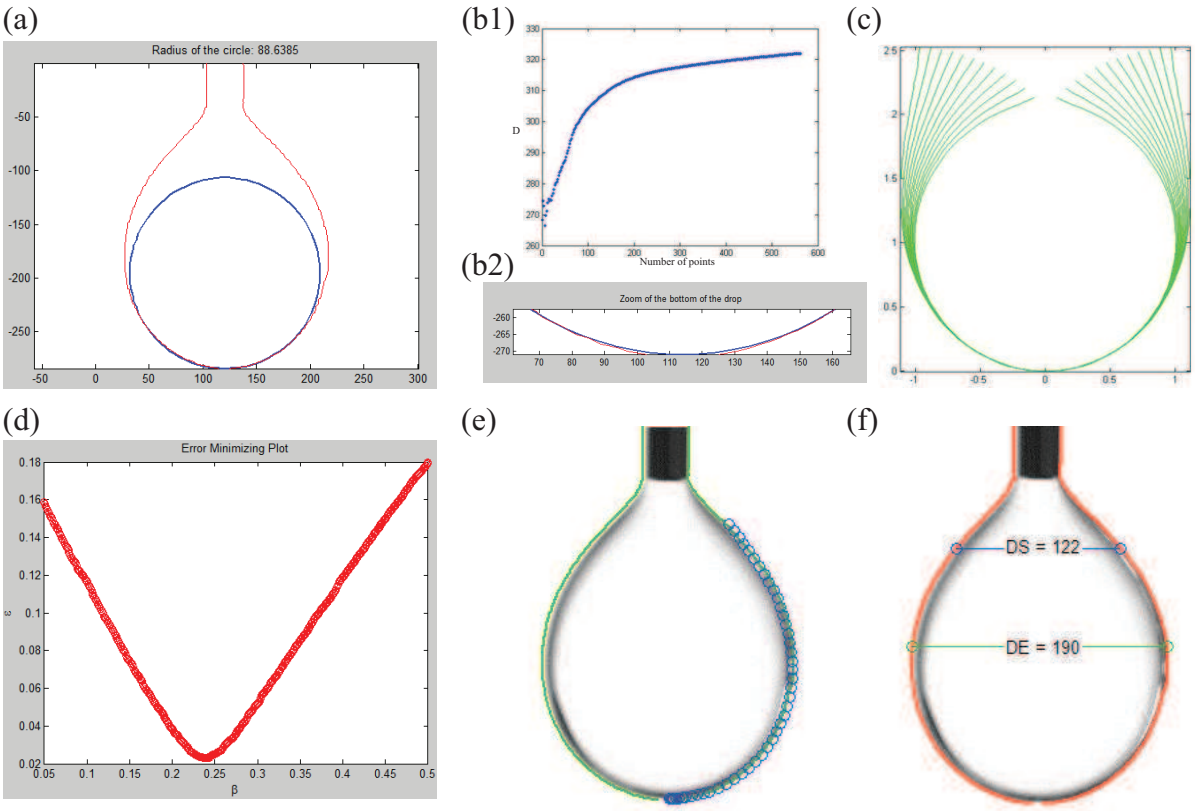

Figure A.3: The pendant drop analysis of a 0.075 wt% carbopol solution in 10 cps silicone oil. (a) A circle with radius equal to the radius of curvature at the drop apex plotted with the contour of the droplet. (b1) A plot of value of D as a function of number of points from the apex as fitted by the circle. (b2) A close-up of the apex of the droplet, where the red line is the actual droplet profile and the blue line is the fitted circle. (c) A plot of theoretical droplet profiles for different values of β normalized by the value of D. (d) A plot of fitting discrepancy ϵ between the theoretical contour calculated for each value of β and the actual contour of the droplet. (e) A comparison between the best-fitted profile (○) and the contour of the droplet (green line). (f) Spatial profile of the droplet showing the maximum diameter, D_e, and the diameter D_s a distance D_e above the drop apex.

To find surface tension, we need to extract D and β from the drop profile. To obtain the value of D we fit a circle to the apex of the droplet profile using an image analysis program developed by Kevin Mohan and Josefa Guerrero (see the acknowledgement), as shown in figure A.3(a). To make sure that we have the circle of best fit, we try to fit the circle to as many points as possible because the radius of a fitted circle depends a lot on the number of points near the apex, provided that only a small number of points is taken. However, the value of D converges to a constant value at a high number of points, as shown in figure A.3(b1). We make sure that circle best fits the profile at the apex of a drop by visually confirming that the magnified droplet profile at the apex

and the overlapping portion of the circle are nicely matched, as shown in figure A.3(b2). To find the value of β, we fit the interface shape by simultaneously solving the differential equations in (A.3), leaving β as a free parameter; note that the droplet shape is varied according to the value of β, as shown in figure A.3(c). We compare the accuracy of the theoretical profile generated using various value of β with the actual droplet contour by plotting the discrepancy (or the corrected sample standard deviation), $\epsilon = \sqrt{\sum(x_\beta - x_{exp})^2/(n-1)}$, against various values of β, where x_β and x_{exp} are the horizontal distance of the droplet interface from the axis of symmetry for the theoretical calculations and the actual drop profile, respectively, as shown in figure A.3(d). The value of β resulting in smallest value of ϵ is chosen. Then we plot the profile of the chosen β together with the actual droplet contour on the actual image to visually confirm that the profile is well-fitted (see figure A.3(e)). From this value of β we obtain the value of surface tension, which we labeled as Γ_1 in the table A.1.

β can also be obtained using a different method, taking advantage of the fact that droplet profiles generated from various values of β possess a unique aspect ratio, $M = D_S/D_E$, where D_E is the maximum diameter on the profile and D_S is the diameter at a distance D_E from the apex. Thus we can generate the equation [113]:

$$\beta = 0.12836 - 0.7577M + 1.7713M^2 - 0.5426M^3\,, \tag{A.4}$$

by polynomial fits the values of M to the value of β, as shown in figure A.3(c). Note that D_E and D_S can be measured directly from the droplet profile, as shown in figure A.3(f). The value of the surface tension obtained using this method is labeled Γ_2 in the table A.1.

Table A.1: Interfacial surface tension between the inner and the outer liquid.

Inner liquid	Outer liquid	Γ_1 (dynes/cm)	Γ_2 (dynes/cm)
60 mM SDS water solution	30000 cps silicone oil	9.6	9.1
glycerol	30000 cps silicone oil	27.0	27.5
0.075% Carbopol solution	10 cps silicone oil	6.4	6.8

APPENDIX B

TOROIDAL DROPLET GENERATION STAGES

A DC motor with gearbox housing was used in the experimental setup to generate a torus in chapter 2 and 3. The gearbox makes it easy for us to control the rotational speed of the rotating stage and helps keeping it constant, since the speed of a small DC motor depends greatly on the viscous drag on the needle. Once the toroidal droplet is formed the viscous drag that the submerged part of metallic need experiences will reduce greatly. Without the gearbox, the stage would end up rotating too fast once the torus is formed, and the experiment will result in a total mess. However, the mechanical coupling of between the gear box and the rotational stage also causes small vibrations, which did not affect the formation of large torus ($\gtrsim$ 1 cm). However, to generate a sub-millimeter size or smaller torus, we needed to eliminate these vibrations. Our idea is to eliminate the mechanical couplings altogether. To achieve this, we use a modified fan motor as our new rotating stage. The fan motor that we use is a shaded-pole induction motor, which is a type of single-phase AC motor. Figure B.1(a) shows the modified motor as viewed from the bottom of the rotational stage; note that the only modification is the enlargement of the hole in the center of the rotor. The synchronous speed (the speed at which the magnetic field rotates) is governed by the equation

$$v_{rpm} = \frac{120f}{p}, \tag{B.1}$$

where v_{rpm} is the synchronous speed in rpm, f is the frequency of applied voltage in hertz, and p is the number of poles in the stator ($p = 6$ for our motor, as shown in figure B.1(a)). Since the number of poles is fixed by the manufacturer, v_{rpm} is determined only by the frequency of the input AC power. Note that the rotor is never able to reach synchronous speed. If it did, there would be no voltage induced in the rotor i.e. no torque would be developed. The difference between rotor speed and synchronous speed is called slip, which is usually less than 5% for this type of motor.

Shaded pole motors get their name from having a continuous copper loop known as the ”shading coil” wound around a small portion of each pole (see figure B.1(b)). This portion of the pole is called

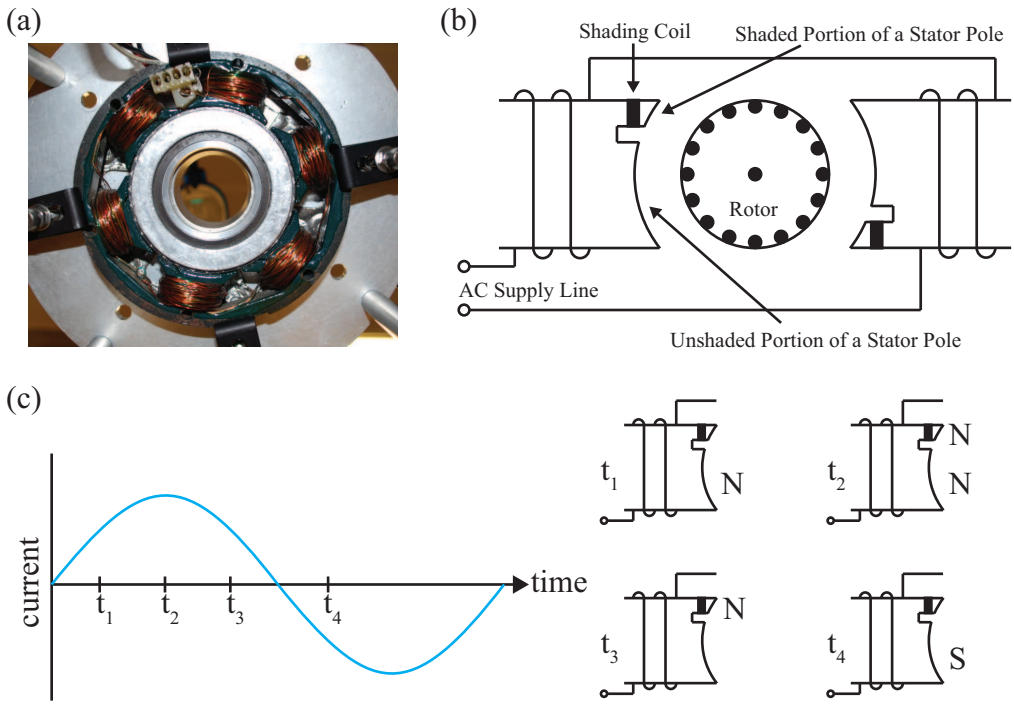

Figure B.1: (a) Magnetic field driven rotating stage as viewed from below. (b) Schematic of 2-pole shaded-pole AC induction motor. (c) Plot of Supply current as a function of time and the corresponding magnetic pole.

the shaded portion while the remainder is called the unshaded portion of a stator pole. The purpose of the shading coil is to causes the magnetic field through the shaded portion to lag behind the field in the unshaded portion. When there is a change in the flux as the current from the AC supply line changes, an e.m.f. (electromagnetic field) is induced in the copper shading band producing its own flux. According to Lenz's law, the direction of the current caused by the e.m.f. is in the direction that will create flux that opposes the original change in flux. Hence there is crowding of flux in unshaded part and weakening of flux in shaded part. This produces a slightly rotating field in each pole face which tends to rotate the rotor from the unshaded to the shaded portion of the pole. For example (see figure B.1(c)): at instant $t = t_1$, when there is a rise in current, the overall magnetic flux is concentrated at the unshaded portion, producing a north magnetic pole there; at instant $t = t_2$, when there is no change in current, the magnetic flux is distributed equally, producing a north magnetic pole in both the unshaded and shaded portions; at instant $t = t_3$, when there is a drop in current, the overall magnetic flux is concentrated at the shaded portion, producing a north magnetic pole there; and at instant $t = t_4$, when there is a rise in current in the opposite direction, the process

repeats itself, but now with the opposite magnetic pole.

APPENDIX C

THEORETICAL ANALYSIS FOR THE BREAKUP OF THIN TORI

C.1 Introduction

In this section we will present the theoretical analysis of the breakup of thin toroidal droplets using the calculations by Yao and Bowick [34, 50] based on the conservation of energy. The perturbation on the surface of the toroidal droplet, $\epsilon_k(t)$ (note that the index $k = 2\pi/\lambda$, where λ is the wavelength associated to mode of instability), grows as $e^{\sigma t}$ based on a linearized stability analysis. Thus, the growth rate σ can be written as $\dot{\epsilon}_k(t)/\epsilon_k(t)$. In order to find this ratio we must solve for the rate of change of the surface energy and the viscous dissipation rate since they are proportional to $\epsilon_k(t)\dot{\epsilon}_k(t)$ and $\epsilon_k(t)^2$ respectively.

C.2 The Rate of Change of Surface Free Energy

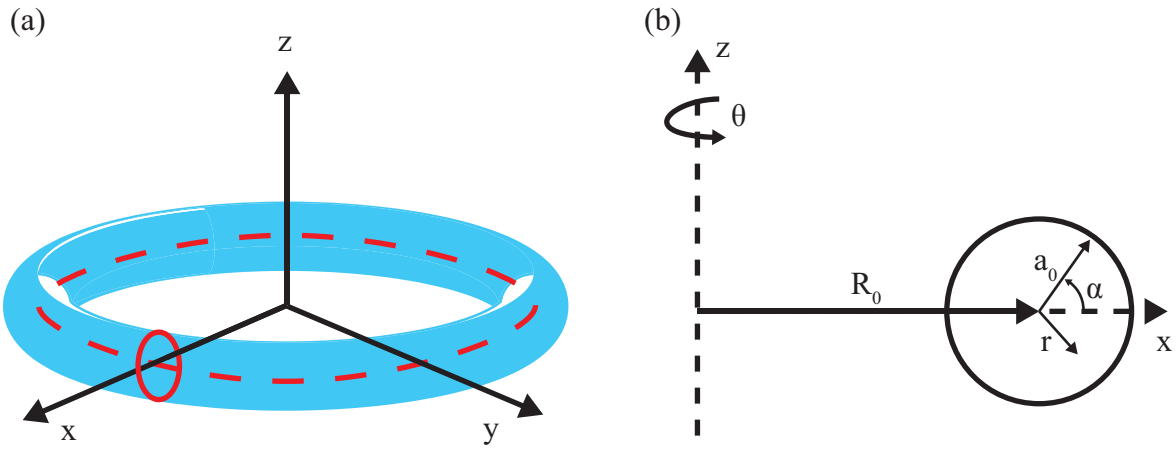

Figure C.1: Azimuthal toroidal coordinates: (a) 3D schematic of the torus, and (b) the cross-section of the tube as indicated in (a).

In order to solve for σ, we first need to solve for the rate of change in the surface free energy

$\Delta\dot{F}$, which is equal to

$$\Delta F = \Gamma \Delta \dot{A} \,. \tag{C.1}$$

Thus, since the surface tension Γ is constant, we only need to solve for the change in the interfacial area between the perturbed and the unperturbed toroidal droplet in order to solve for the change in surface energy.

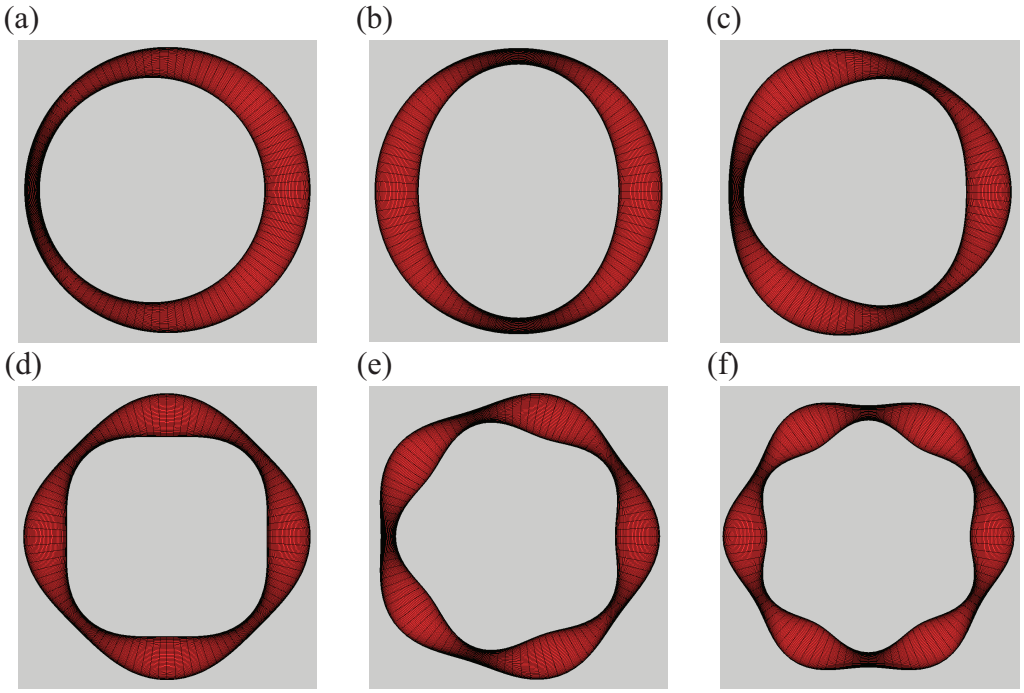

Figure C.2: Plots of tori with a perturbed tube radius ($\epsilon_k = a_0/3$): (a) $n = 1$, (b) $n = 2$, (c) $n = 3$, (d) $n = 4$, (e) $n = 5$, (b) $n = 6$.

To solve for the change in surface area of toroidal droplet due to a perturbation, we will use another toroidal coordinates defined as

$$\vec{x} = \begin{pmatrix} (R_0 + r\cos\alpha)\cos\theta \\ (R_0 + r\cos\alpha)\sin\theta \\ r\sin\alpha \end{pmatrix}, \tag{C.2}$$

where α, θ and r are coordinates shown in figure C.1(b). Under the coordinates (C.2), we can write

the corresponding metric tensor as:

$$\mathbf{g} = \begin{bmatrix} r^2 & 0 & 0 \\ 0 & (R_0 + r\cos\alpha)^2 & 0 \\ 0 & 0 & 1 \end{bmatrix}, \tag{C.3}$$

where each component $g_{ij} = \sum_{k}^{3} \frac{\partial x_k}{\partial u_i}\frac{\partial x_k}{\partial u_j}$ with $u_1 = \alpha$, $u_2 = \theta$ and $u_3 = r$. Then, the area of the torus in terms of this metric tensor is

$$A = \int \sqrt{|\mathbf{g}|} d\alpha d\theta \,, \tag{C.4a}$$

(C.4b)

where $|\mathbf{g}|$ is the determinant of $\mathbf{g}$. For a torus with a small perturbation amplitude ϵ_k, the perturbed tube radius can be written as

$$a(\theta) = a_0 + \epsilon_k \cos(n\theta) \,, \tag{C.5}$$

where $n = kR_0$ is the number of wavelength of perturbation (see figure C.2 for toroidal surface plotted with the tube radius from equation (C.5) with different n). By replacing r in the coordinates from equation (C.2) with the perturbed tube radius from equation (C.5), we can expanded $\mathbf{g}$, assuming small perturbation $\epsilon_k << a_0$, using a Taylor series

$$\mathbf{g}(\epsilon_k) = \mathbf{g}(\epsilon_k = 0) + \epsilon_k \frac{d\mathbf{g}}{d\epsilon_k}\bigg|_{\epsilon_k=0} + \epsilon_k^2 \frac{1}{2}\frac{d^2\mathbf{g}}{d\epsilon_k^2}\bigg|_{\epsilon_k=0} + \dots \,, \tag{C.6}$$

By inserting (C.6) into equation (C.4a) and integrating, we get the area of the perturbed torus upto the second order of ϵ_k as

$$A_{perturbed} = 4\pi^2 a_0 R_0 + \epsilon_k^2 \left(-1 + \frac{k^2 a_0 R_0}{\sqrt{(R_0/a_0)^2 - 1}} \right) \frac{\pi R_0}{a_0} \,. \tag{C.7}$$

Note that the first term on the R.H.S. of equation (C.7) is the area of an unperturbed torus, A_0. In the thin torus limit, $R_0 >> a_0$, $A_{perturbed} < A_0$ provided that $(ka_0)^2 - 1 < 0$ or $2\pi a_0 < 2\pi R_0$, which is the Rayleigh-Plateau criterion; the system will favor instability if the wavelength of instability is greater than the circumference of the thread, since smaller surface area is preferred. Then, the change in surface energy given in equation (C.1) becomes

$$\Delta F = \Gamma \epsilon_k^2 \left(-1 + \frac{k^2 a_0 R_0}{\sqrt{(R_0/a_0)^2 - 1}} \right) \frac{\pi R_0}{a_0} \,. \tag{C.8}$$

From the time derivative of equation (C.8), we obtain the rate of change of surface energy

$$\Delta\dot{F}_\Gamma = 2\Gamma\dot{\epsilon}_k(t)\epsilon_k(t)\left(-1 + \frac{k^2 a_0 R_0}{\sqrt{(R_0/a_0)^2 - 1}}\right)\frac{\pi R_0}{a_0}\,. \tag{C.9}$$

which is proportional to $\dot{\epsilon}_k(t)\epsilon_k(t)$, Γ and R_0/a_0.

C.3 The Rate of Viscous Dissipation

The rate of work for shape change with constant volume can generally be written as

$$\dot{E}_{visc} = \int_V dV' \mathbf{T} : \vec{\nabla}\vec{v}, \tag{C.10}$$

where $\mathbf{T}$ is the viscous stress tensor and $\vec{v}$ is the velocity of the fluid element. The ij^{th} component of $\mathbf{T}$ is defined as

$$T_{ij} = \eta(\partial_i v_j + \partial_j v_i)\,. \tag{C.11}$$

From equations $C.10$ and $C.11$ we can see that $\dot{E}_{visc}$ depends only on the viscosity and the velocity field, so we need to solve for $\vec{v}$ to get the shear dissipation rate. To do this we need to solve the Navier-Stokes equation:

$$\rho(\partial_t\vec{v} + \vec{v}\cdot\vec{\nabla}\vec{v}) = -\vec{\nabla}p + \eta\Delta\vec{v}, \tag{C.12}$$

where ρ is the fluid density and p is pressure. In our experiments, the Ohnesorge number is large, $Oh \equiv \sqrt{\eta_o^2/\rho a_0\Gamma} \sim O\left(10^3\right)$. As a result, the viscous timescale, $t_v \sim \eta_o a_0/\Gamma$, dominates over the diffusion timescale, $t_d \sim \rho a_0^2/\eta_o$, and the convection timescale, $t_c \sim \sqrt{\rho a_0^3/\Gamma}$. Note that $t_d << t_v$ means that the velocity field in bulk fluids can respond to the interface dynamics almost instantaneously, so we can ignore the inertial term $\rho\partial_t\vec{v}$. Likewise, $t_c << t_v$ means that the timescale for the interface to be substantially deformed in an *inviscid* liquid is insignificant, and thus we can also ignore the convection term $\rho\vec{v}\cdot\vec{\nabla}\vec{v}$. Therefore, we can simplify the Navier-Stokes equation into the Stokes equation:

$$0 = -\vec{\nabla}p + \eta\Delta\vec{v}. \tag{C.13}$$

For an incompressible fluid, $\vec{\nabla}\cdot\vec{v} = 0$ and hence there exists a vector potential $\vec{\psi}$ such that $\vec{v} = \vec{\nabla}\times\vec{\psi}$. Note that there are indefinitely many choices for $\vec{\psi}$, but we can fix a particular $\vec{\psi}$ by

applying a particular gauge choice. We use the transverse (or Coulomb) gauge, $\vec{\nabla} \cdot \vec{\psi} = 0$. By further taking the curl on both sides of equation (C.13) and replacing $\vec{v}$ with $\vec{\nabla} \times \vec{\psi}$, we obtain the bi-harmonic equation

$$\Delta^2 \vec{\psi} = 0\,. \tag{C.14}$$

In the limit of a very thin torus, $\xi \to \infty$, we can locally treat the interface as cylindrical. Hence the perturbed interface of the two fluids follows as

$$a(z,t) = a_0 + \epsilon(z,t)\,, \tag{C.15}$$

where $\epsilon(z,t) = \sum_{k=1}^{\infty} \epsilon_k(t) e^{ikz}$. The velocity and pressure also depend on z in the same way: $\vec{v}(z,t) = \vec{v}(t)\exp^{ikz}$ and $p(z,t) = p_0 + p(t)\exp^{ikz}$. In cylindrical coordinates,

$$v_r = \frac{1}{r}\partial_z \psi\,, \tag{C.16a}$$

$$v_z = \frac{-1}{r}\partial_r \psi\,, \tag{C.16b}$$

where $v_\alpha = 0$ due to axial symmetry of the cylinder, and

$$\vec{\psi} = \frac{-\psi(r)}{r} e^{ikz} \hat{e}_\theta\,, \tag{C.17}$$

where $\psi(r)$ is the stream function. Introducing new operator $D \equiv \partial_r^2 - k^2 - \frac{1}{r}\partial_r$ and using equation (C.17), equation (C.14) can be rewritten in terms of stream function as:

$$D^2 \psi(r) = 0\,. \tag{C.18}$$

By choosing $\psi(r) = r f(r)$, equation (C.18) becomes:

$$r^2 \partial_r^2 f(r) + r \partial_r f(r) - (1 + k^2 r^2) f(r) = 0\,, \tag{C.19}$$

which is a modified Bessel equation of order one. Its solution is the linear combination of the modified Bessel function of the first kind of order one, $I_1(kr)$, and of the second kind of order one, $K_1(kr)$. Note that the modified Bessel functions has recurrence relations:

$$\partial_x I_n(x) = \frac{n}{x} I_n(x) + I_{n+1}(x)\,, \tag{C.20a}$$

$$I_n(x) = \frac{2n+1}{x} I_{n+1}(x) + I_{n+2}(x)\,. \tag{C.20b}$$

This relation is the same for K_n. By defining $x \equiv kr$, D becomes $D = k^2(\partial_x^2 - \frac{1}{x}\partial_x - 1)$. For a trial solution $\psi = x^n I_n(x)$, we get:

$$D\psi = k^2((2n-1)I_{n-1}(x) - \frac{2n}{x}I_n(x) - I_{n+1}(x)\,. \tag{C.21}$$

We can obtain $D^2\psi$ as a function of x and I_n by re-applying $k^2(\partial_x^2 - \frac{1}{x}\partial_x - 1)$ to equation (C.21). Finally, we get $D\psi = 0$ for $n = 1$ and $D^2\psi = 0$ for $n = 2$. We can use a similar trial for $x^n K_n(x)$, and hence the solution to the bi-harmonic equation is:

$$\psi(x) = c_1 x I_1(x) + c_2 x K_1(x) + c_3 x^2 I_2(x) + c_4 x^2 K_2(x)\,, \tag{C.22}$$

where c_1, c_2, c_3 and c_4 are the constants of integration. The flow field vorticity, $\vec{\Omega}$, is zero when $D\psi(r) = 0$, since $\vec{\Omega} \equiv \vec{\nabla} \times \vec{v} = \frac{1}{r}D\psi(r)e^{ikz}\hat{e}_\theta$. Therefore the first 2 terms in equation (C.22) represent the irrotational solutions, for which $\vec{\Omega} = 0$, and the last 2 terms represent the rotational solutions, for which $\vec{\Omega} \neq 0$. To obtain the four coefficients c_1, c_2, c_3 and c_4, we use the following boundary conditions:

$$v_r(r = a_0^+) = v_r(r = a_0^-) = \dot{u}(z,t)\,, \tag{C.23a}$$

$$v_z(r = a_0^+) = v_z(r = a_0^-)\,, \tag{C.23b}$$

$$\vec{v}(r = \infty) = 0\,, \tag{C.23c}$$

$$v_r(r = 0) = 0\,, \tag{C.23d}$$

$$\tau_{rz}(r = a_0^+) = \tau_{rz}(r = a_0^-)\,. \tag{C.23e}$$

Equation (*C.23a*) follows from the assumption that the fluid particles at the liquid-liquid interface move together with the surface. Equation (*C.23b*) is the non-slip boundary condition for v_z at the interface. Equation (*C.23c*) results from assuming that the outer fluid does not move at locations sufficiently far away from the toroidal drop. Equation (*C.23d*) results from the polar symmetry of the toroidal drop and equation (*C.23e*) enforces the continuity of the tangential stress across the liquid-liquid interface.

Based on the boundary conditions *C.23c* and *C.23d*, ψ/r has to vanish at $r \to \infty$ and be finite at

$r = 0$. Therefore, for the inside and outside fluids:

$$\psi_{in} = c_1 x I_1(x) + c_3 x^2 I_2(x)\,, \tag{C.24a}$$

$$\psi_{out} = c_2 x K_1(x) + c_4 x^2 K_2(x)\,. \tag{C.24b}$$

From these equations, we can obtain the velocity field for the inside fluid,

$$v_r(r; c_1, c_3) = ik^2(c_1 I_1(kr) + c_3 kr I_2(kr))\,, \tag{C.25a}$$

$$v_z(r; c_1, c_3) = -k^2(c_1 I_0(kr) + c_3 kr I_1(kr))\,, \tag{C.25b}$$

and for the outside fluid,

$$v_r(r; c_2, c_4) = ik^2(c_2 K_1(kr) + c_4 kr K_2(kr))\,, \tag{C.26a}$$

$$v_z(r; c_2, c_4) = -k^2(c_2 K_0(kr) + c_4 kr K_1(kr))\,. \tag{C.26b}$$

In addition, from equation *C*.11, we obtain the tangential stress of the inside fluid,

$$\tau_{rz}(r; c_1, c_3) = 2\eta_i k^3(-c_3 kr I_0(kr) + (c_3 - c_1) I_1(kr))\,, \tag{C.27}$$

and of the outside fluid,

$$\tau_{rz}(r; c_2, c_4) = -2\eta_o k^3(c_4 kr K_0(kr) + (c_2 + c_4) K_1(kr))\,. \tag{C.28}$$

From the boundary equations *C*.23*a*, *C*.23*b* and *C*.23*e*, we can construct the linear equation $\mathbf{A}x = \mathbf{B}$, where

$$\mathbf{A} = \begin{bmatrix} I_1(ka_0) & 0 & ka_0 I_2(ka_0) & 0 \\ 0 & K_1(ka_0) & 0 & ka_0 K_2(ka_0) \\ I_0(ka_0) & -K_0(ka_0) & ka_0 I_1(ka_0) & -ka_0 K_1(ka_0) \\ -2\eta_i(ka_0)^3 I_1(ka_0) & 2\eta_o(ka_0)^3 K_1(ka_0) & -3\eta_i(ka_0)^3(ka_0 I_0(ka_0) - I_1(ka_0)) & 2\eta_o(ka_0)^3(ka_0 K_0(ka_0) + K_1(ka_0)) \end{bmatrix},$$

$x = (c_1 \quad c_2 \quad c_3 \quad c_4)^{-1}$ and $\mathbf{B} = (\frac{\dot{u}_k}{ik^2} \quad \frac{\dot{u}_k}{ik^2} \quad 0 \quad 0)^{-1}$. By solving for $x = \mathbf{A}^{-1}\mathbf{B}$, where $\mathbf{A}^{-1}\mathbf{A} = \mathbb{1}$,

we get the coefficients c_1, c_2, c_3 and c_4 as

$$c_1 = \frac{N_1(k)}{D(k)}\,, \tag{C.29a}$$

$$c_2 = \frac{N_2(k)}{D(k)}\,, \tag{C.29b}$$

$$c_3 = \frac{N_3(k)}{D(k)}\,, \tag{C.29c}$$

$$c_4 = \frac{N_4(k)}{D(k)}\,. \tag{C.29d}$$

where

$\frac{N_1(k)}{-ik\dot{u}_k} = [ka_0(\kappa-1a_0)I_0(ka_0)-(\kappa-2)I_1(ka_0)]K_0^2(ka_0)+[ka_0(2\kappa-1)I_0(ka_0)+2(1-\kappa)I_1(ka_0)]K_1(ka_0)+$
$ka_0(\kappa-1)[-ka_0I_0(ka_0)+I_1(ka_0)]K_1^2(ka_0)$,

$\frac{N_2(k)}{-ika_0\dot{u}_k} = ka_0(\kappa-1)I_1^2(ka_0)(ka_0K_0(ka_0)+K_1(ka_0))+I_0(ka_0)I_1(ka_0)[ka_0(\kappa-2)K_0(ka_0)+2(\kappa-$
$1)K_1(ka_0)]+ka_0I_0^2(ka_0)[ka_0(1-\kappa)K_0(ka_0)+(1+2\kappa)K_1(ka_0)]$,

$\frac{N_3(k)}{i\dot{u}_k} = I_0(ka_0)K_1(ka_0)^2+I_1(ka_0)[ka_0(\kappa-1)K_0(ka_0)^2+(2\kappa-1)K_0(ka_0)K_1(ka_0)+ka_0(1-\kappa)K_1(ka_0)^2]$,

$\frac{N_4(k)}{-ika_0\dot{u}_k} = (\kappa-1)I_0(ka_0)^2K_1(ka_0)-(\kappa-2)I_0(ka_0)K_1(ka_0)+I_1^2(ka_0)[\kappa K_0(ka_0)+ka_0(1-\kappa)K_1(ka_0)]$,
and

$\frac{D(k)}{(ka_0)^2} = -ka_0I_0^2(ka_0)K_1^2(ka_0)+2I_0(ka_0)I_1(ka_0)K_1^2(ka_0)+I_1^2(ka_0)[\kappa ka_0K_0^2(ka_0)+2\kappa K_0(ka_0)K_1(ka_0)+$
$ka_0(1-\kappa)K_1^2(ka_0)]$.

The dissipation rate, $\dot{E}_{vis}$, for the inside and the outside liquids can now be calculated using equation *C*.10. By inserting equations *C*.25 and *C*.27 into equation *C*.10 and integrating only with respect to r and α, we obtain for the viscous dissipation rate per unit length inside fluid

$$\dot{E}_{visc} = -\eta_i V_i(k)\,, \tag{C.30}$$

where

$\frac{V_i(k)}{\pi(ka_0)^4} = 2c_3(c_3-c_1)(ka_0)^2I_0^2(ka_0)-2ka_0[c_1^2-3c_1c_3+c_3^2(3+(ka_0)^2)]I_0(ka_0)I_1(ka_0)+[(c_1-2c_3)^2+$
$c_3(ka_0)^2(-2c_1+3c_3)]I_1^2(ka_0)$. The viscous dissipation rate of the outside fluid, $V_o(k)$, can be obtained in a similar way. From the expression of the coefficients c_1, c_2, c_3 and c_4, we can see that $V_i(k)$ depends on the viscosity ratio, κ. Furthermore, since the coefficients c_1, c_2, c_3 and c_4 are proportional to $\dot{u}_k$, $\dot{E}_{visc} \propto \dot{u}_k^2$ as previously stated.

C.4 Growth Rate Calculation via Energy Conservation

The calculation for the growth rate σ is very simple now that we have obtained $\Delta\dot{E}_\Gamma$ and $\dot{E}_{visc}$, since, from energy conservation, the change in surface energy due to the evolution of the toroidal droplet must balance the change in kinetic energy and the heat exchange with the surroundings due to viscous dissipation. For Stokes flow, we can choose to ignore the change in kinetic energy since it is insignificant compared to the amount of viscous dissipation. Thus, by equating $\Delta\dot{E}_\Gamma$ to $\dot{E}_{visc}$, we obtain the growth rate associated with a wavenumber k:

$$\sigma_k = \frac{\Gamma S(k)}{\eta_i V_i(k) + \eta_o V_o(k)}, \tag{C.31}$$

where $S(k) = \left(-1 + \frac{k^2 a_0 R_0}{\sqrt{\xi^2-1}}\right)\pi\xi$.

In the limit $\kappa \to 0$, this equation becomes:

$$\sigma_k = \frac{\Gamma}{\eta_o} \frac{\left(1 - \frac{(ka_0)^2 R_0}{a_0\sqrt{\xi^2-1}}\right)}{2\left[1 + (ka_0)^2 - (ka_0)^2\left(\frac{K_0(ka_0)}{K_1(ka_0)}\right)^2\right]}, \tag{C.32}$$

which exactly coincides with that obtained by Tomotika [43]. Therefore, in this limit, it is valid to compare our experimental results with the Tomotika's results. For larger k, our experiments suggest that this is still correct.

APPENDIX D

DERIVATION OF HERSCHEL-BULKLEY MODEL IN GENERALIZED TENSOR FORM

Note that the equation (3.1) is only applicable to a 2-dimensional shear flow. However, the collapsing of the toroidal droplet is caused by the 3-dimensional elongational flow of the yield stress material of the inner region of the torus. Thus, to find the values of τ_{ye} and τ_{ys}, we solve for elongational and shear flow of equation viscoelastic fluid using the Herschel-Bulkley model in tensor notation. First we introduce the stress, $\mathbf{T}$, and strain rate, $2\mathbf{D}$, tensor:

$$\mathbf{T} = \begin{bmatrix} T_{xx} & T_{xy} & T_{xz} \\ T_{yx} & T_{yy} & T_{yz} \\ T_{zx} & T_{zy} & T_{zz} \end{bmatrix}, \tag{D.1}$$

$$2\mathbf{D} = \mathbf{2}\begin{bmatrix} D_{xx} & D_{xy} & D_{xz} \\ D_{yx} & D_{yy} & D_{yz} \\ D_{zx} & D_{zy} & D_{zz} \end{bmatrix}. \tag{D.2}$$

where $D_{ij} = \frac{1}{2}\left(\frac{\partial v_i}{\partial x_j} + \frac{\partial v_j}{\partial x_i}\right)$. From the definition of D_{ij}, we can see that $2\mathbf{D}$ is a symmetric matrix. We can solve for its eigenvalues by solving:

$$|2\mathbf{D} - \dot{\gamma}\mathbf{I}| = 0\,. \tag{D.3}$$

Expanding equation (D.3) yields

$$\dot{\gamma}^3 - I_{2D}\dot{\gamma}^2 + II_{2D}\dot{\gamma} - III_{2D} = 0\,, \tag{D.4}$$

where the coefficients are

$$I_{2D} = D_{11} + D_{22} + D_{33}\,, \tag{D.5a}$$

$$II_{2D} = D_{11}D_{22} + D_{22}D_{33} + D_{33}D_{11} - (D_{12}D_{21} + D_{23}D_{32} + D_{31}D_{13})\,, \tag{D.5b}$$

$$III_{2D} = D_{11}D_{22}D_{33} + D_{12}D_{23}D_{31} + D_{13}D_{32}D_{21} - (D_{11}D_{23}D_{32} + D_{21}D_{12}D_{33} + D_{31}D_{22}D_{13})\,. \tag{D.5c}$$

$I_{2D} = tr2\mathbf{D}$ is the first invariant of the tensor $2\mathbf{D}$, $II_{2D} = \frac{1}{2}[I_{2D}^2 - tr(2\mathbf{D})^2]$ is the second invariant and $III_{2D} = det2\mathbf{D}$ is the third invariant. Note that these coefficients are called invariant because they retain the same values no matter what coordinate system $2\mathbf{D}$ is in because the eigenvalues of $2\mathbf{D}$ have to always be the same. We can also define them as the following:

$$I_{2D} = \dot{\gamma}_1 + \dot{\gamma}_2 + \dot{\gamma}_3\,, \tag{D.6a}$$

$$II_{2D} = \dot{\gamma}_1\dot{\gamma}_2 + \dot{\gamma}_2\dot{\gamma}_3 + \dot{\gamma}_3\dot{\gamma}_1\,, \tag{D.6b}$$

$$III_{2D} = \dot{\gamma}_1\dot{\gamma}_2\dot{\gamma}_3\,, \tag{D.6c}$$

where $\dot{\gamma}_i$ is the strain rate in the principal direction x_i. The physical interpretation of the invariants depends on the type of the tensor. For the strain rate tensor, it is well known that the time derivative of an infinitesimal volume per unit volume is equal to the first invariant:

$$\lim_{V\to 0} \frac{1}{V}\frac{dV}{dt} = \nabla\cdot\vec{v} = I_{2D}\,, \tag{D.7}$$

where $V = xyz$ and $\vec{v}$ is the fluid's velocity. Dishington [79] has given the physical interpretation for the second invariant and third invariant of the strain rate tensor. He finds that taking the second time derivative of an infinitesimal volume per unit volume gives the following relation:

$$\lim_{V\to 0} \frac{1}{V}\frac{d^2V}{dt^2} = \nabla\cdot\vec{a} + 2II_{2D}\,, \tag{D.8}$$

provided that x, y and z axis are along the principal axes. The first and second term on the R.H.S. of equation (D.8) represent the second time derivative of an infinitesimal volume per unit volume caused by dilatation and deformation of the surface of that fluid element, respectively. Applying the same method to the third time derivative, he shows that $6III_{2D}$ is equivalent to the second term in equation (D.8). This indicates that even in the absence of acceleration and jerk, a constant strain rate will still create a non-zero second and third time derivative of the volume.

In a Newtonian liquid, stress is linearly proportional to the strain rate. The generalized Newtonian liquid model proposes that stress depends only on the rate of deformation

$$\mathbf{T} = f(2\mathbf{D})\,. \tag{D.9}$$

By expanding the above equation in a power series, we get

$$\mathbf{T} = f_0\mathbf{D}^0 + f_1\mathbf{D}^1 + f_2\mathbf{D}^2 + f_3\mathbf{D}^3 + \ldots\,, \tag{D.10}$$

where $\mathbf{D}^0 = \mathbf{I}$ and f_0 corresponds to pressure $-p$ for an incompressible fluid. The Cayley-Hamilton theorem [80] states that we can write

$$(2\mathbf{D})^3 - I_{2D}(2\mathbf{D})^2 + II_{2D}2\mathbf{D} - III_{2D}\mathbf{I} = 0\,, \tag{D.11}$$

provided that $2\mathbf{D}$ satisfies its own characteristic equation (D.4). Similarly, for $(2\mathbf{D})^4$ and higher powers, we can just multiply equation (D.11) with the appropriate lower power of $\mathbf{D}$ and then express the result in terms of that lower power and the invariants of $2\mathbf{D}$. We can then simplify the equation (D.10) to

$$\mathbf{T} = -p\mathbf{I} + \eta_1 2\mathbf{D} + \eta_2(2\mathbf{D})^2\,, \tag{D.12}$$

where η_1 and η_2 are both functions of II_{2D} and III_{2D} only (since for an incompressible fluid $I_{2D} = \nabla\cdot\vec{v} = 0$). This equation described what is known as a Reiner-Rivlin fluid [81]. We can discard the term η_2 because it give rise to a non-zero normal stresses ($T_{xx} - T_{yy}$) in steady shear flow ($2D_{xy} = 2D_{yx} = \dot{\gamma}$), which qualitatively disagrees with the experimental observation [82]. We will also discard the pressure term, since in rheological work the pressure term is usually irrelevant, giving us the general liquid equation

$$\mathbf{T} = \eta_1(II_{2D}, III_{2D})2\mathbf{D}\,. \tag{D.13}$$

Equation (D.13) can be adapted to any fluid model. The Newtonian model is a special case, where $\eta_1(II_{2D}, III_{2D})$ has a constant value, η. We will follow [82] for the construction of the Herschel-Bulkley model in terms of the tensor notation

$$\mathbf{T} = \left[\frac{\tau_y}{|II_{2D}|^{1/2}} + m|II_{2D}|^{(n-1)/2}\right]2\mathbf{D}\,, \tag{D.14}$$

which is almost as simple as replacing the τ and $\dot{\gamma}$ in equation (3.1) with $\mathbf{T}$ and $2\mathbf{D}$, respectively, with $|II_{2D}|^{1/2}$ the magnitude of the effective strain rate due to the deformation of the fluid volume. Here the III_{2D} contribution is ignored. Equation (D.14) is not a universal model since it fails to capture the flow behavior of other yield stress materials such elongation of a water-in-oil emulsion [77], mayonnaise, ketchup and bentonite [75]. The discrepancy between the theoretical and experimental results in those cases may have been due to the fact that equation (D.14) should also include a term depending on III_{2D} as suggested by [77]:

$$\mathbf{T} = \left[\frac{\tau_y}{|II_{2D}|^{1/2} + k_1 |III_{2D}/2|^{1/3}} + m \left(|II_{2D}|^{1/2} + k_2 |III_{2D}/2|^{1/3} \right)^{n-1} \right] 2\mathbf{D}\,, \tag{D.15}$$

If $k_1 = k_2 = 0$ then the contribution of III_{2D} is ignored and equation (D.15) reduces to equation (D.14). We chose equation (D.14) to describe our experiment because it consistently describes the experimental flow results of carbopol solutions [83, 75].

APPENDIX E

MICROSURGERY

In chapter 3, we show that a stable torus made inside a yield stress material can be deformed with an external perturbation. This property allows us to join a number of toroidal droplets generated side by side together, thus creating a droplet with multiple handles. For toroidal droplets of dimension $\sim$ 1 cm or above, we can simply join them by removing the material between the droplets with a pipette. However, we need to refine this process if we need to join sub-millimeter size tori.

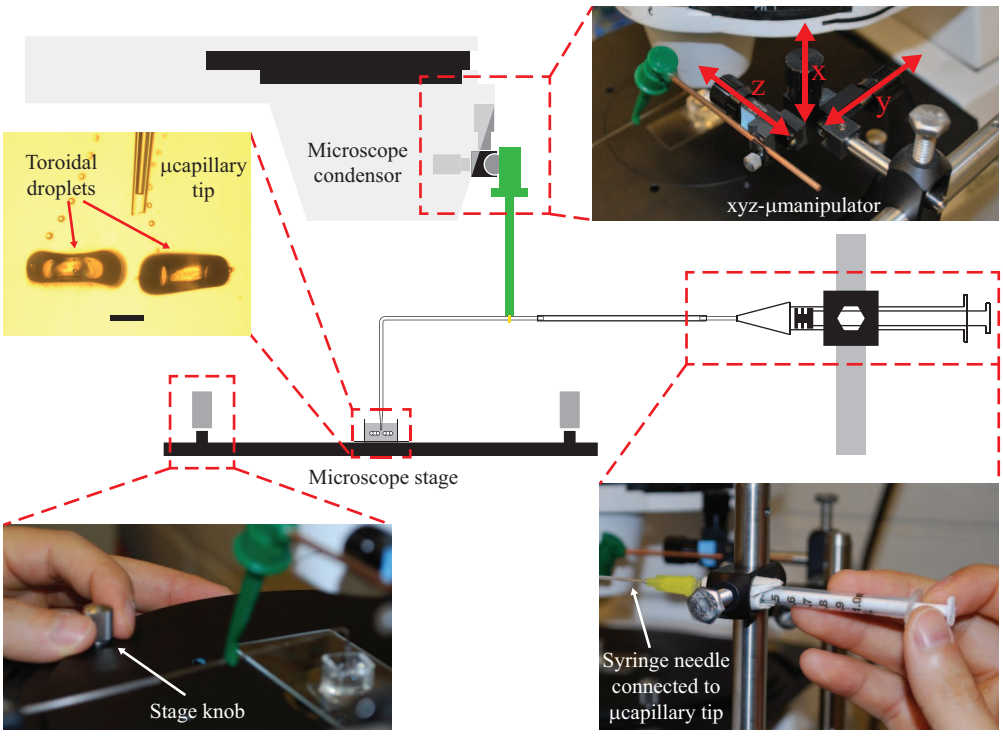

Figure E.1: Diagram showing the crucial components of the microsurgery. Scale bar represents 300 μm.

This process demands high precision, since the tori we joined are on the order of $\sim$ 1 mm. Thus we built our microsurgery setup around a microscope (see figure E.1). In this setup, we use an xyz micromanipulator to precisely position the glass microcapillary tip used to suck out the yield stress material between the tori. The microcapillary tip is connected to a small syringe which is

used to control the sucking pressure; note that controlling the sucking pressure is very delicate, so the syringe should be mounted on the side of the dominant hand of the user. In our setup, we keep the microcapillary tip stationary and move the sample with the stage knob of the microscope stage during surgery. See figure E.2 for an example on how we operate this setup.

Figure E.2: A picture of me performing microsurgery.

To make a double torus, we first generate two toroidal droplets side by side, as shown in figure E.3(a). Then, we position the microcapillary tip in between the two droplets to suck out the yield stress material between them, as shown in figure E.3(b). For the best result, we usually keep lowering the microcapillary tip until it is in the same focal plane as the center of the tori. As a result of the surrounding material being removed from between the tori, the liquid inside the tori will flow toward the tip. This is a crucial point because we do not want to actually suck up the inner liquid (unless we want to make the tori thinner), so right before the inner fluid is actually sucked into the tip, we need to apply positive pressure by pushing on the syringe just enough to stop the flow. Then we quickly removing the tip so the two tori will join, forming a double torus (see figure E.3(c)). At this point we have successfully generated a droplet with two handles.

Also microsurgery enables us to further manipulate the curvature of the droplet. For example, suppose we want to make the ligament joining the two tori fatter. To do this, we suck out more material on both sides of the joint to widen it (see figure E.3(d) and (e)). After we do this the joint area will be wider, as desired, but it is thinner than the tori in the perpendicular direction. To make it the same thickness as the tori, we stir the joint by moving the microscope stage around while the microcapillary tip is piercing the joint area, as shown in figure E.3(f). This causes the fluid to flow from one torus to another through the joint and as a result, the joint will become as thick as the tori, as shown in figure E.3(g). This is just one example-the shapes we can make are limited only by our imagination.

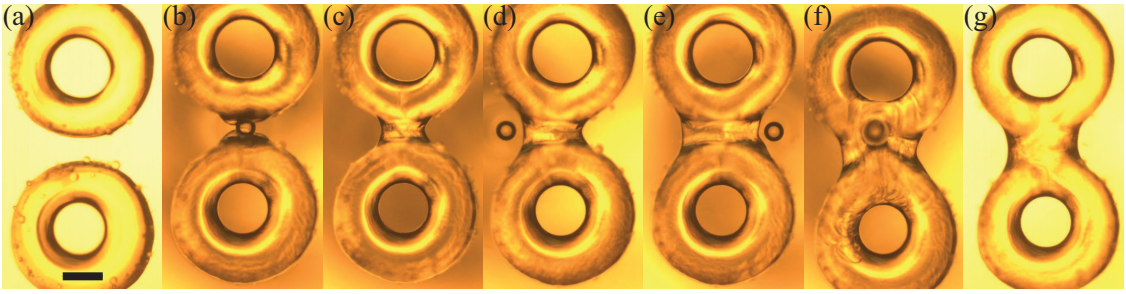

Figure E.3: (a) Two toroidal droplets side by side as viewed from the top. (b) The continuous yield stress material is being sucked out from the center between the two droplets. (c) Two toroidal droplets joined to form a double toroid droplet once sufficient material between the two original drops is removed. (d) and (e) More of the continuous phase is being removed from the sides to widen the joint area. (f) The area around the joint is stirred to increase the joint thickness to match the handles. (g) The finished double toroid droplet with a widened joint. Scale bar represents 200 μm.

APPENDIX F

CROSS POLAR MICROSCOPY

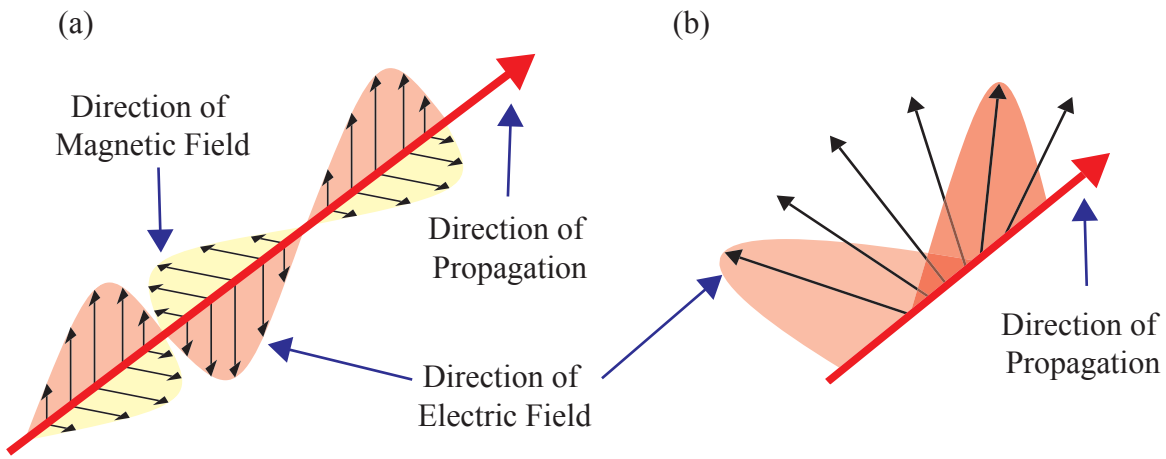

Figure F.1: A schematic showing: (a) linearly (b) elliptically polarized light.

Light is a transverse electromagnetic wave with perpendicular electric and magnetic field. Natural light is generally unpolarized, with all planes of propagation being equally probable, where the plane of propagation is defined as the plane containing the electric field. In linearly polarized light, the electric and magnetic fields are each confined within their own plane, as shown in figure F.1(a). Light composed of two plane waves with differing planes of propagation are said to be elliptically polarized, if their amplitudes are different, or circularly polarized, if their amplitudes are the same, as shown in figure F.1(b). Linearly polarized light can be generated by passing a light beam through a polarizer. A polarizer can also be used to terminate light with polarization direction perpendicular to the polarizer's axis. However, a single polarizer can never completely eliminate elliptically polarized light, because elliptically polarized light will always contain a component that is parallel to the polarization axis of the polarizer. Elliptically polarized light is generated by passing a light beam through a birefringent material. Birefringent materials have different indices of refraction; in crystalline materials, these indices are associated with different crystallographic directions. If the x and y directions are equivalent in terms of one of the indices of refraction, then the z-axis is unique

to another and is called the optic axis of the material. The component of light polarized along the optic axis is called the extraordinary or $e-wave$, while the component polarized in the plane perpendicular to the optic axis is called the ordinary or $o-wave$. Because of the difference in the index of refraction, the $e-wave$ and $o-wave$ propagate out of phase once they pass through a birefringent material.

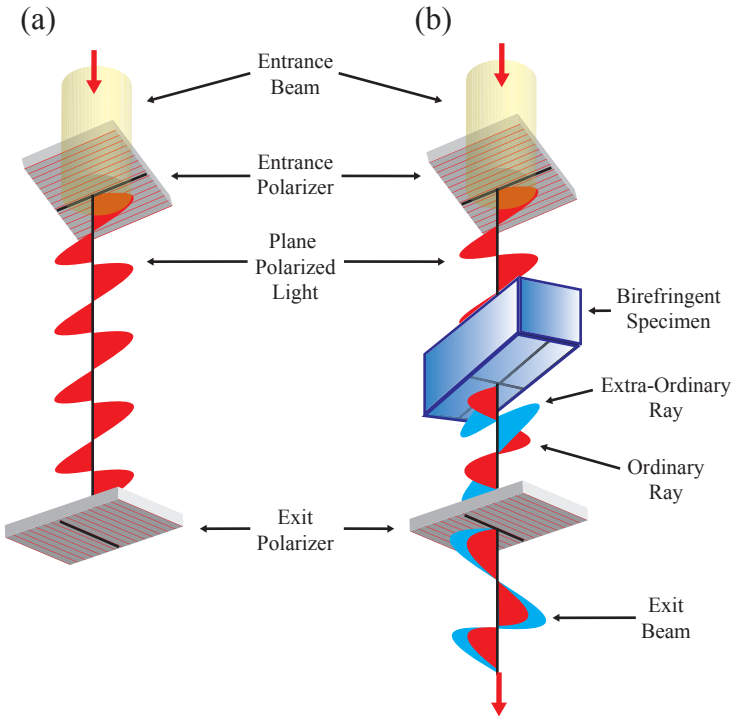

Figure F.2: A schematic showing a light beam passing through crossed polarizers: (a) without anything and (b) with a sample of birefringent specimen in between the two polarizers.

Cross-polar microscopy is a method designed to observe and photograph specimens that are visible primarily due to their birefringent nature. This method requires two polarizers to be placed in the optical pathway with the first polarizer (entrance polarizer) before the specimen and the second polarizer (exit polarizer or analyzer) after the specimen, as shown in figure F.2. The orientation of the entrance and exit polarizer also has to be arranged in such a way that their polarization axes are perpendicular to one another. Given this placement, an entrance light beam with any polarization state will get polarized by the entrance polarizer into a plane polarization state that is perpendicular to the axis of polarization of the second polarizer. Thus, without a birefringent specimen in between the two polarizers, the light will get terminated by the second polarizer, as shown in figure F.2(a).

However, if a birefringent specimen is placed after the first polarizer, a beam that gets polarized by the entrance polarizer gets polarized into elliptically polarized light and will pass through the second polarizer to the detector, as shown in figure F.2(b).

REFERENCES

[1] H. W. Kroto *et al*., Nature, **318** 162 (1985).

[2] M. F. Jarrold *et al*., Nature, **407** 26 (2000).

[3] M. J. Bowick, L. Giomi, Adv. Phys. **58**, 449 (2009)

[4] A. Bausch *et al*., Science **299**, 1716 (2003).

[5] Y. Chushak and A. Travesset, Europhys. Lett. **72**, 767 (2005).

[6] T. Einert *et al*., Langmuir **21**, 12076 (2005).

[7] P. Lipowsky *et al*., Nat. Mater. **4**, 407 (2005).

[8] T. M. William, V. Vitelli and P. M. Chaikin, Nature, **468** 947 (2010).

[9] R. D. Kamien, Rev. Mod. Phys. **74**, 953 (2002).

[10] T. C. Lubensky and J. Prost, j. Phys. II **2**, 371 (1992)

[11] T. Lopez-Leon, V. Koning, K. B. S. Devaiah, V. Vitelli, A. Fernández-Nieves, Nat. Phys. **7**, 39 (2011)

[12] P. S. Drzaic, *Liquid Crystal Dispersions* (World Scientific, River Edge, NJ, 1995)

[13] M. A. Bates, J. Chem. Phys. **128**, 104707 (2008).

[14] P. K. Chan and A. D. Rey, Liquid Crystals 23, 677 (1997).

[15] A. Fernández-Nieves, *et al*., Phys. Rev. Lett. **99**, 157801 (2007).

[16] S. Dhakal, F. J. Solis and M. Olvera de la Cruz, Phys. Rev. E: *Stat., Nonlinear, Soft Matter Phys.* **86**, 011709 (2012).

[17] H. Shin, M. J. Bowick and X. Xing, Phys. Rev. Lett. **101**, 037802 (2008).

[18] V. Vitelli and D. R. Nelson, Phys. Rev. E: *Stat., Nonlinear, Soft Matter Phys.* **74**, 021711 (2006).

[19] G. Napoli and L. Vergori, Phys. Rev. Lett. **108**, 207803 (2012).

[20] V. Koning, T. Lopez-Leon, A. Fernández-Nieves and V. Vitelli, Soft Matter **9**, 4993 (2013).

[21] G. A. Devries, *et al*., Science **315**(5810), 358 (2007).

[22] I. I. Smalyukh, Y. Lansac, N. A. Clark and R. P. Trivedi, Nat. Mater. **9**, 139 (2010).

[23] I. M. Kulic, D. Andrienko and M. Deserno, Europhys. Lett. **67**, 418 (2004).

[24] C. V. Boys, *Soap Bubbles - Their Colours and the Forces which Mould Them* (Dover Publication, New York, 1959).

[25] J. Plateau, *Statique experimentale et theorique des liquides soumix aux seules forces molecular*es (Paris, Gauthier-Villars, 1873).

[26] R. A. Brown and L. E. Scriven, Proc. R. Soc. London A **371**, 331 (1980).

[27] R. J. A. Hill and L. Eaves, Phys. Rev. Lett. **101**, 234501 (2008).

[28] F. Zoueshtiagh *et.al*., Eur. Phys. J. E **20**, 317 (2006).

[29] J. K. Walters and J. F. Davidson, J. Fluid Mech. **17**, 321 (1963).

[30] T. J. Pedley, J. Fluid Mech. **32**, 97 (1968).

[31] N. Baumann, D. D. Joseph, P. Mohr, and R. Renardy, Phys. Fluids **4**, 567 (1992).

[32] M. C. Sostarecz and A. Belmonte J. Fluid Mech. **497**, 235 (2003).

[33] Y. Renardy *et.al*., J. Fluid Mech. **484**, 69 (2003).

[34] Z. Yao and M. J. Bowick, Eur. Phys. J. E **34**, 32 (2011).

[35] L. Giomi and M. J. Bowick, Phys. Rev. E **78**, 010601 (R) (2008).

[36] L. Giomi and M. J. Bowick, Eur. Phys. J. E **27**, 275 (2008).

[37] H. Mehrabian and J. J. Feng, J. Fluid Mech. **717**, 281 (2013).

[38] A. S. Utada, A. Fernández-Nieves, H. A. Stone, and D. A. Weitz, Phys. Rev. Lett. **99**, 094502 (2007).

[39] To estimate this time scale we balance the driving force due to surface tension with the viscous force, which is the relevant opposing force in our experiments: $\gamma \approx \eta_o v = \eta_o a_{tip}/t_b$, where $v = a_{tip}/t_b$ is a representative velocity for the pinching process of a jet of radius $a_{jet} \approx a_{tip}$.

[40] S. Chandrasekhar, *Hydrodynamic and Hydromagnetic Stability* (Oxford University Press, New York, 1961).

[41] R. J. Donnelly and W. Glaberson, Proc. Roy. Soc. Lond. A **290**, 547 (1966).

[42] E. F. Goedde and M. C. Yuen, J. Fluid Mech. **40**, 495 (1970).

[43] S. Tomotika, Proc. Roy. Soc. **150**, 322 (1935).

[44] E. F. Geodde and M. C. Yuen, J. Fluid Mech. **40**, 495 (1970).

[45] M. Tjahjadi, H. A. Stone and J. M. Ottino, J. Fluid Mech. **243**, 297 (1992).

[46] J. Plateau, Acad. Sci. Bruxelles Mem. **23**, 5 (1849).

[47] L. Rayleigh, Proc. Roy. Soc. London **29**, 71 (1879).

[48] G. K. Batchelor, *An Introduction to Fluid Dynamics* (Cambridge University Press, New York, 2000).

[49] We emphasize that this force balance is only intended to provide an order of magnitude estimate for the speed. More precise calculations would be required to further develop this rough estimate.

[50] Z. Yao, *Geometries in Soft Matter* (Syracuse, New York, 2012).

[51] J. Vanderlinde, *Classical Electromagnetic Theory* (Kluwer Academic Publisher, 2004), 2nd ed.

[52] S. Khuri and A. Wazwaz, App. Math. Com. **85**, 139 (1997).

[53] Z. J. Taylor, R. Gurka, G. A. Kopp and A. Liberzon, IEEE Trans. Ins. and Meas., **59**, 3262 (2010).

[54] J. S. Hadamard, C. R. Acad. Sci., **152**, 1735 (1911).

[55] W. Rybczynski, Bull. Int. Acad. Pol. Sci. Lett., Cl. Sci. Math. Nat., Ser. A pp. 40 (1911).

[56] R. Clift, *Bubbles, Drops, and Particles* (Academic Press, New York, 1978).

[57] F. H. Garner and P. J. Haycock, Proc. Roy. Soc., Ser. A **252**, 457 (1959).

[58] F. H. Garner and A. H. P. Skelland, Chem. Eng. Sci. **4**, 149 (1955).

[59] A. I. Johnson and L. Braida, Can. J. Chem. Eng. **35**, 165 (1957).

[60] M. Linton and K. L. Sutherland, Proc. Int. Congr. Surf. Act., 2nd. **1**, 497 (1957).

[61] R. H. Magarvey and J. Kalejs, Nature **198**, 377 (1963).

[62] P. Savic, Natl. Res. Counc. Can. Rep. No. MT-22 (1953).

[63] K. E. Spells, Proc. Phys. Soc. London, Sect. B **65**, 541 (1952).

[64] V. G. Levich, *Physicochemical Hydrodynamics* (Prentice-Hall, New York, 1962).

[65] K. B. Friedrich and S. H. Siavash, Proc. WSEAS Int. Con., 195 (2006).

[66] C. Mundo, M. Sommerfeld and C. Tropea, Int. J. Multiph. Flow **21**, 151 (1995).

[67] E. Pairam and A. Fernández-Nieves, Phys. Rev. Lett. **102**, 234501 (2009).

[68] S. P. Meeker, R. T. Bonnecaze and M. Cloitre, J. Rheol. **48**, 1295 (2004).

[69] W. H. Herschel and R. Bulkley, (1926), Kolloid Zeitschrift **39**, 291 (1926).

[70] V. Trappe and D. A. Weitz, Phys. Rev. Lett. **85**, 449 (2000).

[71] M. Reiner *et al*., Kolloid Zeitschrift **65**, 44 (1933).

[72] J. Boujlel and P. Coussot, Soft Matter **9**, 5898 (2013).

[73] C. R. Beverly and R. I. Tanner, J. Rheol. **33**, 989 (1989).

[74] C. W. Macosko, *Rheology Principles, Measurements, and Applications* (VCH Publishers, 1994).

[75] P. Coussot and F. Gaulard, Phys. Rev. E: *Stat., Nonlinear, Soft Matter Phys.* **72**, 031409 (2005).

[76] G. German and V. Bertola, Phys. Fluids **22**, 033101 (2010).

[77] K. Niedzwiedz, H. Buggisch and N. Willenbacher, Rheol. Acta **49**, 1103 (2010).

[78] L. Martinie, H. Buggisch and N. Willenbacher, J. Rheol. **57**, 627 (2013).

[79] R. H. Dishington, Phys. Fluids **3**, 482 (1960).

[80] P. Chadwick, *Continuum Mechanics* (Wiley, New York, 1976).

[81] W. P. Graebel, *Advanced Fluid Mechanics* (Academic Press, 2007).

[82] C. W. Macosko, *Rheology Principles, Measurements, and Applications* (VCH Publishers, 1994).

[83] G. German and V. Bertola, Phys. Fluids **22**, 033101 (2010).

[84] D. R. Nelson, Nano. Lett. **2**, 1125 (2002).

[85] M. D. Contreras and R. Sanchez R, Int. J. Pharm. **234**(12), 149 (2002).

[86] R. D. Williams, J. Phys. Math. Gen. **19**,3211 (1986).

[87] G. E. Volovik and O. D. Lavrentovich, Zh. Eksp. Teor. Fiz. **85**, 1997 (1983).

[88] O. D. Lavrentovich and V. V. Sergan, Nuovo Cim **12**:1219 (1990).

[89] H. E. Stanley, *Introduction to Phase Transitions and Critical Phenomena* (Oxford Science, New York, 1971).

[90] D. W. Allender, G. P. Crawford and J. W. Doane, Phys. Rev. Lett. **67**, 1442 (1991).

[91] O. D. Lavrentovich, V. M. Pergamenshchik, Phys. Rev. Lett. **73**, 979 (1994).

[92] O. D. Lavrentovich, V. M. Pergamenshchik, Int. J. Mod. Phys. B **9**, 2389 (1995).

[93] R. D. Polak, G. P. Crawford, B. C. Kostival, J. W. Doane and S. Zumer, Phys. Rev. E: *Stat., Phys. Plasmas Fluids Relat. Interdiscip. Topics* **49**, R978 (1994).

[94] A. Sparavigna, O. D. Lavrentovich and A. Strigazzi, Phys. Rev. E: *Stat., Phys. Plasmas Fluids Relat. Interdiscip. Topics* **49**, 1344 (1994).

[95] R. P. Pan, *et al*., J. Bio. Phys. bf 29, 335 (2003).

[96] P. Yeh and C. Gu, *Optics of Liquid Crystal Displays* (Wiley, New York, 1999).

[97] A. Yariv and P. Yeh, *Optical Waves in Crystal* (Wiley, 1984).

[98] G. P. Alexander, B. G-g Chen, E. A. Matsumoto and R. D. Kamien, Rev. Mod. Phys. **84**, 497 (2012).

[99] M. A. Bates, G. Skacej and C. Zannoni, Soft Matter **6**, 655 (2010).

[100] V. Vitelli and D. R. Nelson, Phys. Rev. E: *Stat., Nonlinear, Soft Matter Phys.* **70**, 051105 (2004).

[101] M. Bowick, D. R. Nelson and A. Travesset, Phys. Rev. E: *Stat., Nonlinear, Soft Matter Phys.* **69**, 041102 (2004).

[102] E. Pairam, *et al*., PNAS bf 110, 9295 (2013).

[103] M. Kleman, O. D. Lavrentovich, *Soft Matter Physics, An Introduction* (Springer, New York, 2003).

[104] J. P. Sethna, Phys. Rev. B: *Condens. Matter* **31**(10):6278 (1985).

[105] J. F. Sadoc and J. Charvolin, J. Phys. A: Math. Theor. **42**, 465209 (2009).

[106] R. Mosseri and J. F. Sadoc, Struct. Chem. **23**, 1071 (2012).

[107] D. Kleckner and W. T. M. Irvine, Nat. Phys. **9**, 253 (2013).

[108] B. Senyuk, *et al*., Nature **493**, 200 (2013).

[109] U. Tkalec, M. Ravnik, S. Copar, S. Zumer and I.Musevic, Science **333**, 62 (2011).

[110] H. Shin and G. M. Grason GM, Eur. Phys. Lett. **96**, 36007 (2011).

[111] Y. Hatwalne and M. Muthukumar, Phys. Rev. Lett. **105**, 107801 (2010).

[112] Y. Rotenberg, L. Boruvka and A. W. Neumann, J. Colloid Interface Sci. **93**, (1983).

[113] Q. S. Chen, *et al*., J. Colloid Interface Sci. **106**, 353 (1985).

VITA

Ekapop Pairam was born on 18th of January 1983 in Nakhonratchasima, Thailand. He attended Marie Vithaya in Thailand for primary and middle school. In 1995 he left Thailand to study abroad in Dunedin, New Zealand for his high school education and graduated in the year 2000 receiving the DUX award along with it. In the following year he made his way to the United States to join Indiana University of Pennsylvania, where he received his B.Sc in Physics in 2004. In January 2008, he started his doctoral studies under the supervision of Prof. Alberto Fernández-Nieves at the Georgia Institute of Technology.